

2009-01-01

High Temperature Oxidation Characteristics of Nb-10W-XCr Alloys

Maria Del Pilar Moricca

University of Texas at El Paso, mdgonzalez5@miners.utep.edu

Follow this and additional works at: https://digitalcommons.utep.edu/open_etd



Part of the [Materials Science and Engineering Commons](#), and the [Mechanics of Materials Commons](#)

Recommended Citation

Moricca, Maria Del Pilar, "High Temperature Oxidation Characteristics of Nb-10W-XCr Alloys" (2009). *Open Access Theses & Dissertations*. 2738.

https://digitalcommons.utep.edu/open_etd/2738

This is brought to you for free and open access by DigitalCommons@UTEP. It has been accepted for inclusion in Open Access Theses & Dissertations by an authorized administrator of DigitalCommons@UTEP. For more information, please contact lweber@utep.edu.

HIGH TEMPERATURE OXIDATION CHARACTERISTICS
OF Nb-10W-XCr ALLOYS

MARIA DEL PILAR MORICCA

Department of Metallurgical and Materials Engineering

APPROVED:

S.K. Varma, Ph.D., Chair

Luis Trueba, Ph.D.

Miguel Castro-Colin, Ph.D.

Russell Chianelli, Ph.D.

Patricia D. Witherspoon, Ph.D.
Dean of the Graduate School

Copyright ©

by

Maria del Pilar Moricca

2009

Dedicated to:

Rebecca, Rachel, Natalia, and Tim

HIGH TEMPERATURE OXIDATION CHARACTERISTICS
OF Nb-10W-XCr ALLOYS

by

Maria del Pilar Moricca

DISSERTATION

Presented to the Faculty of the Graduate School of
The University of Texas at El Paso
in Partial Fulfillment
of the Requirements
for the Degree of

DOCTOR OF PHILOSOPHY

Department of Metallurgical and Materials Engineering

THE UNIVERSITY OF TEXAS AT EL PASO

December 2009

ACKNOWLEDGMENTS

I take this opportunity to express my appreciation for the valuable contributions of my professors, collaborators, and friends throughout my graduate career. I would like to thank my advisor, Dr. S.K. Varma, for all his support, patience, and guidance. Special thanks to Dr. Murr, who gave me the opportunity to pursue my graduate studies, without his support none of this would have been possible. I would also like to express my gratitude to my dissertation committee, Dr. Luis Trueba, Dr. Miguel Castro-Colin, and Dr. Russell Chianelli, for their time, guidance, and encouragement.

I gratefully acknowledge the financial support given by the Metallurgical and Materials Engineering Department and the National Energy Technology Laboratory of the U.S. Department of Energy, Project Number DE-FG26-05NT42491.

My deepest appreciation goes to my family; thank you for all your support, patience, love, and encouragement. This is our accomplishment.

ABSTRACT

The use of refractory metals in high temperature applications has been attractive for several years. Systems based on niobium represent a potential new generation of refractory materials systems because of their low density, high melting points, and strength at elevated temperatures. Despite these desirable characteristics, the widespread use of niobium-based alloys is limited because its oxidation resistance is still inadequate for structural applications. Understanding the oxidation kinetics of Nb-based alloys and the role of the different phases in the oxidation process is of crucial importance to improve the oxidation resistance of these materials.

The effect of Cr content on the microstructure and oxidation behavior of Nb-10W-XCr alloys with four different compositions has been investigated. Experiments were conducted for 24 hours in air at 900, 1100, and 1300°C under isothermal and cyclic conditions. The oxidation kinetics were evaluated in terms of weight change per unit area with respect to exposure time. The phases present in the alloys and the oxide scales were characterized by XRD, SEM and EDS.

Alloy's microstructure consists of Nb solid solution phase surrounded by a network of NbCr₂ Laves phase. An improvement trend for the oxidation resistance with increase of the intermetallic phase has been observed at 1300°C and oxidation kinetics follows a parabolic behavior. At 900°C, alloys with higher Cr content exhibit higher oxidation rates in comparison to alloys with lower Cr content. The oxidation products are a mixture of CrNbO₄ and Nb₂O₅ and the amount of each oxide present in the mixture is related to the intermetallic phase content and the oxidation temperature.

Results delineate the influence of microstructure and composition on the oxidation mechanisms of these alloys that represent a promising base for high-temperature alloy development.

TABLE OF CONTENTS

ACKNOWLEDGMENTS.....	v
ABSTRACT.....	vi
TABLE OF CONTENTS	viii
LIST OF FIGURES.....	xi
LIST OF TABLES.....	xv
CHAPTER 1:INTRODUCTION	17
1.1 Justification	19
CHAPTER 2:LITERATURE REVIEW.....	21
2.1 Refractory Metals.....	21
2.2 Refractory Metals and High Temperature Applications.....	23
2.3 Niobium as High Temperature Material	26
2.4 Niobium Alloys	27
2.4.1 Alloys Classification and Compositions	27
2.4.2 Effect of Cr Additions on Nb Alloys.....	29
2.4.2.1 Crystal Structure and General Properties of Laves Phases	30
2.4.3 Nb-Cr-W Alloys.....	33
2.5 Fundamentals of Oxidation	34
2.5.1 Thermodynamic Considerations	35
2.5.2 Pilling-Bedworth Ratio (PBR).....	38
2.5.3 Kinetics of Oxidation	40
2.5.3.1 Linear Kinetics.....	41
2.5.3.2 Parabolic Kinetics.....	42

2.5.3.3 Logarithmic Kinetics	42
2.5.4 Temperature Dependence of Oxidation.....	43
2.5.5 Oxidation of Alloys	44
2.5.6 Oxidation Theories	45
2.6 Oxidation Resistance of Nb and Nb-Based Alloys.	48
2.6.1 Oxidation of Nb.....	49
2.6.2 Oxidation of Nb Alloys	51
CHAPTER 3:EXPERIMENTAL METHODS	56
3.1 Preparation of the Alloys.....	56
3.2 Characterization of the Alloys	57
3.3 Oxidation Experiments.....	57
3.3.1 Isothermal Oxidation.....	57
3.3.2 Cyclic Oxidation.....	57
3.4 Oxidation Products Characterization.....	58
CHAPTER 4:RESULTS AND DISCUSSION.....	60
4.1 Isothermal Sections from Nb-W-Cr System	60
4.2 Alloys Characterization	61
4.3 Isothermal Oxidation	67
4.3.1 Oxidation Kinetics.....	67
4.3.2 Oxide Scale Characterization	74
4.3.2.1 Surface Morphology	74
4.3.2.2 Oxidation Products Analysis by X-ray Diffraction	80
4.3.2.3 SEM and EDS Analysis of Oxide-Metal Interfaces.....	84

4.3.3 Oxidation Models.....	103
4.4 Cyclic Oxidation	105
4.4.1 Oxidation Kinetics.....	105
4.4.2 Oxide Scale Characterization	107
4.4.2.1 SEM and EDS Analysis of Oxide-Metal Interfaces.....	108
4.4.2.2 Oxidation Products Analysis by X-ray Diffraction	113
CHAPTER 5:SUMMARY AND CONCLUSIONS	116
RECOMMENDATIONS.....	118
REFERENCES	120
CURRICULUM VITA.....	128

LIST OF FIGURES

Figure 2.1: Diagram illustrating the basic features of a gas turbine engine.....	25
Figure 2.2: Cr-Nb phase diagram.....	30
Figure 2.3: Distribution of the A atoms and the B atoms in Laves phases	32
Figure 2.4: A and B atoms configuration for (a) C15, (b) C14, and (c) C36 structures	32
Figure 2.5: Ternary phase diagram of the Nb-Cr-W alloy system at (a) 1000°C and (b) 1500°C	34
Figure 2.6: Schematic illustration of metal-oxygen reaction	37
Figure 2.7: Standard Gibbs energies of formation of selected oxides as a function of temperature.....	38
Figure 2.8: Variation of weight gain with time for linear, parabolic and logarithmic oxidation.....	41
Figure 2.9: Various oxidation behaviors observed in two phase alloys. (a) Independent oxidation to form a non-uniform scale. (b) Cooperative oxidation forming a uniform scale. (c) Solute rich second phase acts as a reservoir for the growth of the solute scale.....	45
Figure 2.10: Schematic illustration of Wahl's model.....	47
Figure 2.11: Calculated phase diagram for the Nb-O system	50
Figure 4.1: Isothermal sections at 25, 900, 1100, and 1300°C for the Nb-W-Cr system calculated by using Pandat™ 7.0 software.....	60
Figure 4.2: Optical images of the as-cast microstructure of Nb-W-Cr alloys.	61
Figure 4.3: BSE image and X-ray maps of 15Cr alloy showing Nb, Cr, and W distribution.....	62
Figure 4.4: BSE image and X-ray maps of 20Cr alloy showing Nb, Cr, and W distribution.....	62
Figure 4.5: BSE image and X-ray maps of 25Cr alloy showing Nb, Cr, and W distribution.....	63

Figure 4.6: BSE image and X-ray maps of 30Cr alloy showing Nb, Cr, and W distribution.....	63
Figure 4.7: Relationship between Cr content as measured by EDS and area fraction of intermetallic and solid solution.	64
Figure 4.8: XRD patterns of 15, 20, 25, and 30Cr alloys in the as-cast condition.	65
Figure 4.9: Lattice parameters of the Nb _{ss} in the alloys.....	66
Figure 4.10: Microhardness values of alloys in the as-cast condition and the relationship with the intermetallic phase volume percentage.	67
Figure 4.11: Isothermal oxidation curves for 15Cr, 20Cr, 25Cr, and 30Cr alloys at 1300°C.	68
Figure 4.12: Isothermal oxidation curves for 15Cr, 20Cr, 25Cr, and 30Cr alloys at 1100°C.	69
Figure 4.13: Isothermal oxidation curves for 15Cr, 20Cr, 25Cr, and 30Cr alloys at 900°C.	70
Figure 4.14: Weight gain and parabolic rate constant relationships to Cr content and temperature.....	71
Figure 4.15: Microhardness of alloys in the as-cast condition and after exposure for 24 hours in air at 900, 1100 and 1300°C.....	73
Figure 4.16: Oxidation products obtained from 15Cr and 20Cr alloys after isothermal oxidation for 24 hours.....	75
Figure 4.17: Oxidation products obtained from 25Cr and 30Cr alloys after isothermal oxidation for 24 hours.....	76
Figure 4.18: BSE images of the oxide surface of 15Cr alloy oxidized for 24 hours at 900, 1100, and 1300°C.	77
Figure 4.19: BSE images of the oxide surface of 20Cr alloy oxidized for 24 hours at 900, 1100, and 1300°C.	78
Figure 4.20: BSE images of the oxide surface of 25Cr alloy oxidized for 24 hours at 900, 1100, and 1300°C.	79
Figure 4.21: BSE images of the oxide surface of 30Cr alloy oxidized for 24 hours at 900, 1100, and 1300°C.	80

Figure 4.22: XRD pattern of the oxidation products obtained from the 4 alloys after 24 hours of exposure at 900°C.....	81
Figure 4.23: XRD pattern of the oxidation products obtained from the 4 alloys after 24 hours of exposure at 1100°C.....	82
Figure 4.24: XRD pattern of the oxidation products obtained from 15Cr, 20Cr, and 30Cr alloys after 24 hours of exposure at 1300°C.....	82
Figure 4.25: Relative intensity ratio as a function of the volume percentage of intermetallic phase.	83
Figure 4.26: BSE images of the metal-oxide interface of 15Cr alloy after 24 hours of exposure at 900°C. (a) and (c) interface, (b) and (d) oxide scale.....	85
Figure 4.27: BSE image and X-ray maps showing Nb, Cr, W, and O distribution for 15Cr alloy oxidized 24 hours at 900°C.	86
Figure 4.28: BSE images of the metal-oxide interface of 20Cr alloy after 24 hours of exposure at 900°C.	87
Figure 4.29: BSE image and X-ray maps showing Nb, Cr, W, and O distribution for 20Cr alloy oxidized 24 hours at 900°C.	88
Figure 4.30: BSE images of the metal-oxide interface of 30Cr alloy after 24 hours of exposure at 900°C showing oxidation of Nb _{ss} and NbCr ₂ to form Nb ₂ O ₅ and CrNbO ₄ respectively.	89
Figure 4.31: BSE images of the metal-oxide interface of 25Cr alloy after 24 hours of exposure at 900°C. (a) and (b) interface, (c) oxide scale.	89
Figure 4.32: BSE images of the metal-oxide interface (a) and oxide scale (b) of 30Cr alloy after 24 hours of exposure at 900°C.	90
Figure 4.33: BSE images of the (a) metal-oxide interface, and (b) oxide scale of 15Cr alloy after 24 hours of exposure at 1100°C.	91
Figure 4.34: BSE image and X-ray maps showing Nb, Cr, W, and O distribution for 15Cr alloy oxidized 24 hours at 1100°C.	92
Figure 4.35: BSE images of the (a) metal-oxide interface, and (b) oxide scale of 20Cr alloy after 24 hours of exposure at 1100°C.	93
Figure 4.36: BSE images of the (a) metal-oxide interface, and (b) oxide scale of 25Cr alloy after 24 hours of exposure at 1100°C.	93

Figure 4.37: BSE images of the (a) metal-oxide interface, (b) and (c) oxide scale of 30Cr alloy after 24 hours of exposure at 1100°C.	94
Figure 4.38: Cross-section BSE images of the metal-oxide interface (a) and oxide layer (b) of 15Cr alloy after 24 hours of exposure at 1300°C.	95
Figure 4.39: BSE image and X-ray maps showing Nb, Cr, W, and O distribution for 15Cr alloy oxidized 24 hours at 1300°C.	96
Figure 4.40: Cross-section BSE images of the metal-oxide interface (a) and oxide scale (b) of 20Cr alloy after 24 hours of exposure at 1300°C.	97
Figure 4.41: BSE image and X-ray maps showing Nb, Cr, W, and O distribution for 20Cr alloy oxidized 24 hours at 1300°C.	98
Figure 4.42: SEM images of the oxide layers formed on 25Cr and 30Cr alloys after 24 hours of exposure at 1300°C.	99
Figure 4.43: Cross-section BSE images of the metal-oxide interface (a) and an external oxide layer (b) for 25Cr alloy after 24 hours of exposure at 1300°C.	100
Figure 4.44: Cross-section BSE images of the metal-oxide interface (a) and internal oxide layer (b) of 30Cr alloy after 24 hours of exposure at 1300°C.	100
Figure 4.45: BSE image and X-ray maps showing Nb, Cr, W, and O distribution for 30Cr alloy oxidized 24 hours at 1300°C.	101
Figure 4.46: Schematic representation of the oxide scale formed on samples oxidized at 900°C. (a) 15Cr alloy. (b) 20Cr alloy.	104
Figure 4.47: Schematic representation of the oxide scale formed on samples oxidized at 1300°C. (a) 15Cr and 20Cr alloys. (b) 25 Cr and 30Cr alloys.	104
Figure 4.48: Cyclic oxidation curves for 15Cr, 20Cr, 25Cr, and 30Cr alloys at 1300°C.	106
Figure 4.49: Cyclic oxidation curves for 15Cr, 20Cr, 25Cr, and 30Cr alloys at 900°C.	106
Figure 4.50: Oxidation products obtained from 15Cr and 20Cr alloys after cyclic oxidation for 24 hours in air.	109
Figure 4.51: Oxidation products obtained from 25Cr and 30Cr alloys after cyclic oxidation for 24 hours in air.	110

Figure 4.52: BSE images of the metal-oxide interface from 15Cr alloy after 24 hours of cyclic exposure at 900°C.....	111
Figure 4.53: BSE images of the metal-oxide interface of 30Cr alloy after 24 hours of cyclic exposure at 900°C.....	111
Figure 4.54: BSE images of the metal-oxide interface of alloy 30Cr after cyclic exposure at 1300°C for (a) 8 hours, and (b) 24 hours.....	112
Figure 4.55: BSE images of the metal-oxide interface of alloy 15Cr oxidized for 8 hours at 1300°C.	113
Figure 4.56: XRD pattern of the oxidation products obtained from the 4 alloys after 24 hours of cyclic exposure at 900°C.....	114
Figure 4.57: XRD pattern of the oxidation products obtained from the 4 alloys after 24 hours of cyclic exposure at 1300°C.....	115
Figure 4.58: Relative intensity ratio as a function of the volume percentage of intermetallic phase for oxidation products of alloys oxidized under cyclic conditions.	115

LIST OF TABLES

Table 2.1: Properties of some refractory metals with potential to replace superalloys..	22
Table 2.2: Properties of Nb, W, and Cr	23
Table 2.3: Existing and emerging aeroengine materials	24
Table 2.4: Conventional niobium alloys for high temperature use.....	28
Table 2.5: Composition and microstructures of selected Nb-based multiphase alloys.	29
Table 2.6: Oxide-metal volume ratios of some common metals.....	40
Table 3.1: Nominal compositions of Nb-Cr-W alloys.	56
Table 3.2: Equipment description and operating conditions.....	59
Table 4.1: Elemental compositions determined by EDS analysis and area fraction of the NbCr ₂ phase in the as cast condition.	64
Table 4.2: Values of parabolic rate constants (kp) corresponding to isothermal exposure.	72
Table 4.3: Parabolic oxidation rate constants for Nb alloys developed for high temperature applications.....	72
Table 4.4: Elemental compositions (at%) of the oxides formed after 24 hours of exposure	102
Table 4.5: Values of parabolic rate constants (kp) and correlation coefficients corresponding to cyclic exposure at 900°C and 1300°C.	107

CHAPTER 1

INTRODUCTION

Considerable efforts have been devoted to enhance the capabilities of high temperature materials in order to develop higher efficiency engines and advanced aerospace systems. High temperature applications require materials with a balance of physical, chemical and mechanical properties that allow an improved performance under a combination of elevated temperature, high stress and aggressive environmental conditions.

The currently used Ni-base superalloys are only capable of withstanding temperatures up to 1150°C and although thermal barrier coatings (TBCs) can provide insulation in the hot region [1, 2], it is very difficult to achieve any further increase in service temperature because the operating temperature has reached 0.9T_m (melting point) of these superalloys [3, 4]. The urgency in discovering and evaluating new materials with higher temperature suitability is evident.

Systems based on niobium represent a potential new generation of refractory materials because of their low density, high melting points and strength at elevated temperatures. Despite these desirable characteristics, the widespread use of niobium-based materials in aircraft, missiles, and certain reactors is limited because of the poor oxidation resistance and the difficulty to form a protective-oxide layer on the Nb solid solution surface. Extensive investigations aimed to improve the oxidation resistance of Nb alloys have been performed. Initial studies of binary alloys of niobium with titanium, chromium, vanadium, molybdenum and certain other elements showed that these alloys exhibit higher oxidation resistance than pure niobium, but not sufficiently

high to be used as oxidation resistant materials [5]. Subsequent studies concentrated on the use of Al addition to induce the formation of a protective alumina scale. Although a protective layer of oxide was formed, the resulting alloys exhibit lower melting points and increased brittleness [6, 7, 8].

Recent studies have been concentrated in the development of Niobium systems with Al, Cr, Ge, Hf, Si, and Ti additions; often referred to as refractory metal-intermetallic composites (RMICs). These niobium alloys contain multiphase microstructures comprised of silicides, Laves phase and Nb solid solution [1-3, 9-17]. The NbCr₂ laves phase is of particular interest because it has high melting point (1730°C), reasonable density (7.7 g/cm³), high strength, excellent creep behavior and good oxidation resistance. However this phase exhibits brittleness and limited fracture toughness at low and intermediate temperatures [18, 19].

The multiphase approach has lead to the study of materials with microstructures composed of a dispersion of hard intermetallic particles in a refractory, but, relatively more ductile, solid solution matrix which allows a more favorable balance of high temperature strength and good oxidation resistance.

Recent studies show that the Nb-Cr-X system (X is a refractory metal) may exhibit such characteristics [20-22]. The system Nb-W-Cr is of interest because a duplex microstructure consisting of NbCr₂ Laves phase and a bcc solid solution can be obtained. The low temperature fracture toughness can be improved by the Nb solid solution (Nb_{ss}) and the high temperature strength and good oxidation resistance can be anticipated from the Laves phase [6, 20]. The results of oxidation resistance in air for Nb-20W-5Cr and Nb-20W-10Cr (composition are in weight percents) have been

reported recently [23-26]. These alloys show improvement in oxidation resistance as the temperature increases.

Understanding the oxidation kinetics of Nb-based alloys is of crucial importance to improve the oxidation resistance. This dissertation presents the results of an investigation performed in order to study the effect of the Cr content on the cyclic oxidation behavior of four alloys from the Nb-W-Cr system at 900, 1100, and 1300°C. The results are expected to provide guidance towards the development of a structural material with improved oxidation resistance for use in high temperature applications.

1.1 Justification

Materials that can withstand high temperatures and corrosive environments are constantly sought after in the power generation and aerospace industries, typically for gas turbine engine (GTE) and land-based industrial gas turbines (IGT) applications. The efficiency of a turbine engine depends upon the difference in temperature between the gas in the combustion chamber and the exhaust gas; therefore it can be improved either by increasing the turbine entry temperature (TET) or by reducing the temperature of exhaust gases. The TET has increased by approximately 93°C over the past ten years. For every 30°C increase in the firing temperature, the gas turbine combined-cycle efficiency improves approximately 1% which translates into millions of dollars in savings to an electrical power producer [27-29]. An increase of 56°C in the use temperature could result in a decrease of about one million per military aircraft life-cycle cost [30].

Materials and processes improvements have enabled better performance along with improving the durability and reliability of the turbines. As working temperatures

continue to rise and operating conditions become steadily more aggressive, it has become evident that new materials should not only be designed with merely their mechanical performance in mind; the development of materials with improved oxidation resistance has become a necessity.

Studies regarding oxidation resistance, particularly for refractory metals such as niobium which may constitute a base for materials operating at high temperatures, are of undoubted interest. Alloys from the Nb-W-Cr system are promising candidates for high temperature applications because Nb and W sustain high thermal stability and Cr could offer the chemical stability needed to provide oxidation resistance. Although the study of alloys from this system initiated in the past decade [20, 21, 23-26], the amount of research done is limited for the following reasons: (1) lack of basic experimental data on thermodynamical, mechanical and physical properties, (2) difficulties associated with the processing of the alloys, and (3) scarce information on the conditions required for the formation of a protective oxide scale.

The oxidation of alloys from the Nb-W-Cr system is not well understood and it is affected by many factors including composition, microstructure and oxidation temperature. The following aspects play an important role on the oxidation behavior;

- Alloy composition and microstructure.
- Oxidation of the alloys at intermediate (800°C-1000°C) and high (>1200°C) temperatures.
- Diffusion mechanisms of the elements forming the oxides.

The study of these factors constitutes the foundation for the improvement of the oxidation resistance of Nb-based alloys.

CHAPTER 2

LITERATURE REVIEW

Extensive studies have been performed in order to replace the Ni-based superalloys with intermetallics, ceramics and metallic alloys. To overcome the temperature limitation of Ni base superalloys, the candidate material should exhibit high melting point, low density, good oxidation resistance, and high temperature strength.

2.1 Refractory Metals

Refractory metals can be conveniently defined as those metals and their alloys that have melting points and chemical resistance properties that surpass those of stainless steel, cobalt-based or nickel-based alloys [31]. Traditionally, refractory metals are defined as those elements with a melting point higher than 1925°C [32]. A cut off temperature of 2200°C has also been suggested to define the “true” refractory metals. A more restrictive definition states that the pure metal must have a body-centered cubic (bcc) structure and that the ratio of the melting point of the metallic oxide to that of the base metal be less than one [31]. Although the definition of refractory metal appears to be context dependent, the common characteristic is a high melting temperature, higher than the melting temperature of titanium (1660°C) and zirconium (1850°C). Table 2.1 presents the melting points and densities of some refractory metals with potential to replace superalloys.

Table 2.1: Properties of some refractory metals with potential to replace superalloys [33, 34].

Element	Melting point (°C)	Density (g/cm ³)
V	1902	5.8
Nb	2468	8.6
Ta	2966	16.7
Cr	1907	7.2
Mo	2617	10.3
W	3422	19.3
Re	3180	21.0

According to the melting temperatures, these metals appear to have inherent advantage for high temperature applications; however certain drawbacks have limited their use. Some of the limitations of refractory metals as high temperature materials have been discussed by Briant [33] and they can be summarized as follows:

- Relatively high density; aluminum, titanium or nickel have densities of 2.7, 4.5, and 8.9 g/cm³ respectively. Elements such as V, Nb, and Cr show comparable or lower densities; but elements with higher melting points (W, Ta, and Re) have higher densities.
- Loss of strength at high temperatures, most of the refractory metals have bcc crystal structure and therefore alloys based on these metals show significant loss of strength at high temperatures.
- Alloy processing; casting is difficult due to their high melting temperature.
- Poor oxidation resistance.

Many of the deficiencies can be overcome by the addition of alloying elements. The right type of addition can lower the density, provide high temperature strength or low temperature toughness through the formation of second phases, or provide oxidation resistance.

Of all refractory metals Nb and Mo have been considered as having the greatest potential for high temperature applications. Table 2.2 presents general properties of Nb, W, and Cr.

Table 2.2: Properties of Nb, W, and Cr [33, 34].

Element	Nb	W	Cr
Atomic Number	41	74	24
Density (g/cm ³)	8.58	19.3	7.19
Melting point (°C)	2468	3422	1907
Crystal Structure	BCC	BCC	BCC
<i>Coefficient of Thermal Expansion (μm/mK)</i>	7.3	4.5	4.9

2.2 Refractory Metals and High Temperature Applications

Operation at high temperatures is of fundamental importance to many sectors of the industry, including material production and processing, chemical engineering, power generation, transportation, and aerospace.

Ni and Co-based superalloys are extensively used in the land-based gas turbines and aero engines. These alloys are engineered to meet the demands of stability at high temperatures while retaining most of its ambient strength and exhibiting good creep and fatigue resistance. Superalloys have a complex structure and may contain in excess of ten different alloying elements in order to satisfy the performance requirements. In terms of oxidation resistance, Cr is primarily added to Ni-based alloys for environmental protection, whereas Al is not only added to provide oxidation resistance by forming a protective Al₂O₃ scale but also is a gamma prime former which is the primary strengthening mechanism in Ni-based superalloys [28].

Alloying elements such as Mo, W, Ta, Re, and Co promote solid solution strengthening.

Since Ni-based superalloys are currently used at about 80 to 90% of its melting point; considerable efforts have been made to develop new high temperature materials for gas turbine engine applications. In the temperature range between 1000°C and 1400°C, a number of very high temperature material systems are being considered for potential applications in the next generation of engines. These include refractory metal intermetallic composites based on silicides, Laves phase, or both. Table 2.3 presents a list of existing aeroengine materials as well as the emerging systems that have been identified as potential candidates [35].

Table 2.3: Existing and emerging aeroengine materials [35].

Section(s) of Aeroengine	Existing Alloy System(s)	Density (g/cm ³)	Emerging Alloy System(s)	Density (g/cm ³)
Fan hubs and disks	Ti-6Al-4V	4.5	Polymer matrix composites	2
Compressors	α and/or β Ti alloys	4.5	Orthorhombic Ti alloys/composites	4.5-5.0
Combustors	Ni-base superalloys	8-10	Ceramic matrix composite	2
Turbines	Ni-Co-base superalloys	8-10	Niobium/intermetallic	5-6
Nozzles	Nb alloys	10-12	Niobium/intermetallic	5-6

Since the development of high temperature alloys is inextricably linked to the gas turbine engine, a schematic of a gas turbine engine is presented in Figure 2.1. There are three main sections, the compressor, the combustion chamber or burner, and the turbine. The function of the compressor is to increase the incoming air pressure and consists of blades and discs that are usually fabricated from Ti-6Al-V alloys. The temperatures in the low pressure zones are close to room temperature,

however higher temperatures (approximately 400°C-500°C) may occur in the high pressure stages. The compressed air enters in the combustion chamber where it is mixed with fuel and ignited. The hot gases are allowed to expand through a turbine, which extracts the mechanical work required to drive the compressor; this requires a shaft which transmits the torque required for the process to happen. The thrust arises from the momentum change associated with the incoming air being accelerated and its emergence as exhaust gas at significantly higher temperature. Nickel and Co-based superalloys are used in the combustor chamber and the turbine sections due to the high temperatures in these sections, which range from 500°C to 650°C in the discs to approximately 1200°C at the tips of the blades in the turbine. Beyond the turbine section of an aeroengine, air is expanded through the nozzles, typically made of coated niobium based alloys. In order to improve the temperature capability of alloys for high temperature applications, thermal barrier coatings (TBCs) are widely used. These are thick oxide coatings (Y_2O_3 -stabilized ZrO_2) that can lower metal alloy surface temperature by reducing the heat flux. TBCs are mainly used in combustion chambers, but the use in nozzles and blades is even more promising.

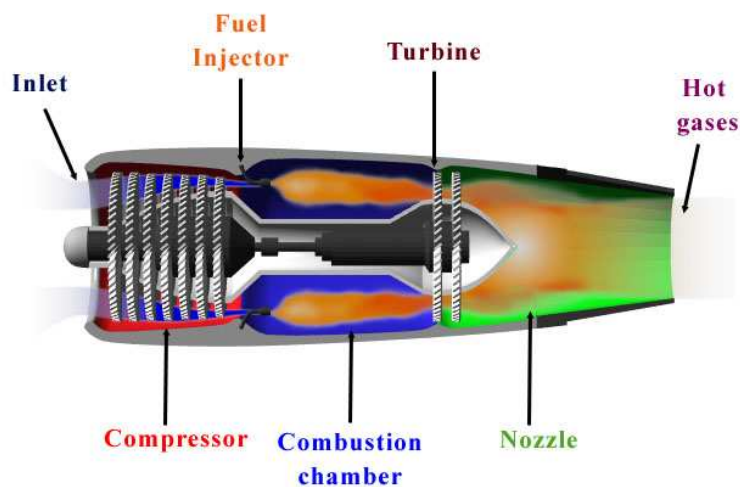


Figure 2.1: Diagram illustrating the basic features of a gas turbine engine [36].

2.3 Niobium as High Temperature Material

Niobium and its alloys exhibit properties that provide technological capabilities of great importance among the refractory metals. Although niobium was discovered more than two hundred years ago, it was not until the early 20th century that niobium was first used commercially. Brazil is the leading producer of niobium and ferroniobium, an alloy of niobium and iron. Niobium is used in the field of oil and gas transportation, in aircraft engines, automotive industry, nuclear industry, construction, jewelry and in magnetic applications such as medical diagnosis devices. The low neutron capture cross-section make it suitable for nuclear energy applications; Nb is also resistant to some types of chemical attack and its melting point, density and high melting oxide make it attractive candidate as a base metal for high temperature structural materials. Approximately 95% of all niobium is used as alloy additions in steel and nickel alloys. Only 1-2% of niobium is used as pure niobium metal or for niobium-based alloys [37].

Appreciable amounts of the element are used in nickel-, cobalt-, and iron-based superalloys for such applications as jet engine components, gas turbines, rocket subassemblies, and heat resisting and combustion equipment. One example of a nickel-based niobium-containing superalloy is Inconel 718, which consists of approximately 53% Ni, 19% Cr, 18.5% Fe, 5% Nb, 3% Mo, 0.9% Ti, and 0.5% Al [29]. Even the most advanced superalloys cannot meet the challenges imposed by the performance requirements of power generation systems because of the melting temperature of nickel.

The advantages of niobium as compared with other refractory metals can be summarized as follows: niobium is the one of the least dense and most ductile of all refractory metals. Its strength can be improved by alloying to make it competitive with and superior to molybdenum and its alloys, the closest rival for use at temperatures in excess of 1500°C. The main disadvantage of Nb is poor oxidation resistance at moderate and high temperatures, a protective coating is necessary for these applications to prevent the alloy from becoming brittle. Their refractory metal intermetallic composites depend on an intermetallic phase to provide high temperature oxidation resistance [2].

2.4 Niobium Alloys

Niobium alloys have been explored for applications with temperatures exceeding 1100°C for more than 50 years. The alloys are made by subsequent vacuum arc remelting with the appropriate elemental additions. Alloying elements are added to niobium mainly to increase elevated temperature strength and/or to increase oxidation resistance. The alloying additions used in commercial and developmental niobium alloys include [38]:

- Substitutional solutes (Mo, W, V, Ta)
- Reactive elements for carbides, nitrides and/or oxide formation (Zr, Hf, Ti)
- Interstitials (C, N)

2.4.1 Alloys Classification and Compositions

Niobium alloys are usually categorized in terms of strength; low strength alloys are highly fabricable and weldable, Nb-1Zr and C-103 belong to this group.

Nb-1Zr is widely used for liquid metal containers, sodium and magnesium vapor lamps and nuclear applications; C-103 is used in aerospace applications as thrust cones, and high temperature valves. Moderate strength alloys such as PWC-11, Cb129Y, and FS-85 are generally used for aerospace applications. Higher-strength alloys are used in aircraft gas turbine blades; one example is WC-3009, this alloy also exhibits an oxidation rate less than one tenth of that of most Nb alloys [39]. Table 2.4 lists conventional Nb alloys.

Table 2.4: Conventional niobium alloys for high temperature use [37, 40, 41].

Alloy	Composition (wt%)	Density (g/cm ³)	Melting Temperature (°C)
Nb-1Zr	Nb-1Zr	8.57	2410±10
C-103	Nb-10Hf-1Ti	8.85	2350±50
PWC-11	Nb-1Zr-0.1C	8.57	2410±10
WC-3009	Nb-30Hf-9W	10.10	-
FS-85	Nb-28Ta-10W-1Zr	10.60	2590±10
Cb-752	Nb-10W-2.5Zr	9.10	-
Cb-129Y	Nb-10W-10Hf-0.1Y	-	-

More recent studies have led to the development of multiphase alloys; often referred to as refractory metal intermetallic composites (RMICs) or in situ composites, these alloys contain significant amounts of one or more intermetallic phases in a metallic matrix or an intermetallic matrix with ductile metallic particles. The Nb-based multiphase alloys are usually divided into four categories according to the strengthening phases [35].

1. Nb-Si-X strengthened by silicides
2. Nb-Cr-X strengthened by Laves phase
3. Nb-Al-X strengthened by aluminides
4. Nb-Cr-Si-Al-X strengthened by silicides and Laves phase

The X represents a list of alloying elements the most used are Fe, Ge, Hf, Mo, Sn, Ta, Ti, and W. Depending on the alloy composition, as many as four silicides (Nb_5Si_3 , Nb_3Si , Ti_5Si_3 , and Ti_3Si) and two Laves phases (C14 and C15 NbCr_2) can be present in the microstructure of these composites. A list of selected Nb-based multiphase alloys containing composition and microstructure is presented in Table 2.5.

Table 2.5: Composition and microstructures of selected Nb-based multiphase alloys.

Alloys Composition (at%)	Microstructure	Reference
Nb-10Si	$\text{Nb}_{\text{ss}} + \text{Nb}_5\text{Si}_3$	[35, 42]
Nb-10Ti-10Si	$\text{Nb}_{\text{ss}} + (\text{Nb,Ti})_5\text{Si}_3 + (\text{Nb,Ti})_3\text{Si}$	[35]
Nb-10Ti-10Si-9Al	$\text{Nb}_{\text{ss}} + \text{Nb}_5\text{Si}_3 + \text{Nb}_3\text{Al}$	[42]
Nb-24Ti-18Si	$\text{Nb}_{\text{ss}} + (\text{Nb,Ti})_3\text{Si}$	[43, 44]
Nb-24Ti-18Si-5Cr	$\text{Nb}_{\text{ss}} + \text{Nb}_5\text{Si}_3 + (\text{Nb,Ti})_3\text{Si} + \text{NbCr}_2$	[44]
Nb-18Al	$\text{Nb}_{\text{ss}} + \text{Nb}_3\text{Al}$	[35, 42]
Nb-10Ti-15Al	$\text{Nb}_{\text{ss}} + \text{Nb}_3\text{Al}$	[35]
Nb-30Cr	$\text{Nb}_{\text{ss}} + \text{NbCr}_2$	[35]
Nb-45Cr-4W	$\text{Nb}_{\text{ss}} + \text{NbCr}_2$	[45]
Nb-20Cr-20Mo-15Si-5B	$\text{Nb}_{\text{ss}} + \text{Nb}_5\text{Si}_3 + \text{NbCr}_2 + \text{Nb}_3\text{Si}$	[46]
Nb-18Si-5Cr-5Al-5Mo	$\text{Nb}_{\text{ss}} + \text{Nb}_5\text{Si}_3 + \text{NbCr}_2 + \text{Nb}_3\text{Si}$	[14]

2.4.2 Effect of Cr Additions on Nb Alloys

Additions of Cr to Nb alloys have been known for improving the oxidation resistance, but also lead to the formation of Laves phases (NbCr_2). Formation of Laves phase is important for oxidation resistance, as well as mechanical properties. Excess of Laves phase introduces brittleness into the system but on the other hand, can improve oxidation.

Figure 2.2 shows the Cr-Nb binary phase diagram revised by Thoma et al. [47] by means of XRD and chemical analysis. The diagram shows the formation of an

intermediate phase, NbCr_2 ; this phase forms a eutectic with each of the terminal solid solutions, (Cr) and (Nb). High temperature Laves phase (C14) is stable above 1650°C and the low temperature (C15) Laves phase is stable at temperatures below 1650°C [35].

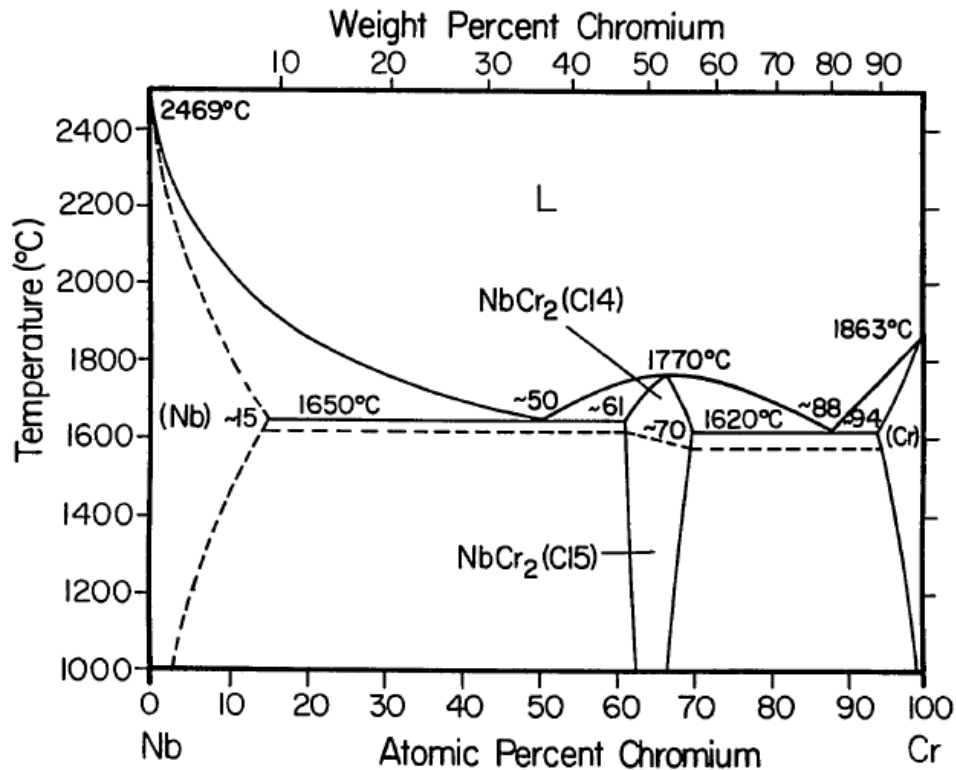


Figure 2.2: Cr-Nb phase diagram [47].

2.4.2.1 Crystal Structure and General Properties of Laves Phases

Laves phases comprise the largest group of intermetallic compounds. Initial studies of the crystallographic structure and properties of these phases were performed by Friauf [48, 49] and Laves [50], from whom they derive their name: "Friauf-Laves" or, more commonly "Laves" phases. Laves phases are attractive as high-temperature structural materials operating in severe environments because they have high melting point, low density, high strength up to high temperatures, and

potential resistance to oxidation [21]. The principal limitation is their brittleness at ambient temperatures which has been tried to overcome by combining Laves phases with a ductile phase such as Nb_{ss} [18, 51, 52].

The Laves phase structures are adopted by a large number of binary intermetallic compounds of composition AB₂. Three different types of the Laves phase structure are generally observed: the cubic MgCu₂ type (C15), the hexagonal MgZn₂ type (C14), and the dihexagonal MgNi₂ type (C36) [51]. Element A forms a cubic, hexagonal, and a dihexagonal structure and element B forms a tetrahedral around each A atom. The stability of the structure is primarily determined by the atomic size ratio of the A and B atoms. As it is shown in Figure 2.3 the crystal structures are related to each other as the basic unit layer of these phases is the same, while the stacking sequence of the unit layer is different in each structure.

The C15 structure is face-centered cubic with 8 formula units per non-primitive cubic unit cell, the A-sublattice defines a cubic diamond net, while the B sublattice can be described in terms of tetrahedra. The C14 structure is hexagonal with 4 formula units per unit cell, the A sublattice defines a hexagonal diamond net and the B sublattice is again composed of tetrahedra, however the arrangement is distinct to that in C15. The C36 structure also belongs to the hexagonal space group with 8 formula units per unit cell, this structure can be defined as a composite of the C14 and C15 structures [53]. The A and B nets for the different configurations are presented in Figure 2.4.

Among the Laves phases, NbCr₂ shows the most promise as a high temperature material. The NbCr₂ Laves phase has a melting temperature of 1730°C,

appreciable creep resistance, high strength, a density of 7.7 g/cm^3 , excellent oxidation resistance below 1100°C [54]. The C14 crystal structure is stable above 1650°C , and the low temperature (C15) Laves phase is stable at temperatures below 1650°C . The C15 is an ordered fcc phase which offers more slip systems than other types [35, 19].

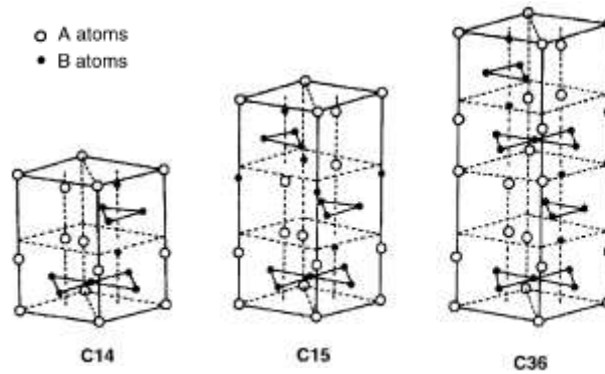


Figure 2.3: Distribution of the A atoms and the B atoms in Laves phases [51].

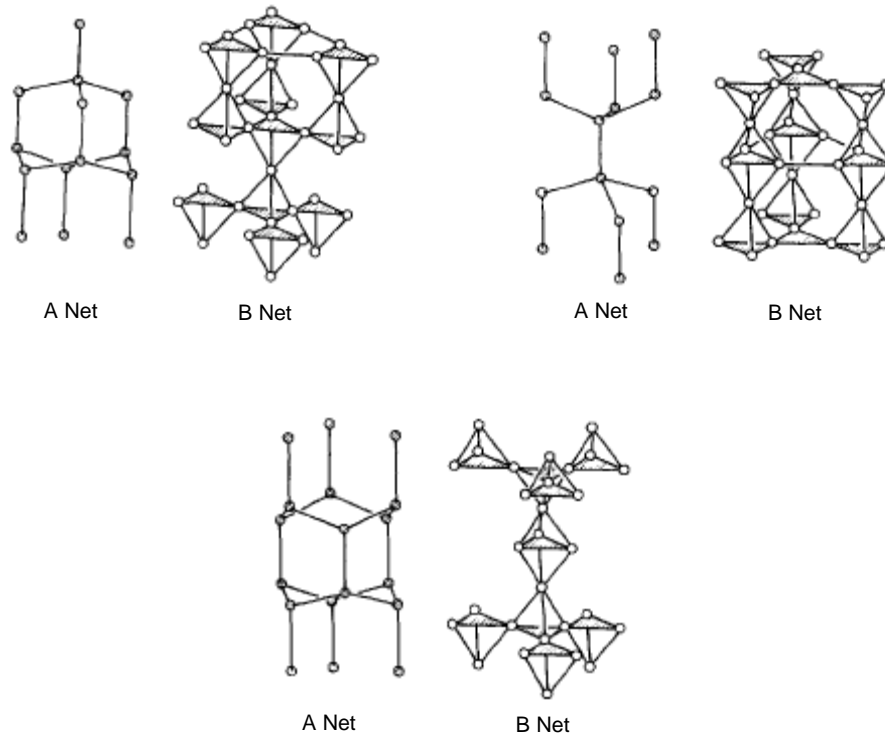


Figure 2.4: A and B atoms configuration for (a) C15, (b) C14, and (c) C36 structures [53].

2.4.3 Nb-Cr-W Alloys

The Nb-Cr-X alloys system (X is a refractory metal such as V, Mo, Hf, Ta and W) is of interest for the development of high-temperature materials because Nb sustains thermal stability and Cr offers resistance to corrosion [22]. In relation to the phase diagrams, the Nb and Cr form an intermediate NbCr₂ phase that equilibrates directly with the bcc solid solution without forming any ternary compounds. The element W is soluble by about 8 at% in the NbCr₂ phase at 1632 K [20]. The Laves phase exhibits a very low creep rate, inherently high oxidation resistance, and it is extremely brittle at ambient temperature. Anton and Shah showed that the concept of ductile phase toughening for the NbCr₂/Nb is possible [35].

The isothermal sections at 1000°C and 1500°C for the Nb-W-Cr system, reported by English [55], are presented in Figure 2.5. Depending on the composition, two combinations are obtained: (a) Nb solid solution particles embedded within a NbCr₂ matrix or (b) Cr(α₂) or Nb(α₁) solid solution matrix containing NbCr₂ particles [35]. This last combination is expected to provide a more favorable balance of high temperature strength, fracture toughness and oxidation resistance than Nb-Cr alloys with duplex microstructure.

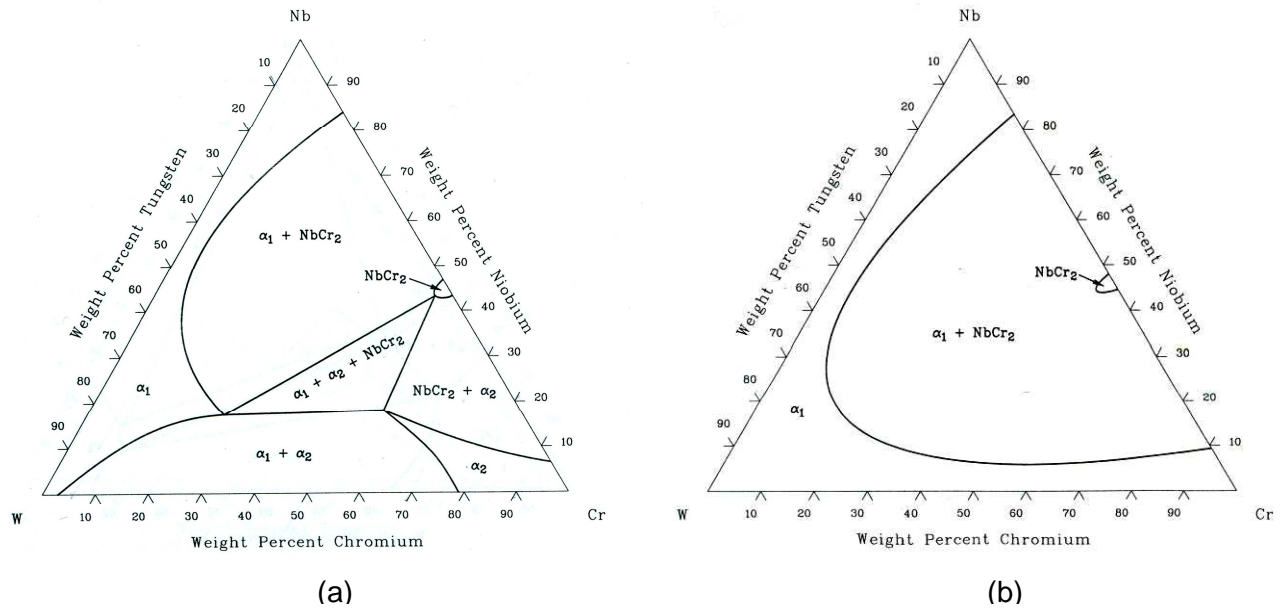


Figure 2.5: Ternary phase diagram of the Nb-Cr-W alloy system at (a) 1000°C and (b) 1500°C [55].

2.5 Fundamentals of Oxidation

Metals react chemically when exposed to air or other more aggressive gases. High temperature exposure is specially damaging to most metals because of the exponential increase in reaction rate with temperature. The term high temperature corrosion usually refers to material degradation at temperatures higher than the ambient, when exposed to corrosive environments. The most common reactant is oxygen in the air; the oxygen-metal reactions are referred to as oxidation. Oxidation is the most important high temperature reaction. In the simplest form, an oxidation reaction is represented by the interaction of metal with oxygen to form an oxide. The overall equation for the chemical reaction involved in the oxidation of a metal may be written as:



An oxidation reaction begins with the adsorption of oxygen on the metal surface. The oxide nucleates at multiple sites that are thermodynamically favorable and grows to form a film, as the reaction proceeds the oxygen may dissolve in the metal. The thin oxide layer grows to a thicker scale providing a protective scale barrier, the reaction then proceeds through the solid-state diffusion of the reactants through the scale. The metal may form a porous scale or growth stresses in the scale may lead to the formation of cavities and microcracks, this will modify the oxidation mechanism and may cause the oxide to fail to protect the metal [56, 57]. Figure 2.6 illustrates the various stages and aspects of the oxidation of a metal.

2.5.1 Thermodynamic Considerations

The driving force for metal-oxygen reactions is the Gibbs energy change, ΔG . Since the conditions most often encountered in high temperature reactions are constant temperature and pressure, ΔG is described by the Second Law of Thermodynamics as:

$$\Delta G = \Delta H - T\Delta S \quad (2.2)$$

where ΔH is the enthalpy of reaction, ΔS is the entropy change and T is the absolute temperature. An oxidation reaction will occur spontaneously if $\Delta G < 0$, if $\Delta G = 0$, the system is at equilibrium, and if $\Delta G > 0$ the reaction is thermodynamically unfavorable.

The driving force ΔG for the oxidation reaction in Equation 2.1 can be expressed as:

$$\Delta G = \Delta G^\circ + RT \ln \left[\frac{a_{M_xO_y}}{(a_M)^x (a_{O_2})^{y/2}} \right] \quad (2.3)$$

where the chemical activity, a , of each reactant or product is raised to the power of its stoichiometric coefficient, ΔG° is the standard free energy of formation, and R is the gas constant. Generally, the activities of the metals and the oxide are considered to be equal to 1, and the oxygen partial pressure is used for the activity of the oxygen. Therefore at equilibrium Equation 2.3 can be written as:

$$\Delta G^\circ = RT \ln p_{O_2} \quad (2.4)$$

$$p_{O_2} = \exp \left(\frac{\Delta G^\circ}{RT} \right) \quad (2.5)$$

where p_{O_2} is the partial pressure of oxygen. Equation 2.5 is used to determine the partial pressure of oxygen in equilibrium with the oxide from the standard free energy of formation. Thermodynamically the oxide will form only if the oxygen potential in the environment is larger than the oxygen partial pressure in equilibrium with the oxide.

A plot of the standard free energy of formation of metal oxides as a function of temperature and the corresponding dissociation pressures of the oxides is known as Ellingham diagram (Figure 2.7). These diagrams are used to get information about the partial pressure of oxygen required for any metal to form oxides at different temperatures. The stabilities of various oxides may be compared directly, the lower the position of the line on the diagram, the more stable is the oxide [58].

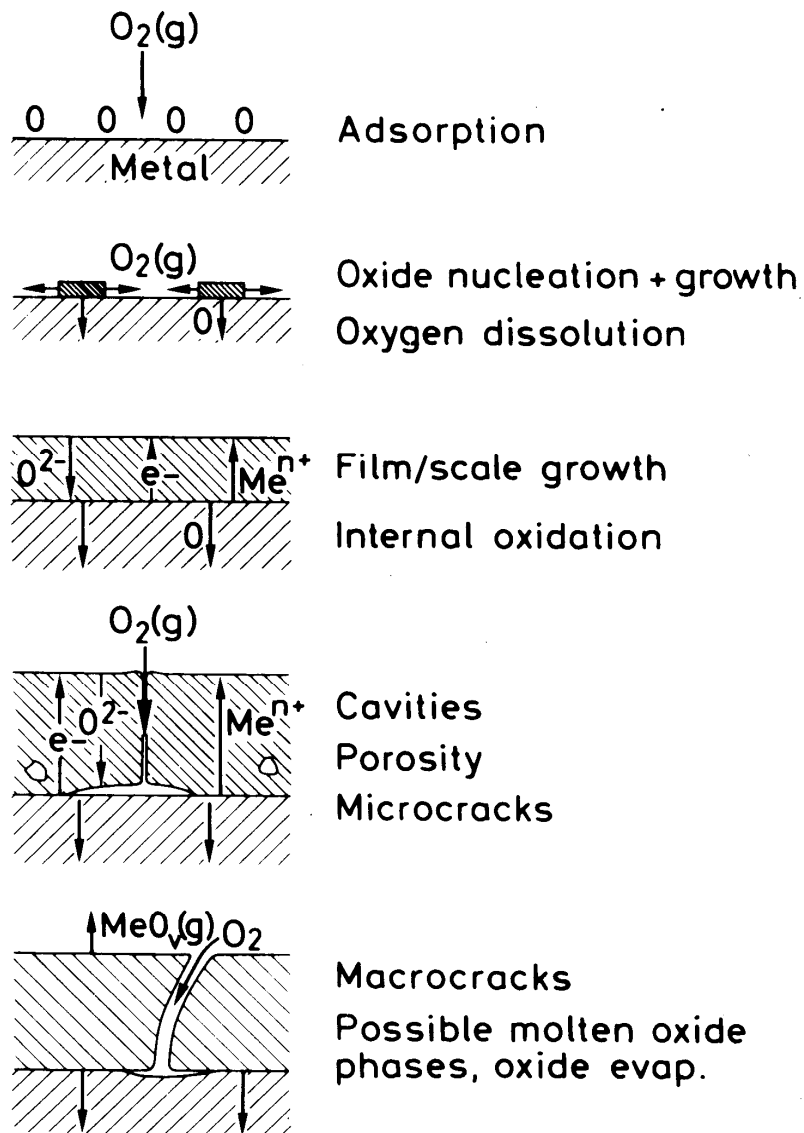


Figure 2.6: Schematic illustration of metal-oxygen reaction [57].

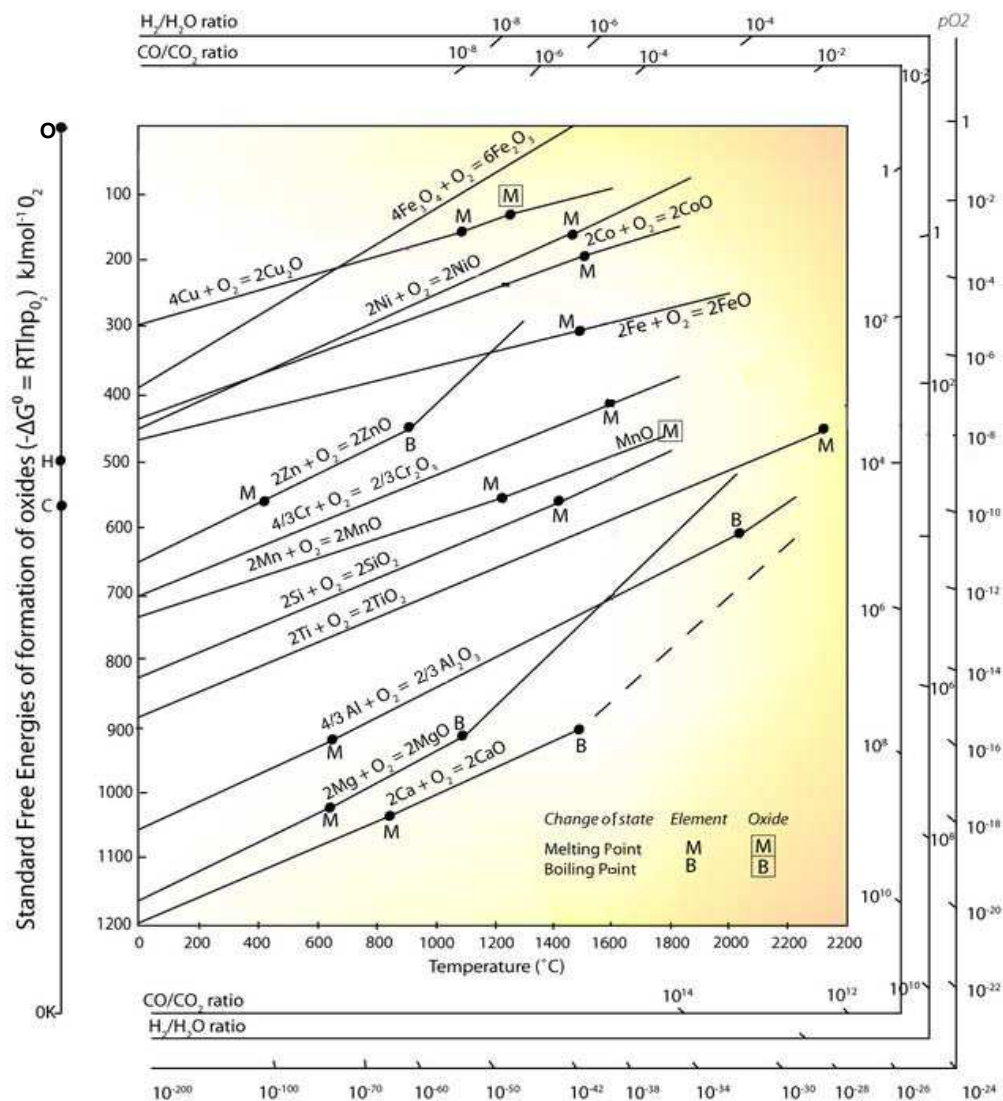


Figure 2.7: Standard Gibbs energies of formation of selected oxides as a function of temperature [59].

2.5.2 Pilling-Bedworth Ratio (PBR)

The resistance of a metal to high temperature oxidation requires the formation of a protective barrier and the maintenance of this protection is required in order to achieve continuous resistance. The characteristics of the oxide scales formed play an important role in the oxidation process of any metal. As oxide scales grow, stress generation may cause scale cracking and spallation. The stresses developed during

scale formation are usually classified as: growth stresses, transformation stresses which occur when a crystallographic phase transformation takes place, and thermal stresses due to the thermal expansion between oxide and metal. Although the precise origin of the growth stress is complex and not fully understood, it is believed that is strongly affected by the volumes of metal and oxide; the crystal structures of oxide and metal, and the oxide growth mechanism [60].

In 1923 Pilling and Bedworth [61] classified oxide scales into two main classes according to the protective properties of the scales; those which form protective oxides, and those which cannot. The type of oxide scales that form is dependent on the relative volumes of both the metal and the resulting oxide. The ratio of these volumes is the Pilling-Bedworth ratio:

$$PBR = \frac{V_{ox}}{V_m} \quad (2.6)$$

where V_{ox} and V_m are the volume of the oxide and the metal respectively. If PBR is less than 1, the oxide scale is porous and un-protective. If PBR is equal or more than 1 a protective scale is formed, the oxidation can proceed only by solid-state diffusion. The larger the deviation of PBR from 1, the larger the growth stress. For PBR greater than 2, large compressive stresses may cause the scale to crack or flake off, continually exposing a fresh unprotected metal surface.

Exceptions to the PBR rules are numerous. Many of the exceptions can be attributed to the mechanism of the oxide growth since the PBR theory is based on the assumption that oxygen needs to diffuse through the oxide layer to the metal surface; but in reality, it is often the metal ion that diffuses to the air-oxide interface.

Nevertheless, Pilling and Bedworth made the first step in achieving understanding of the metal-gases reaction process. The volume ratio, as a rough rule-of-thumb, is usually correct [56]. Table 2.6 lists the PBRs for some common oxides.

Table 2.6: Oxide-metal volume ratios of some common metals. [Source 56, 58].

Oxide	Volume Ratio
Al_2O_3	1.28
Cr_2O_3	2.07
$\alpha\text{-Fe}_2\text{O}_3$	2.15
Fe_3O_4	2.10
Nb_2O_5	2.68
SiO_2	2.15
TiO_2	1.76
WO_3	3.30

2.5.3 Kinetics of Oxidation

The study of the reaction rates and kinetics is imperative in order to understand the high temperature oxidation of metals. Rates of reaction and the corresponding rate equations depend on a number of factors such as temperature, oxygen pressure, time, and surface preparation. These equations are often used to classify the oxidation behavior of metals; the rate equations commonly encountered are linear, parabolic, and logarithmic. Deviations from these reaction rates or combinations are also often encountered. At high temperatures, metals and alloys may have a combination of linear and parabolic oxidations. Since the oxidation products are often retained on the metal surface, the rate of oxidation is usually measured as weight gain per unit area. Figure 2.8 presents typical oxidation rate curves showing the

relationship between weight gain versus time for the most common oxidation kinetics, the slope of the curve determines the oxidation rate.

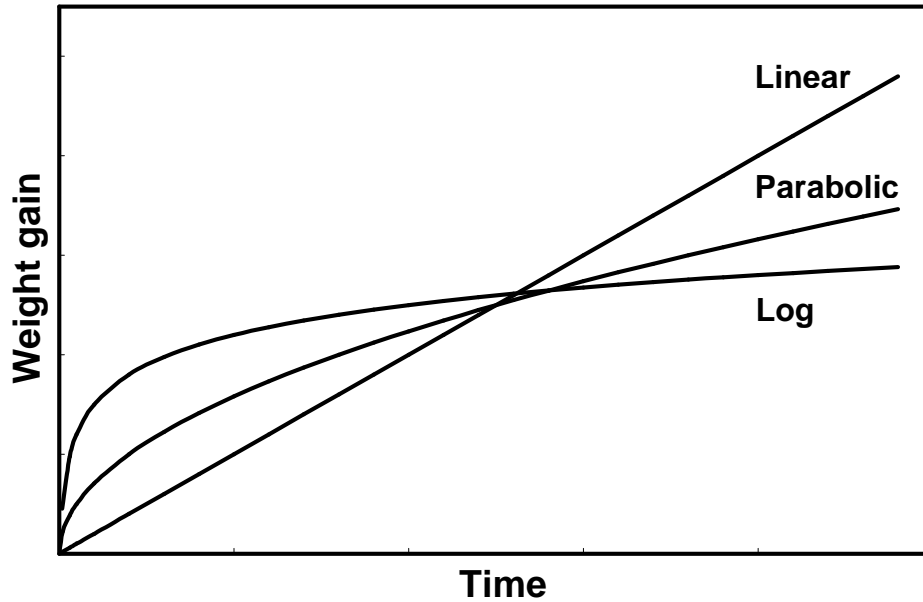


Figure 2.8: Variation of weight gain with time for linear, parabolic and logarithmic oxidation.

2.5.3.1 Linear Kinetics

The rate of oxidation remains constant with time and it is independent of the amount of metal previously consumed in the reaction. The rate of this type of reactions is usually controlled by a surface-reaction step or by diffusion through the gas phase. The rate of reaction is directly proportional to the time; linear oxidation may be described using the equations:

$$\frac{dx}{dt} = k_l \quad (2.7)$$

$$x = k_l t \quad (2.8)$$

where x is the mass or thickness of the oxide formed, t is the exposure time, and k_l is the linear rate constant. Linear oxidation occurs when the oxide scale forming on the metal surface provides no protection, which is usually caused by oxide cracking or spallation due to internal stresses, porous scales, or the formation of volatile or molten oxides.

2.5.3.2 Parabolic Kinetics

At high temperatures the oxidation of many metals follows parabolic kinetics. The oxidation reaction is controlled by the diffusion of ions through the oxide scale. As the oxide grows thicker, the diffusion distance increases causing the oxidation rate to decrease, therefore the oxidation rate is inversely proportional to the thickness or the weight of the oxide scale formed, this is represented as:

$$\frac{dx}{dt} = \frac{k_p}{x} \quad (2.9)$$

$$x^2 = k'_p t \quad (2.10)$$

where k_p is the parabolic rate constant.

2.5.3.3 Logarithmic Kinetics

In this case the reaction is initially rapid and then stabilizes to low or negligible rates. Logarithmic oxidation occurs at low temperatures when a very thin film of oxide is formed. There are a number of theories to explain this behavior; most of them are

based on the transport of either ions or electrons. The logarithmic rate and the inverse logarithmic rate can be expressed using the following equations:

$$x = k_e \log(at + 1) \quad (2.11)$$

$$\frac{1}{x} = b - k_i \log t \quad (2.12)$$

where k_e , and k_i , are the rate constants for logarithmic and inverse logarithmic process, and a , and b are constants.

2.5.4 Temperature Dependence of Oxidation

Numerous experimental studies of oxidation reactions have shown that the temperature dependence of the oxidation rate constants at constant ambient oxygen pressures obeys an Arrhenius-type equation [57, 62]:

$$k = k_o \exp(-Q/RT) \quad (2.13)$$

where Q is the activation energy of the oxidation reaction, R is the gas constant and T is the absolute temperature. The rate constant k can be obtained from isothermal oxidation tests at different temperatures. When k is plotted on a logarithm scale as a function of $1/T$, the slope of the resulting straight line represents $-Q/R$. Activation energy remains constant as long as the rate determining mechanism prevails, changes in temperature dependence may indicate changes in the oxidation mechanism. However a change in the activation energy is not sufficient condition to conclude that a change in the reaction mechanism occurred. In Wagner's theory for

parabolic oxidation the rate constant is related to the self diffusion coefficient of the ions in the oxide scale [57, 62].

2.5.5 Oxidation of Alloys

The oxidation of alloys involves the same general phenomena described for pure metals. However, alloys in general contain two or more oxidizable constituents, therefore the oxidation is generally more complex since additional factors and parameters must be taken into account. Several factors determine the effect of alloying additions on the oxidation process [58]:

1. The alloying elements will have different diffusivities.
2. The elements in the alloy will have different affinities for oxygen.
3. Ternary or complex oxides may be formed.
4. A degree of solubility may exist between the oxides.
5. The metals ions will have different mobilities in the oxide phases.
6. Dissolution of the oxygen into the alloy may result in internal oxidation.

Experimental studies have demonstrated that it is not possible to describe the oxidation of multiphase alloys using a common mechanism. Gesmundo et al. [63] presented three corrosion behaviors observed in two phase alloys, which include: (1) independent oxidation of individual phases, (2) cooperative oxidation to form a uniform scale, and (3) exclusive oxidation of a single phase acting as an effective solute reservoir for the exclusive growth of a slow growing, protective scale. Examples of these behaviors are presented schematically in Figure 2.9.

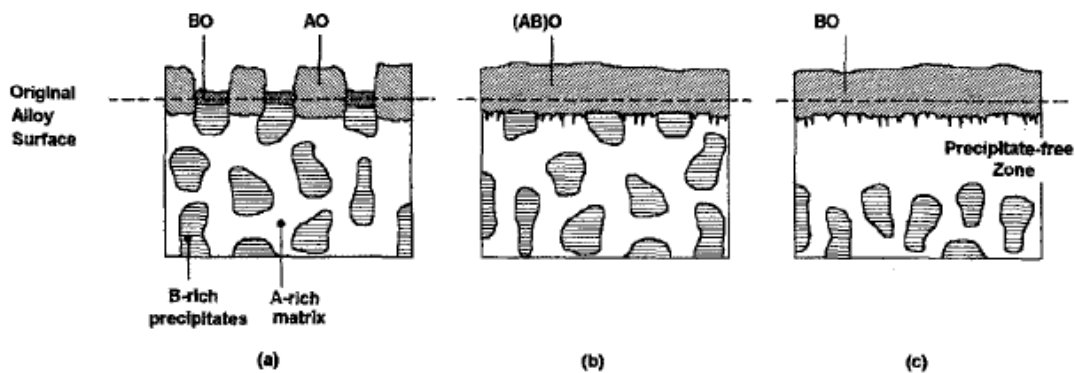


Figure 2.9: Various oxidation behaviors observed in two phase alloys. (a) Independent oxidation to form a non-uniform scale. (b) Cooperative oxidation forming a uniform scale. (c) Solute rich second phase acts as a reservoir for the growth of the solute scale [63].

2.5.6 Oxidation Theories

The study of the oxidation of metals has been a subject of considerable research effort for many years. First studies were basically concerned with the corrosion of pure metals and single-phase alloys. Fundamental studies of the oxidation of metals date back to the classical works of Tammann (1920) and Pilling and Bedworth (1926), followed by the work of Wagner (1933).

The oxidation of single-phase alloys may lead to the formation of a mixed oxide scale on the surface or the exclusive formation of the most stable oxide of the alloy constituents, which in most cases is a slow growing oxide scale. The theory developed by Wagner provided a quantitative, experimentally verifiable model for scale growth on single-phase alloys and established the basic mathematical model of parabolic oxidation upon which most thick-film models are based [64]. Wagner's oxidation theory [65] showed that if the volume diffusion of the ions or electrons

through a compact oxide scale determines the oxidation rate, a parabolic rate law results. Wagner's theory is based upon the following assumptions:

1. The oxide layer is a compact, perfectly adherent scale.
2. Migration of ions or electrons is the rate controlling process.
3. Thermodynamic equilibrium at the metal-scale and scale-gas interfaces.
4. Oxygen solubility in the metal may be neglected.

The theory predicts the minimum concentration of alloying constituents required to form an external protective oxide scale. An expression for the parabolic rate constant (k_p) in terms of the electronic and ionic conductivity of the oxide or alternatively in terms of the self diffusion coefficients of the reacting ions is derived [57].

For an alloy A-B, the minimum concentration of the more reactive component B required for its exclusive oxidation on the surface of a single-phase binary alloy is given by:

$$N_B^* = \frac{V}{z_B M_o} \left(\frac{\pi k_p}{D} \right)^{1/2} \quad (2.14)$$

where N_B^* is the minimum concentration of B necessary to form BO, V is the molar volume of the alloy, z_B is the valence of B, M_o is the atomic weight of oxygen, D is the diffusion coefficient of B in the alloy, and k_p is the parabolic rate constant for growth of BO.

The Wagner's model was developed for single-phase alloys; an extension of this theory to include two-phase systems has been proposed by Wahl [66]. The treatment by Wahl is the simplest of the multiphase treatments, it assumes that the

alloy comprises two phases: (1) a matrix phase containing the oxide forming element M; (2) a precipitate phase which is rich in M and it is the source of metal for the oxide formation. During oxidation, the precipitates close to the surface dissolve into the matrix supplying the element M required for the oxide formation on the surface, creating a precipitate-free zone adjacent to the metal interface. The process where precipitates act as a source of solute for the continued exclusive growth of the MO oxide scale is known as reservoir effect. The model used by Wahl is presented in Figure 2.10. The exclusive formation of the most stable slow growing oxide scale can be achieved if the following condition is satisfied [67]:

$$\sqrt{N_M^o N_M^{tot}} > \frac{V}{V_o} \left(\frac{\pi k_p}{2D} \right)^{1/2} \quad (2.15)$$

where N_M^o and N_M^{tot} are the mole fractions of component M in the matrix phase and in the alloy, V and V_o are the molar volumes of the alloy and the oxide MO, D is the interdiffusion coefficient for the matrix, and k_p is the parabolic rate constant for growth of MO. One of the limitations of Eq. 2.15 is that it does not take into account the kinetics of particle dissolution, which can be greatly affected by size, shape and distribution of precipitates.

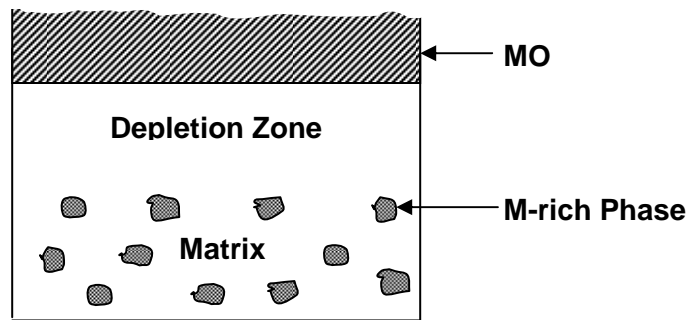


Figure 2.10: Schematic illustration of Wahl's model.

Additional oxidation models for treating the oxidation behavior of two-phase binary alloys have also been proposed by Wang et al. [68, 69] and Gesmundo et al. [63, 70]. Wang et al. [68] found that in addition to the critical amount of element M, the exclusive formation of solute oxide on a two phase alloy can be achieved by increasing the volume fraction of the second phase. Fine, homogeneous and randomly distributed precipitates are more favorable than coarse precipitates. Gesmundo et al. [71] derived the general relation between parabolic rate constant of a two-phase alloy in terms of volume fractions and the parabolic rate constants of the constituent elements. This theory also elucidates the effects of size and distribution of the second phase particles in the overall oxidation kinetics. Gesmundo et al. [72] also studied the conditions from the transition from simultaneous oxidation of the two components to exclusive oxidation of the element forming the most stable oxide taking into account the effect of the displacement of the outer alloy surface with time.

A cyclic oxidation model for multiphase Nb alloys was developed by Chan [6]; this model indicates that the oxidation resistance of two-phase Nb alloys depends on the volume fraction and particle size of the Laves and silicide phases.

2.6 Oxidation Resistance of Nb and Nb-Based Alloys.

In common with other refractory metals, niobium and its alloys tend to oxidize in air at high temperatures. The high temperature oxidation of Nb is characterized by inward diffusion of oxygen through the scale. Initially a protective scale is formed; as the scale grows, stresses are created at the metal-scale interface which results in scale cracking often referred as “breakaway” oxidation [73].

2.6.1 Oxidation of Nb

The oxidation of niobium is rather complex. The oxidation mechanism can be parabolic or linear depending on the temperature, the oxygen pressure and the oxidation time.

Hurlen [74] performed an extensive study of the reaction of niobium with oxygen at different pressures and temperatures from 150°C-1000°C. According to this study, the sequential stages in the oxidation of Nb are: linear (I), parabolic (II), a rate-increasing transition, linear (III), parabolic (IV) and parabolic (V).

A review of the oxidation kinetics of niobium was presented by Kubaschewski and Hopkins [75]; and the sequential steps in the oxidation mechanism can be described as:

- (a) Parabolic growth of a dense oxide scale surface from 300°C to 500°C.
- (b) Linear growth rate from 500°C to 1000°C caused by cracking and spalling of the dense layer.
- (c) Accelerated oxidation from 1100°C to 1250°C.
- (d) Extremely rapid oxidation at temperatures above 1300°C.

Expansion of the niobium lattice upon solution of oxygen indicates that the oxygen dissolves interstitially. Brauer [76] estimated that the solubility limit of oxygen in niobium to be less than 4.7 at% at 1600°C-1700°C. Seybolt [77] reported values of 1.4 at% at 775°C and 5.5 at% at 1100°C. Bryant [78] has determined that the solubility ranges from 0.7 at% at 750°C to 5.5 at% at 1540°C. According to Elliot [79] the oxygen solubility rises from 1.4 at% at 500°C to 3.9 at% at 1800°C.

Brauer [76] identified NbO , NbO_2 , and Nb_2O_5 , as the only equilibrium oxides of niobium, with Nb_2O_5 having three polymorphs. The main features of the Nb-O diagram have been established by Elliot [79]. The phase diagram for the Nb-O system is presented in Figure 2.11. According to this diagram, the solubility of oxygen in $\alpha\text{-Nb}$ varies from 1.4 at% at 500°C to 4.0 at% at 1915°C . NbO_2 and NbO melt congruently at 1915°C and 1945°C respectively, while Nb_2O_5 melts at 1495°C [80, 81].

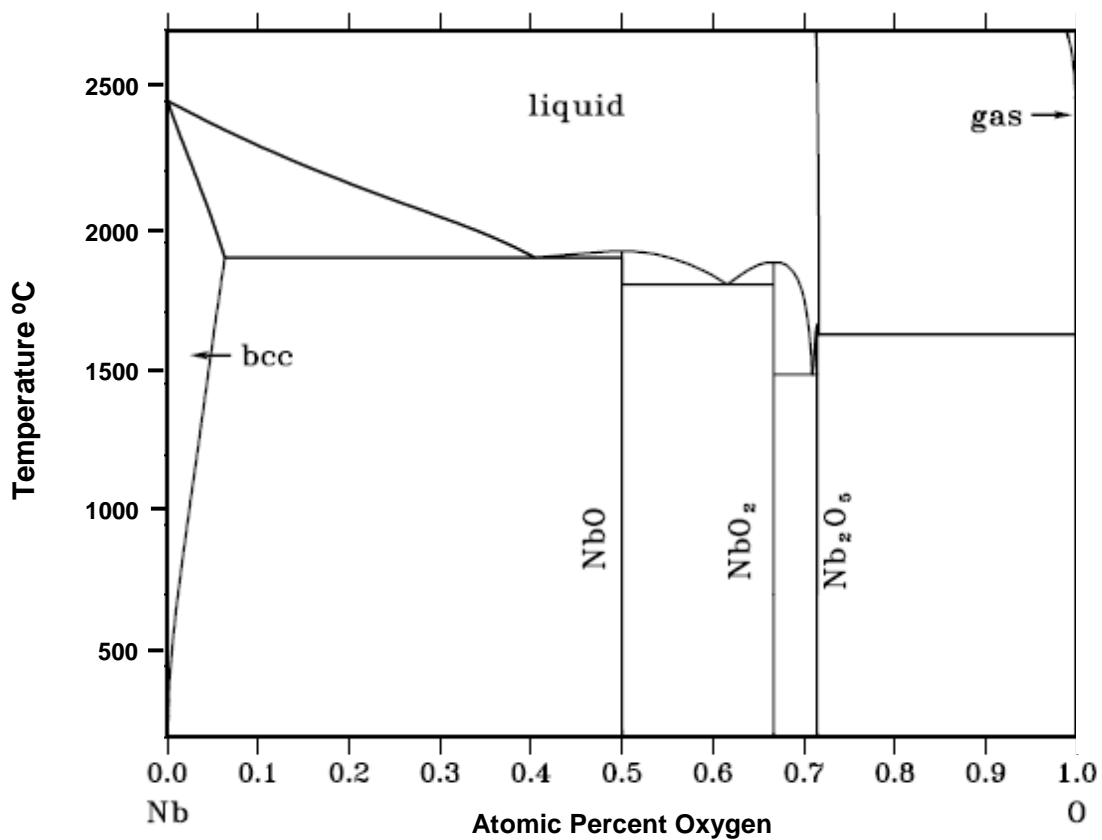


Figure 2.11: Calculated phase diagram for the Nb-O system adapted from Franke et al. [82].

The niobium pentoxide has several modifications that are identified with a variety of prefixes. Classification of the modifications of Nb_2O_5 is confusing since uncorrelated nomenclature is used to designate the polymorphs. Brauer distinguished three modifications [76]:

- T-Nb₂O₅ (low temperature) stable up to 900°C.
- M-Nb₂O₅ (medium temperature) stable between 900°C and 1100°C
- H-Nb₂O₅ (high temperature) stable at temperatures above 1100°C.

Goldschmidt [83] re-investigated the polymorphic forms, reporting two modifications:

- α -Nb₂O₅ (Orthorhombic): It is also called “low temperature” modification, is metastable and transforms spontaneously to β -Nb₂O₅.
- β -Nb₂O₅ (Monoclinic): It is also called “high temperature” modification and is the stable form between 600°C and 1230°C.

Other modifications have been found and numerous observations have been made regarding the modes of formation, structure and stabilities. A comprehensive review and classification of the modifications of niobium pentoxide was made by Schäfer et al. [84].

2.6.2 Oxidation of Nb Alloys

Although a considerable amount of research has been carried out on the oxidation characteristics of Nb-based alloys, very little information is available on the conditions required for the formation of protective oxide layer. Published research has shown that the scale formed on niobium above and about 600°C is porous and non protective [85]. The first goal of the alloying addition is to provide a scale that is tight and adherent, and whose rate of growth is diffusion-controlled. The rate of growth of this scale may then be further improved by additional alloying.

The majority of the initial research was focused on alloying Nb with different elements to reduce the oxidation kinetics. These studies, reviewed extensively by Stringer [86], indicated that the formation of Nb_2O_5 was too dominant to be altered by the alloying additions [6].

Subsequent studies focused on the oxidation characteristics of Nb-Al alloys and the formation of a protective Al_2O_3 scale. The Nb-Al system has three intermetallics, Nb_3Al , Nb_2Al , and NbAl_3 . The oxidation characteristics of the phase NbAl_3 have been studied by several researchers since it is the only intermetallic phase that forms Al_2O_3 when oxidized at high temperatures (1000°C) [8, 87-89], however this phase cannot sustain the growth of a protective oxide layer. The selective oxidation of the aluminum results in the surface stabilization of the non-protective niobium oxides [88-90]. The oxidation resistance of Nb-Al alloys may be increased by adding elements that decrease the diffusivity of oxygen and increase that of aluminum in the metal matrix. Additions of Ti, V, Cr have been used for this purpose, however these elements also decrease the melting point and have negative effects on the mechanical properties [90]. A study of NbAlCrY alloys performed by Hebsur et al. was oriented to improve the oxidation behavior of NbAl_3 based alloys [91]. The intent was to expand the NbAl_3 phase field to lower aluminum levels such that oxidation to form Al_2O_3 would delay the eventual formation of the Nb_2Al in the alloys. The oxidation behavior of the alloys was improved; however, the protective scale formation appeared to be related to the Cr-rich intermetallic grain boundary phases rather than the NbAl_3 -base matrix [8].

In the last several years considerable research efforts at a number of institutions have led to the development of multicomponent, two/three-phase, alloys with Nb-solid solution and intermetallic (silicides or Laves) phases.

Extensive studies performed on two-phase Nb-Nb₅Si₃ system indicated that the alloys from this system have a really attractive balance of high and low temperature mechanical properties, unfortunately, the composites from binary Nb-Si alloys still suffer from catastrophic oxidation upon exposure to air at temperatures above 500°C [9, 13]. The Nb-Nb₅Si₃ alloys oxidize mainly by oxygen diffusion, with the rapid formation of stratified and porous layers, which spall off easily [13]. The studies performed on this system have evolved gradually from a binary model system to a multiphase, multicomponent system of Nb with the additions of Ti, Al, Hf and Al [1, 3, 9, 10, 13, 14, 17, 92]. Subramanian et al. [93] examined the oxidation behavior of Nb-(10-20)Si alloys with ternary Mo, W, V, Ti, Zr, and Ru additions as well as quaternary Nb-Si-Ti-Al alloys. The study showed that the most promising alloys systems were those with Ti and Al additions to Nb-Si alloys.

Menon et al. [94] reported the oxidation behavior of several Nb-Si with different alloying elements. The oxidation products observed include TiNb₂O₇, CrNbO₄, SiO₂, 3Nb₂O₅·TiO₂, and Nb₂O₅. The results also indicated that the Nb solid solution phase oxidizes selectively.

The oxidative instability of Nb-Si alloys led the researchers to add small amount of boron to imitate the Mo-Si-B system to form a protective borosilicate glass layer. Studies performed by Murakami et al. [95] indicated that the scale formed consisted of Nb₂O₅, SiO₂ and a large number of pores and no continuous glass layer was

observed. Liu et al. [96] and Behrani et al. [13] also studied the oxidation properties of Nb-Si-B alloys and reported that the oxidation behavior of alloys from this system is inferior to that of the Mo-Si-B system. The difference in oxidation stability of boron modified Mo-Si and Nb-Si may be attributed to the non-volatile nature of the oxide formed and the high porosity of the scale on Nb-Si-B alloys [13].

Refractory metals and their alloys can suffer from pest damage at intermediate temperatures ($<850^{\circ}\text{C}$) [92]. Niobium has a high solubility for oxygen, and its silicides also suffer from pest oxidation [10]. Additions of Al and Hf are known to reduce the pesting susceptibility of Nb-based alloys, but some Nb-silicide based composites can still be attacked [1]. Bewlay et al. reported that alloying with Sn has been very effective in managing pesting damage [2]. Studies performed by Geng et al. revealed that additions of 5 at% can significantly control pest oxidation behavior [14, 92].

The addition of Cr has been found to improve the oxidation resistance which has been attributed to the stabilization of the NbCr_2 Laves phase [14]. The results of oxidation resistance in air for the alloys Nb-20W-5Cr and Nb-20W-10Cr have been reported by Kakarlapudi et al. and Portillo et al. [23, 24]. The study indicates that alloys containing higher chromium concentration and second phase intermetallic particles exhibit enhanced oxidation resistance than alloys without second phase particles. The mechanism(s) by which chromium additions improve the resistance to oxidation have not been completely understood.

Cyclic oxidation studies performed by Chan [6, 12] on multiphase alloys, containing silicide, Laves and Nb solid solution phases, indicated that the oxidation

products are mainly CrNbO_4 , Nb_2O_5 , and $\text{Nb}_2\text{O}_5\cdot\text{TiO}_2$. The oxidation resistance was improved when CrNbO_4 formed instead of Nb_2O_5 .

The oxidation resistance of multiphase Nb-based alloys is substantially better than that of niobium and conventional Nb alloys; and it is comparable to that of Ni-based superalloys at 1000°C . The numerous studies performed provide evidence that these alloys could meet the required oxidation resistance goal for a metal surface temperature at 1315°C . The short-term goal is for a loss of $<200\text{ }\mu\text{m}$ in 10 hours at $1370\text{ }^\circ\text{C}$. The long-term goal is for a loss $<25\text{ }\mu\text{m}$ in 100 hours at $1315\text{ }^\circ\text{C}$ [2, 97]. This is derived from the requirement of achieving the oxidation life at 1315°C that the 2GSX nickel-based superalloys presently exhibit at 1150°C .

CHAPTER 3

EXPERIMENTAL METHODS

3.1 Preparation of the Alloys

The alloys were fabricated by the Ames Laboratory of Iowa State University using arc melting technique. Nb, W, and Cr with at least 99.9% purity were melted on a water-cooled copper crucible in an atmosphere of high purity argon gas; the samples were remelted several times to ensure chemical homogeneity. The alloys were cast into ingots with dimensions of 50 x 50 x 6 mm; final dimensions were obtained using electro-discharge machining (EDM).

The selection of specific alloy compositions has been based on the ternary isothermal sections of Nb-Cr-W diagrams at 1000 and 1500°C (Figure 2.5). Table 3.1 presents the nominal compositions of the alloys used for this study.

Table 3.1: Nominal compositions of Nb-Cr-W alloys.

Alloy Identification	Composition (% weight)			Composition (% atomic)		
	Nb	Cr	W	Nb	Cr	W
15Cr	75	15	10	70.2	25.1	4.7
20Cr	70	20	10	63.2	32.2	4.6
25Cr	65	25	10	56.6	38.9	4.4
30Cr	60	30	10	50.6	45.2	4.2

Isothermal sections of the Nb-Cr-W phase diagram at 900, 1100, and 1300°C were calculated using a phase diagram calculation software for multicomponent systems, PandatTM 7.0 provided by the CompuTherm LLC [98].

3.2 Characterization of the Alloys

Microstructure of the alloys was characterized using optical microscopy (OM), scanning electron microscopy (SEM) and energy dispersive x-ray spectroscopy (EDS). Phases of the alloys were identified by x-ray diffraction (XRD).

The as-cast samples for metallographic analysis were prepared by standard sample preparation techniques. The etchant used was a solution with a proportion 2:1:2 ml of HF, HNO₃, and HCl respectively [99].

3.3 Oxidation Experiments

The oxidation coupons with dimensions of approximately 4.5 x 4.5 x 3.1 mm were ground to 600 grit and ultrasonically cleaned in ethanol before exposure in static air at 900, 1100, and 1300°C. Mass gain per unit area as a function of the temperature has been used to determine the alloy's oxidation resistance, using isothermal and cyclic experiments.

3.3.1 Isothermal Oxidation

Isothermal oxidation tests were carried out in static air at 900, 1100, and 1300°C for 24 hours using a Setaram LabSys evo thermogravimetric analyzer with a heating rate of 23°C/min. The weight gain vs. temperature graphs were obtained using Calisto data acquisition software v1.053.

3.3.2 Cyclic Oxidation

Cyclic oxidation measurements were performed at 900 and 1300°C in a box furnace using a heating rate of 14°C/min, the specimens were placed in alumina crucibles and held at the peak temperature for 4 hours and then furnace cooled to ambient

temperature. The samples were weighed using a Sartorius analytical balance before and after each thermal cycle; this process was repeated for a total oxidation time of 24 hours.

3.4 Oxidation Products Characterization

The oxidation products were characterized by x-ray diffraction (XRD) using a Bruker D8 Discover diffractometer with a voltage and a current of 40 kV and 40 mA respectively and Cu K α radiation ($\lambda=1.54 \text{ \AA}$). The surface morphologies of the oxide and the cross section of the scales were observed and analyzed by SEM and EDS. Microhardness measurements were performed in the as-cast condition and after oxidation experiments using a Struers Durmain A300 microhardness tester.

The characteristics of the equipment used and the parameters for the analysis are summarized in Table 3.2.

Table 3.2: Equipment description and operating conditions.

Equipment/Analysis	Operating Conditions
OM	Reichert MEF4 A/M Optical Microscope with Digital Camera DCM500 Scope Photo Software 3.0
Analytical Balance	Sartorius Analytical Balance Model MC210S
TGA	Setaram LabSys evo thermogravimetric analyzer Calisto data acquisition software v1.053 Rate:23 ^o /min
Microhardness	Struers Duramin-A300 Load:300g Time:15sec Ecos software v.5
Box Furnace	Sentro Tech ST-1600-888 high temperature box furnace with adapted omega s-type thermocouple and DPi32 monitor. Rate:14.4 ^o /min
SEM/EDX	Hitachi S-4800 scanning electron microscope equipped with energy dispersive spectrometer Accelerating voltage:20KV Probe current:20 μ A Working distance:7-15 mm EDAX 5.21 Genesis Imaging/Mapping Software Elapsed live times:30-35sec
XRD	Bruker D8 Discover x-ray diffractometer Radiation:CuK α (λ =1.54 Å) Voltage:40KV Current: 40mA Step:0.05 ^o Scan rate:5 ^o /min

CHAPTER 4

RESULTS AND DISCUSSION

4.1 Isothermal Sections from Nb-W-Cr System

The isothermal sections at 25°C, 900°C, 1100°C, and 1300°C from the Nb-W-Cr phase diagram calculated using Pandat software are presented in Figure 4.1. The four alloys analyzed remain in a two phase region consisting of Nb rich solid solution and intermetallic phase, NbCr₂, through the entire temperature range.

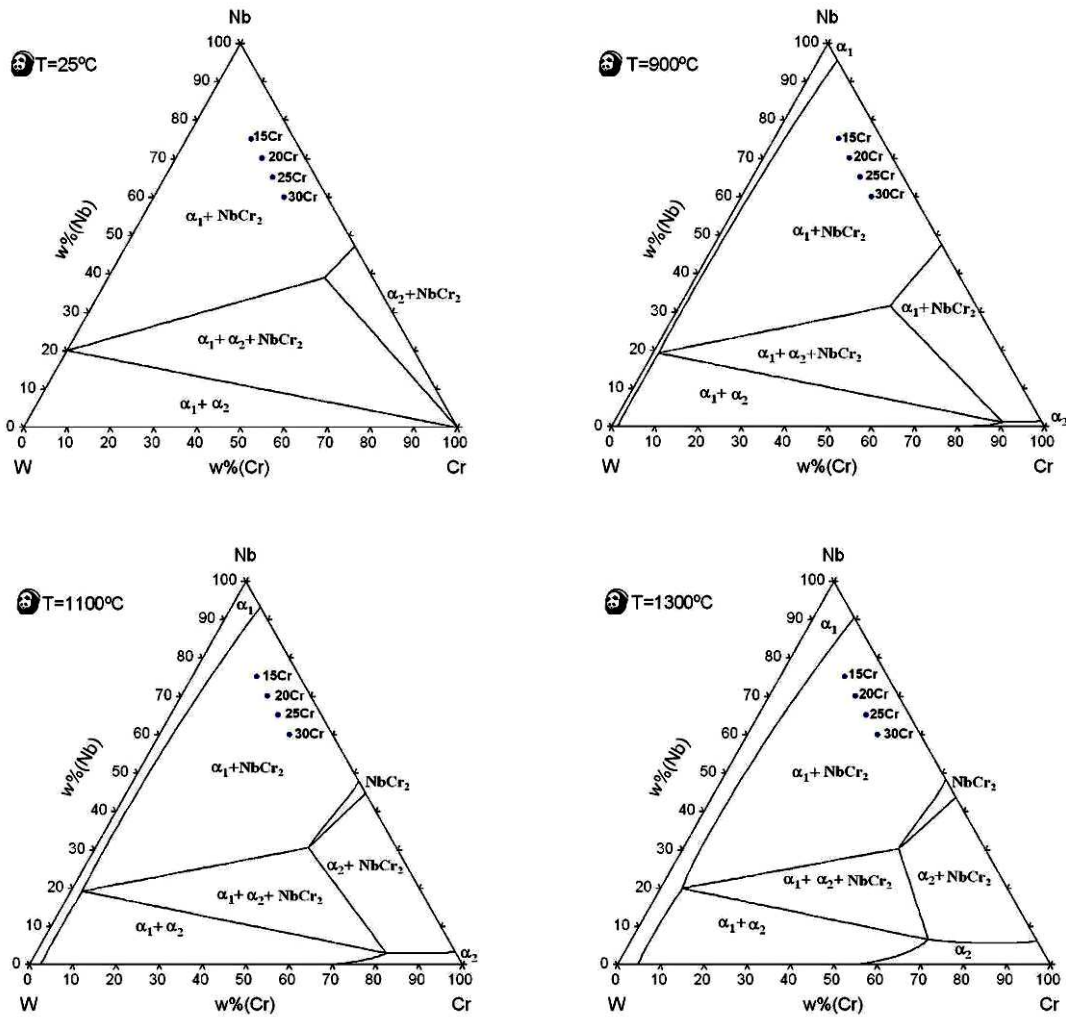


Figure 4.1: Isothermal sections at 25, 900, 1100, and 1300°C for the Nb-W-Cr system calculated by using PandatTM 7.0 software [98].

4.2 Alloys Characterization

Optical images of 15Cr, 20Cr, 25Cr, and 30Cr alloys in the as-cast condition are presented in Figure 4.2. Microstructure of alloys consists of Nb solid solution phase regions (white) and the intermetallic NbCr_2 laves phase (gray), an increase of the intermetallic phase is observed as the Cr content increases.

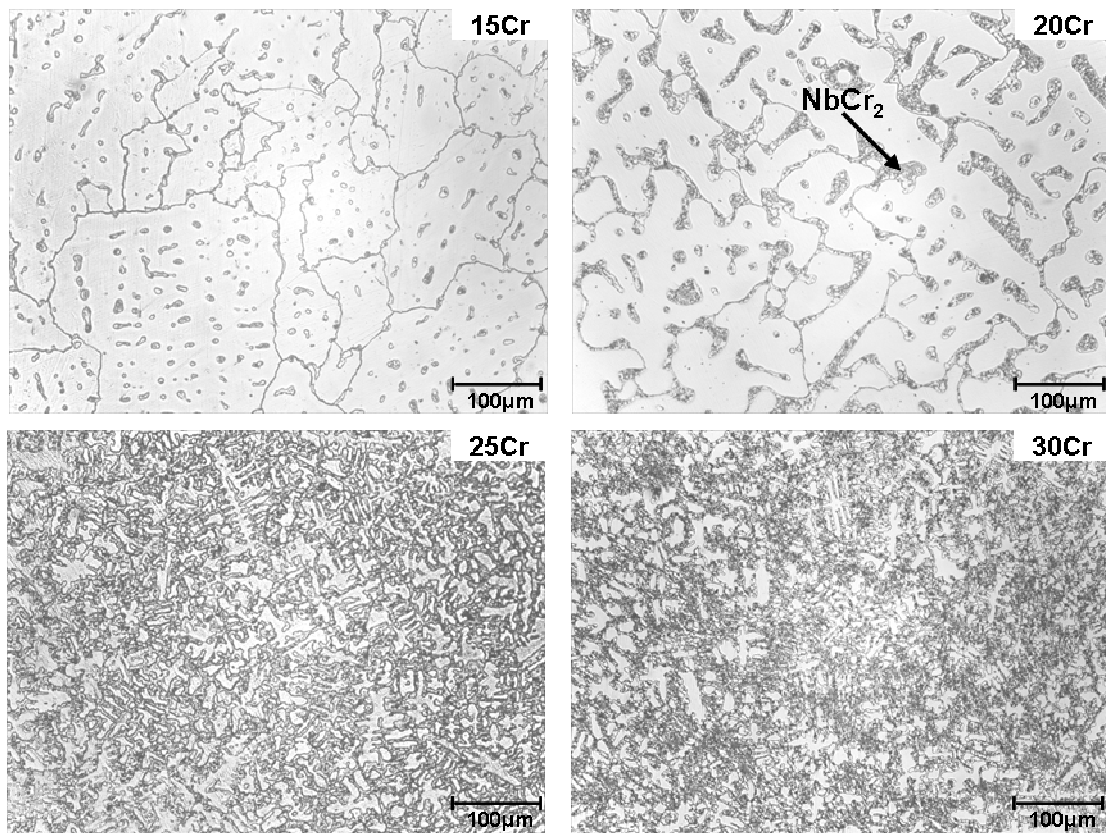


Figure 4.2: Optical images of the as-cast microstructure of Nb-W-Cr alloys.

The BSE images and x-ray maps presented in Figures 4.3 to 4.6 show the two phase structure for the four alloys in the as cast condition.

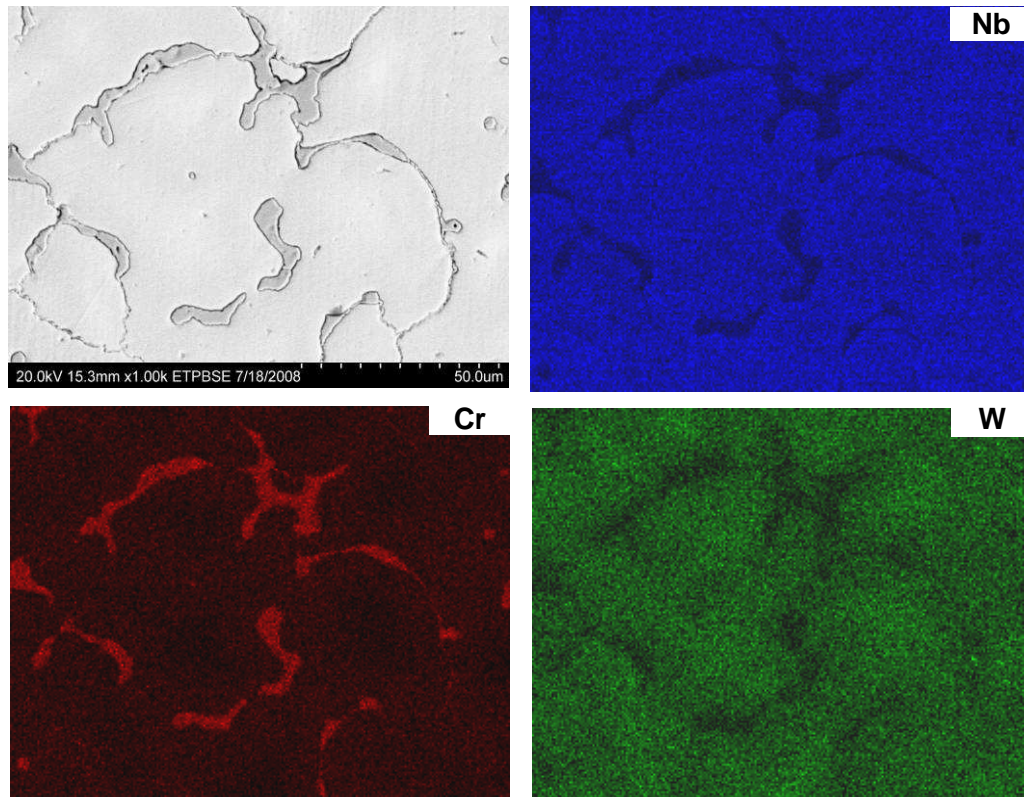


Figure 4.3: BSE image and X-ray maps of 15Cr alloy showing Nb, Cr, and W distribution.

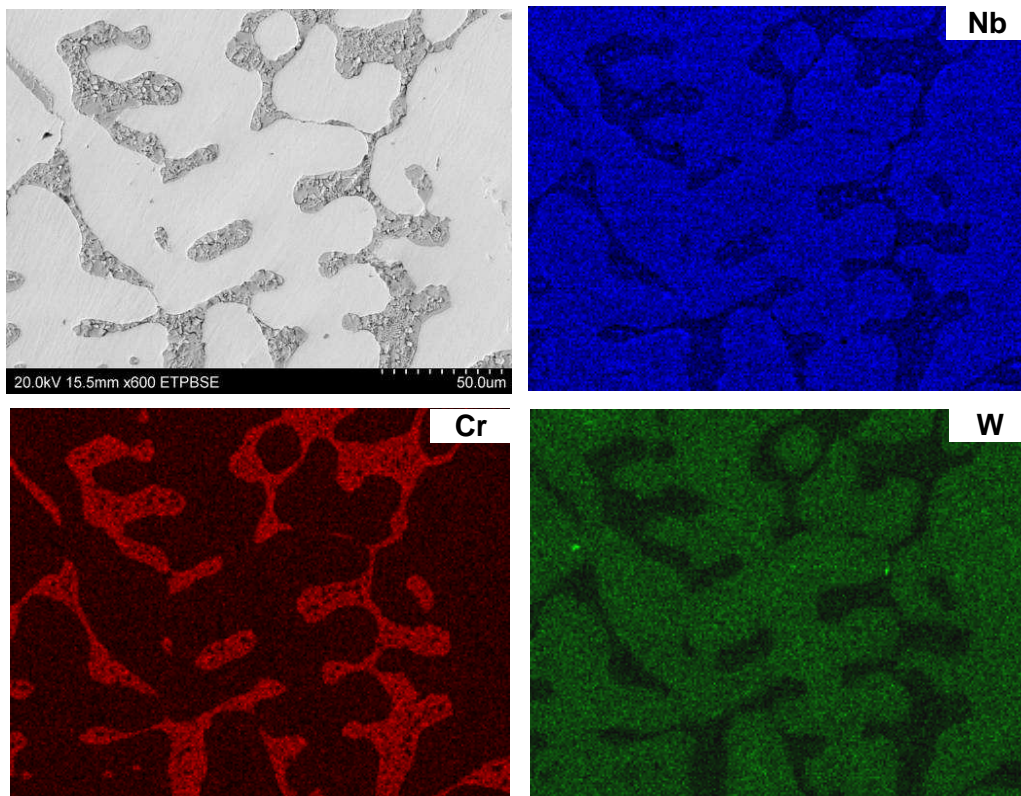


Figure 4.4: BSE image and X-ray maps of 20Cr alloy showing Nb, Cr, and W distribution.

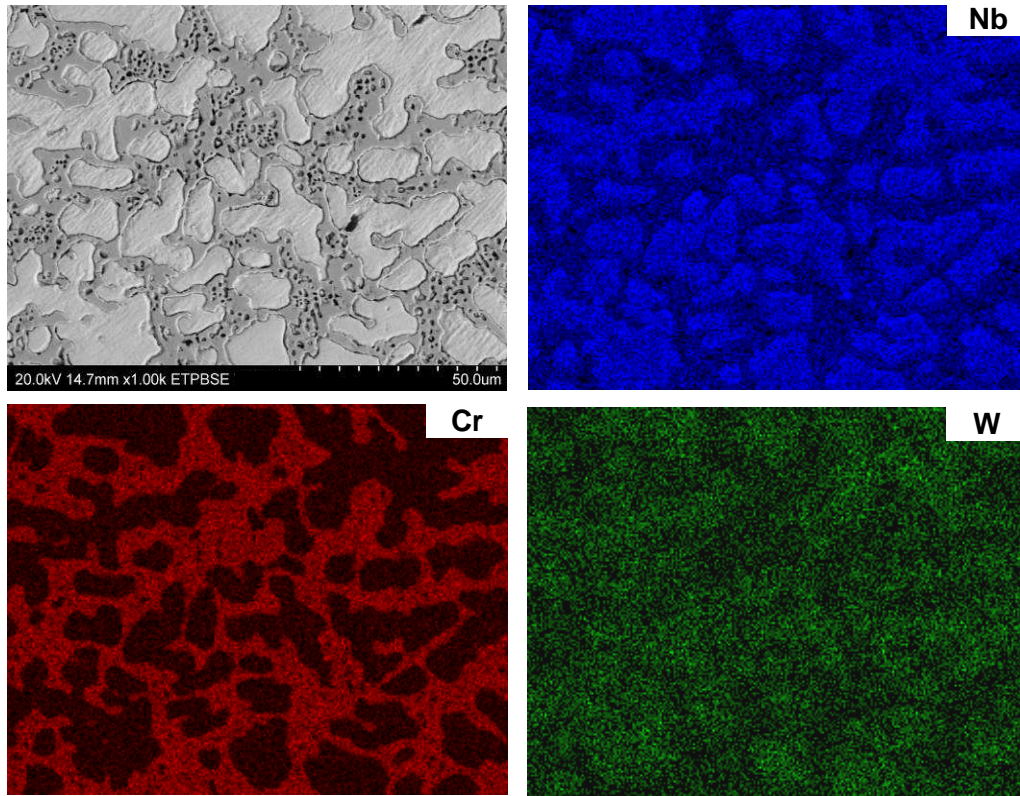


Figure 4.5: BSE image and X-ray maps of 25Cr alloy showing Nb, Cr, and W distribution.

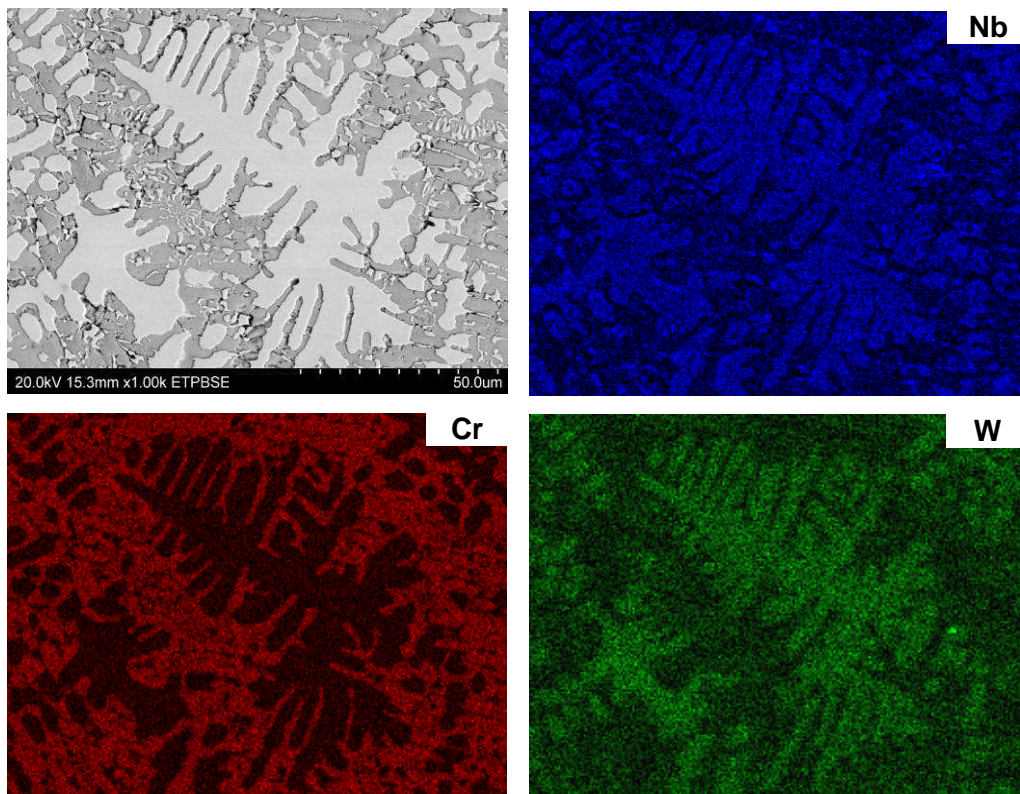


Figure 4.6: BSE image and X-ray maps of 30Cr alloy showing Nb, Cr, and W distribution.

Table 4.1 presents the chemical composition as determined by EDS for each alloy in the as-cast condition, as well as the fraction of the NbCr₂ phase which was measured using image analysis and the BSE contrast. The amount of intermetallic phase increases with the Cr content, the relationship between Cr content as measured by EDS and the fraction of intermetallic and solid solution observed is presented in Figure 4.7.

Table 4.1: Elemental compositions determined by EDS analysis and area fraction of the NbCr₂ phase in the as cast condition.

Alloy	Element (wt%)			NbCr ₂ phase (area percentage)
	Nb	Cr	W	
15Cr	74.5-76.3	12.4-14.0	10.7-12.4	7.6 ± 0.9
20Cr	69.6-71.9	17.1-18.6	10.7-11.9	18.3 ± 1.2
25Cr	62.4-65.7	24.2-26.6	8.9-11.8	43.0 ± 0.8
30Cr	60.9-62.4	28.2-30.3	8.2-9.7	56.7 ± 0.9

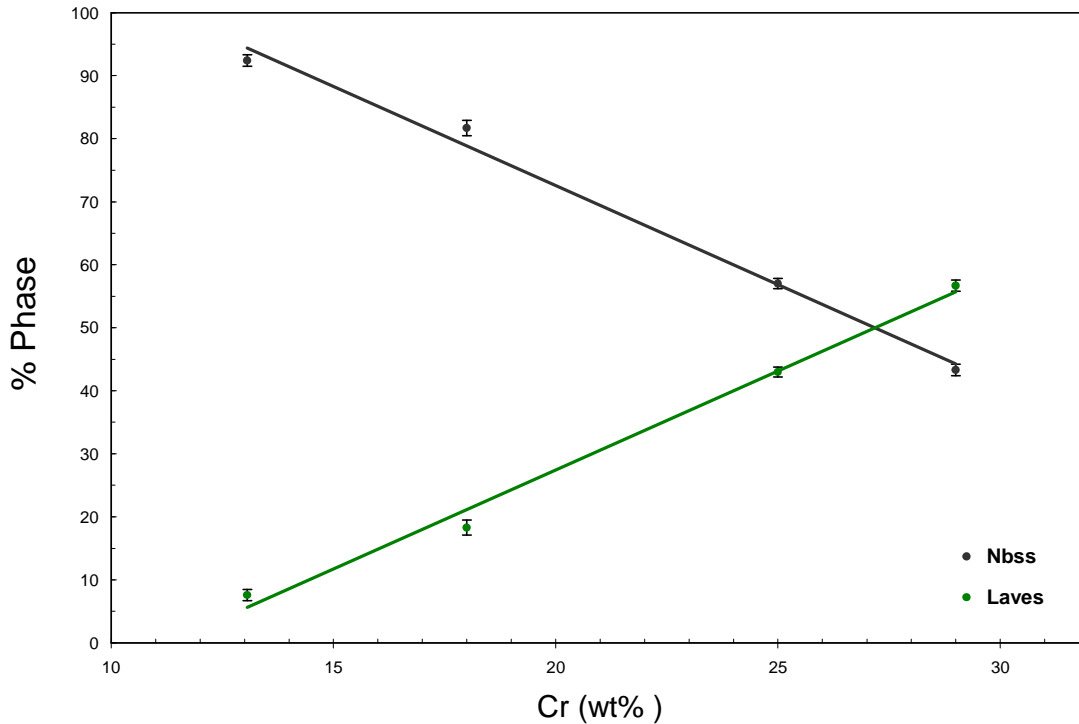


Figure 4.7: Relationship between Cr content as measured by EDS and area fraction of intermetallic and solid solution.

The XRD patterns obtained from the as cast structures are shown in Figure 4.8. Individual phases and their crystal structures were identified by matching the characteristic XRD peaks against JCPDS files. The peak identification confirms the presence of two phases, Nb solid solution (α) and the cubic type laves phase NbCr_2 (C15). The dashed lines represent the diffraction positions of the pure niobium (JCPDS 35-0789). The Nb solid solution peaks in all the as-cast alloys were shifted slightly to the right (higher 2θ values) of the intensity peaks of pure Nb suggesting that the solid solution phase has a reduced lattice parameter compared to pure niobium.

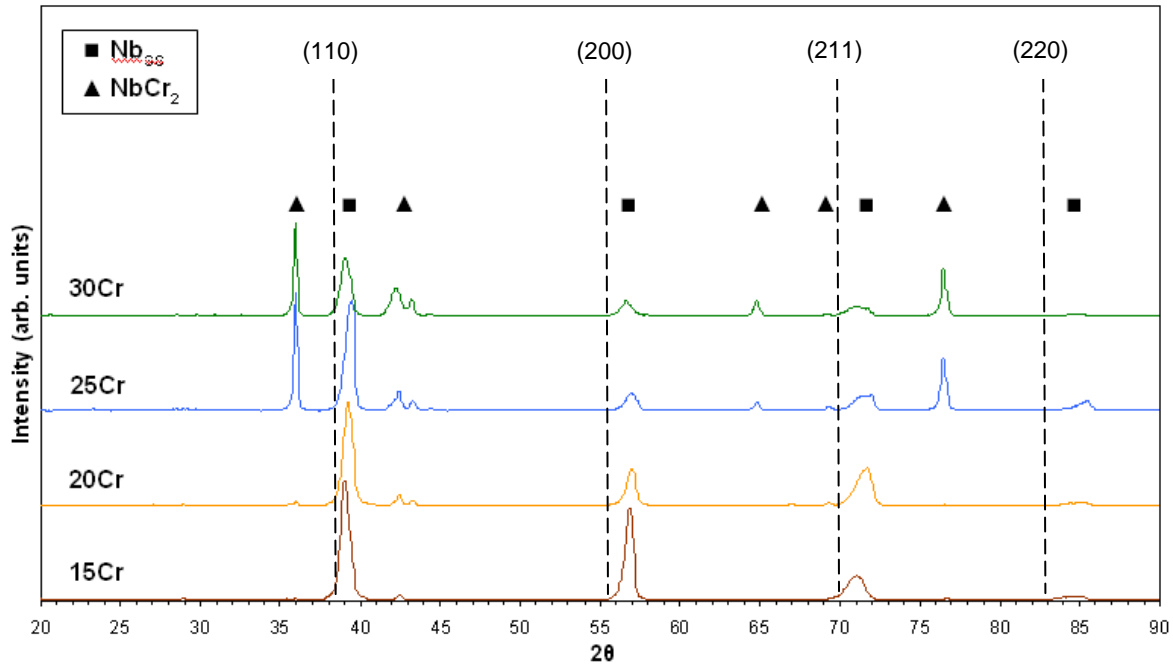


Figure 4.8: XRD patterns of 15, 20, 25, and 30Cr alloys in the as-cast condition.

The lattice parameter a of the bcc Nb solid solution was calculated using the Nelson-Riley extrapolation method and the relation:

$$a = d\sqrt{h^2 + k^2 + l^2} \quad (4.1)$$

where h , k , and l are the plane indices [100]. Figure 4.9 presents the estimated lattice parameters of the Nb_{ss} for the four alloys analyzed and the value for pure niobium (JCPDS 35-0789); the values for the Nb_{ss} in all the as-cast alloys are smaller than the lattice parameter for pure niobium. A trend between the lattice parameter of the Nb_{ss} and the overall Cr content of the alloy was not observed; therefore variations may be related to alloy homogeneity. Since the atomic radii of pure Nb, Cr, and W are 1.47, 1.28, and 1.41 Å respectively [101], a smaller lattice parameter can be attributed to the substitutions of Cr and W in the Nb solid solution, considering only the size effect of substitutional atoms.

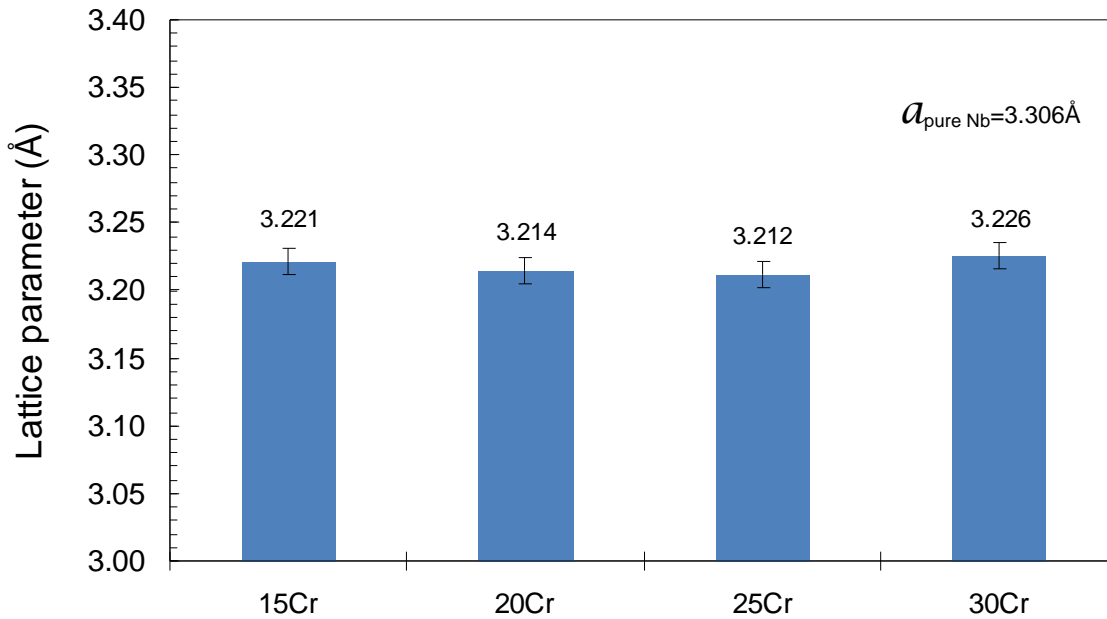


Figure 4.9: Lattice parameters of the Nb_{ss} in the alloys.

Figure 4.10 presents the variation of the hardness with the intermetallic phase volume percentage. The hardness of the alloys increases approximately 60% when the volume percentage of intermetallic phase increases from 7% to 57%.

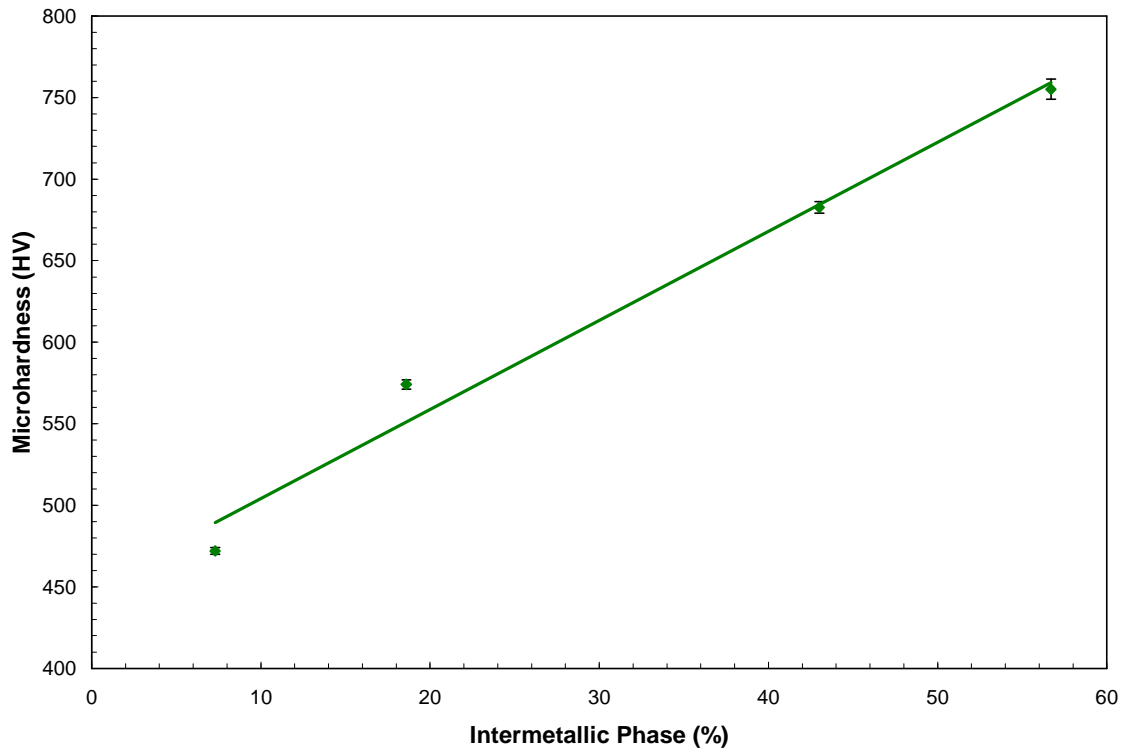


Figure 4.10: Microhardness values of alloys in the as-cast condition and the relationship with the intermetallic phase volume percentage.

4.3 Isothermal Oxidation

4.3.1 Oxidation Kinetics

The oxidation rates of the alloys were measured at 900°C, 1100°C, and 1300°C in static air. Figure 4.11 shows the weight gain per unit area as a function of the exposure time at 1300°C for the alloys 15Cr, 20Cr, 25Cr, and 30Cr. The oxidation behavior of all the alloys follows a parabolic law at this temperature; the time at which the oxidation rate stabilizes depends on the alloy composition. The alloys with higher volume percentage of Laves phase exhibited better oxidation resistance at 1300°C. The weight gain per unit area of the 15Cr alloy is almost 3 times that of the 30Cr alloy, delineating the relationship between the oxidation resistance and the fraction of

intermetallic phase in the alloy. This behavior is in agreement with the results reported for niobium-based alloys in the literature [2, 6, 12].

The large difference in weight gain per unit area between alloys 20Cr and 25Cr and the small difference between alloys 25Cr and 30Cr suggest the existence of a limit concerning the effectiveness of the Cr in improving oxidation resistance of these alloys.

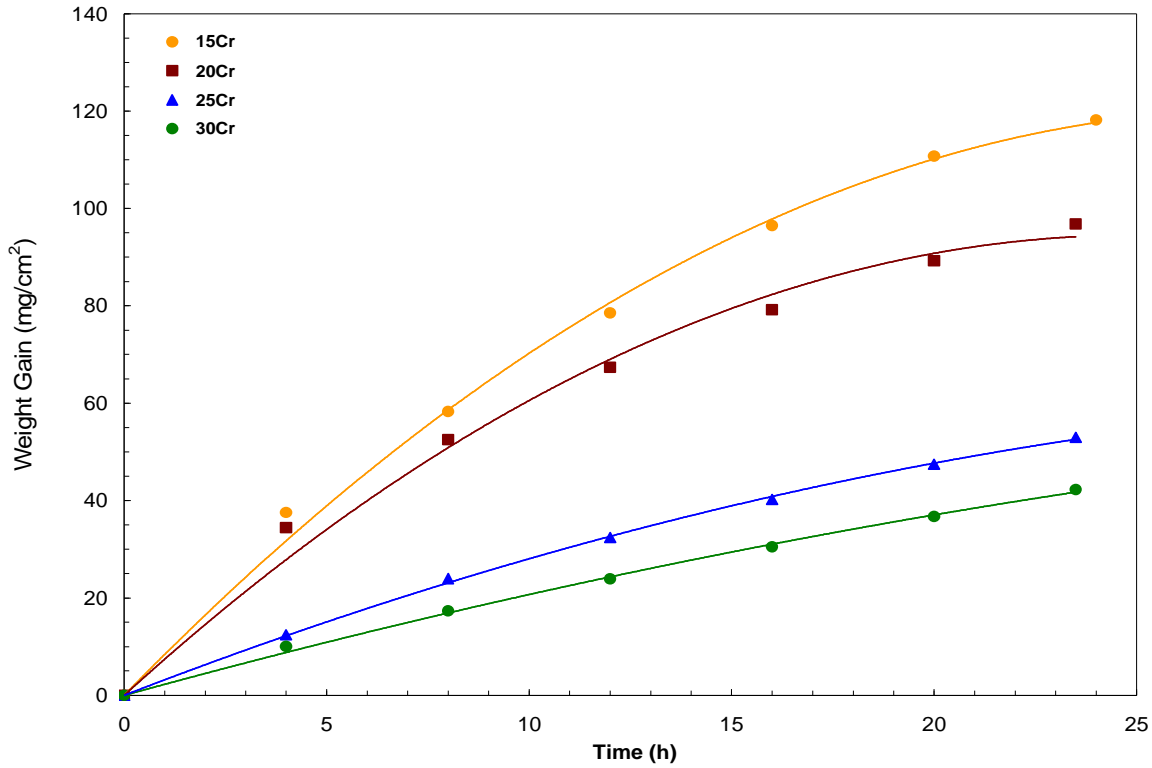


Figure 4.11: Isothermal oxidation curves for 15Cr, 20Cr, 25Cr, and 30Cr alloys at 1300°C.

Figure 4.12 shows the isothermal oxidation curves at 1100°C. The weight gains are slightly lower than the weight gains at 1300°C since the oxidation rate values tend to be lower as temperature decreases. As observed at 1300°C, the oxidation behavior follows a parabolic law and the alloys with higher percentage of Laves phase exhibited

better oxidation resistance at this temperature. The alloy containing 15% of Cr exhibits the lowest resistance with a weight gain that is about 3 times the weight gain of 30Cr alloy.

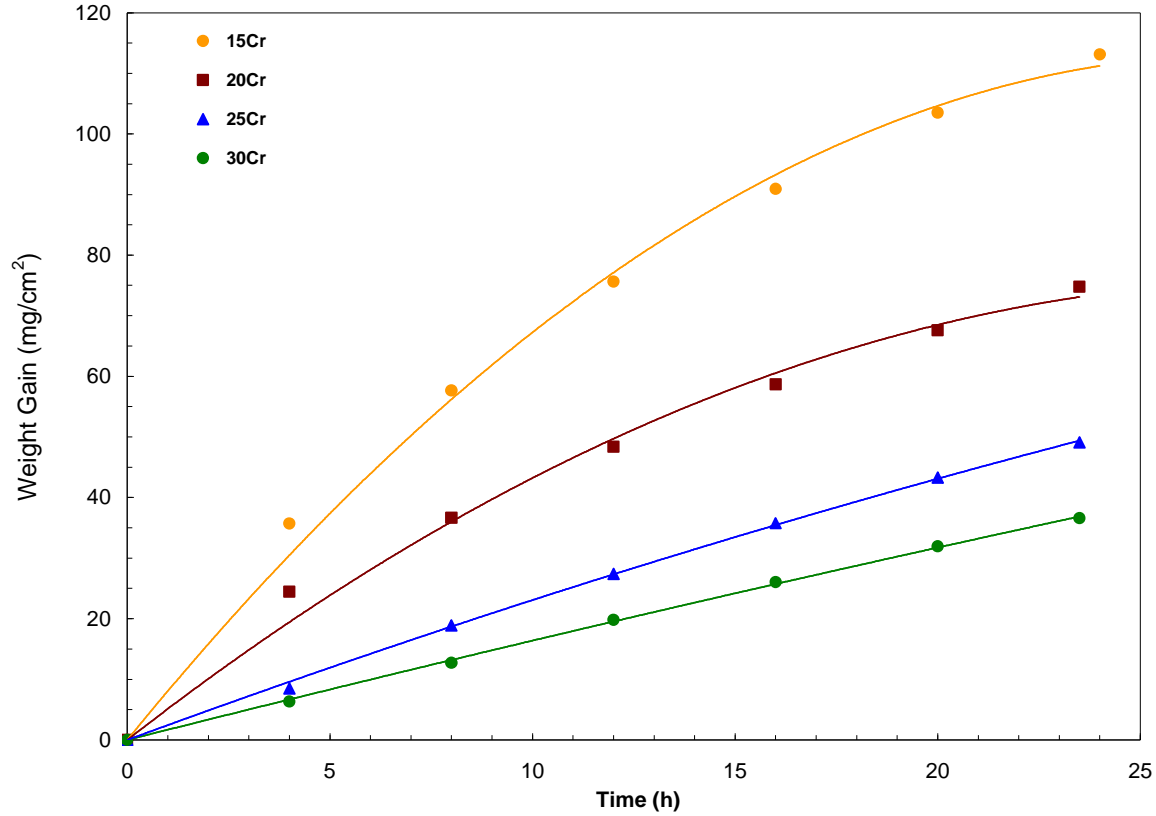


Figure 4.12: Isothermal oxidation curves for 15Cr, 20Cr, 25Cr, and 30Cr alloys at 1100°C.

Contrary to the behavior observed at 1300°C and 1100°C; the samples with higher Cr content showed poor oxidation resistance at 900°C as shown in Figure 4.13. The weight gain per unit area of the 30Cr alloy is approximately two times higher than the weight gained at 1300°C in spite of a temperature difference of 400°C. 15Cr and 20Cr alloys exhibit near identical oxidation behavior at the initial oxidation stage (up to 12 hours), after that point the alloy containing 20% Cr exhibits a slightly better oxidation resistance which may be attributed to the higher Cr content. The high

oxidation rates of 25Cr and 30Cr alloys can be attributed to a porous oxide scale with a limited ability to act as a protective barrier.

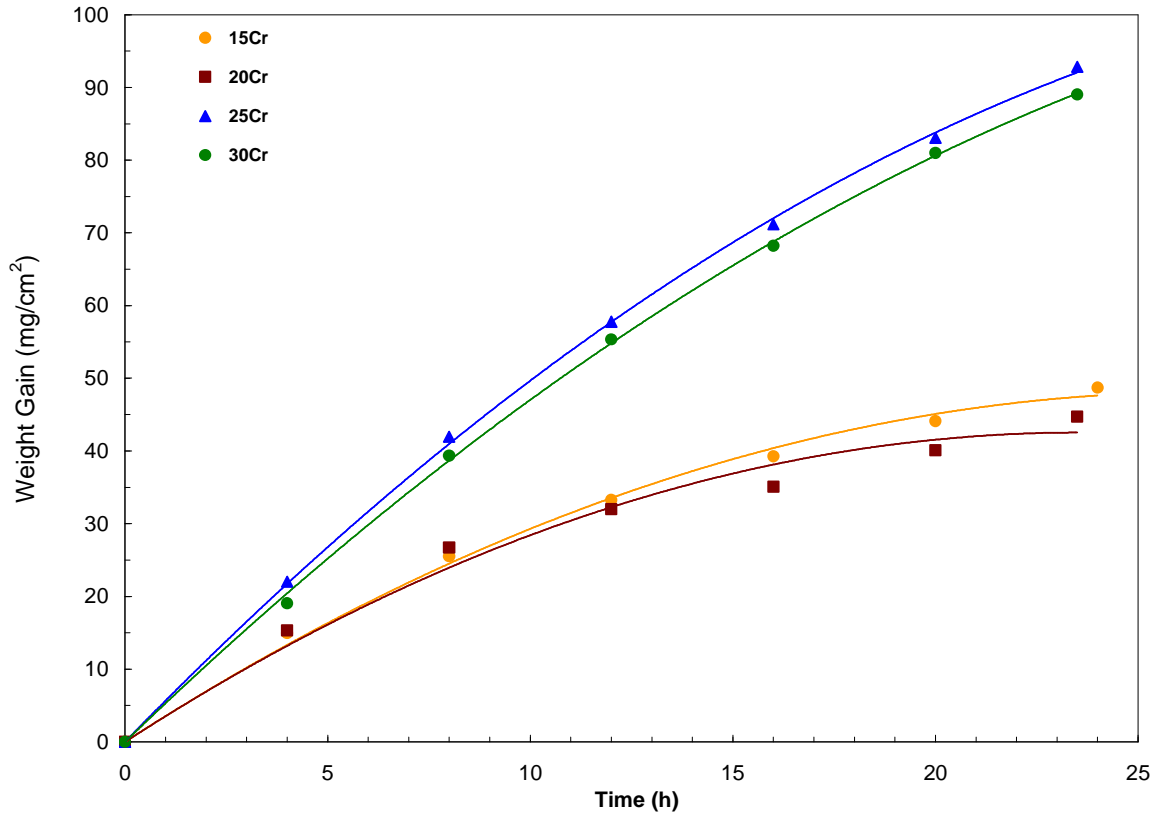


Figure 4.13: Isothermal oxidation curves for 15Cr, 20Cr, 25Cr, and 30Cr alloys at 900°C.

The parabolic rate constants for oxidation tests are listed in Table 4.2. The parabolic oxidation rate constants (k_p) were calculated by least-square, linear-regression analysis of the mass gain per unit surface area ($\Delta m/A$) and the exposure time (t),

$$\left(\frac{\Delta m}{A} \right)^2 = k_p t \quad (4.2)$$

At 900 °C the 25Cr and 30Cr alloys exhibit higher oxidation rates than the alloys containing less Cr, delineating the poor oxidation resistance of the alloys at this

temperature. At 1100°C and 1300°C the oxidation rate values increase with temperature; and decrease as the Cr concentration increases. The parabolic oxidation rate constant is reduced by 88% with the addition of 30% Cr instead of 15% Cr at 1300°C. The relationship between the calculated parabolic rate constants and the Cr content is summarized in Figure 4.14.

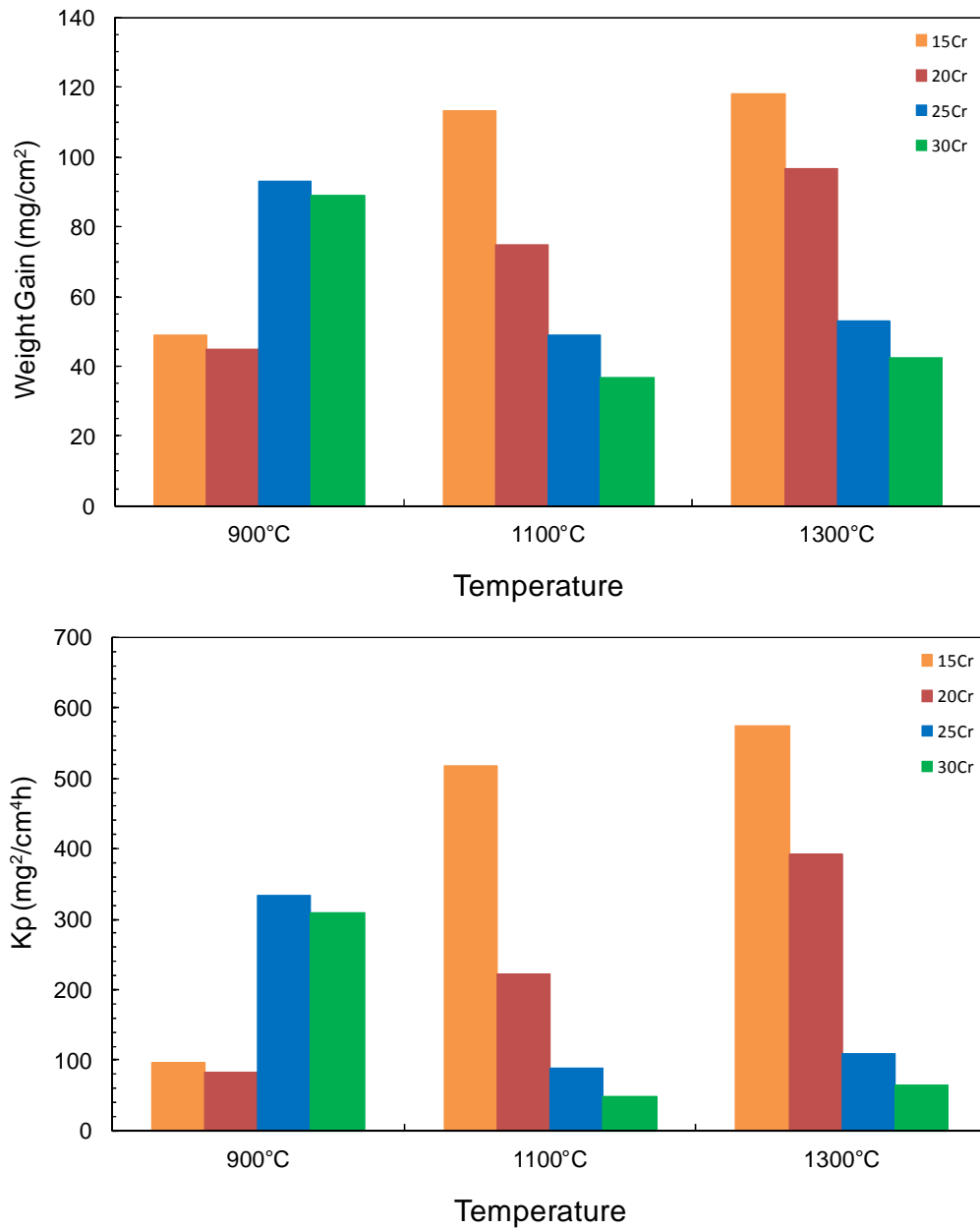


Figure 4.14: Weight gain and parabolic rate constant relationships to Cr content and temperature.

Table 4.2: Values of parabolic rate constants (k_p) corresponding to isothermal exposure.

Temperature	Alloy	Time Span (h)	k_p ($\text{mg}^2 \text{cm}^{-4} \text{h}^{-1}$)
900°C	15Cr	0-24	96.1
	20Cr	0-24	82.2
	25Cr	0-24	333.5
	30Cr	0-24	308.9
1100°C	15Cr	0-24	517.9
	20Cr	0-24	222.8
	25Cr	0-24	88.5
	30Cr	0-24	48.1
1300°C	15Cr	0-24	574.7
	20Cr	0-24	391.9
	25Cr	0-24	108.1
	30Cr	0-24	65.3

A summary of the parabolic oxidation rate constants obtained for the analyzed alloys and Nb alloys being developed for high temperature applications is presented in Table 4.3. Values obtained for the Nb-Cr-W alloys are competitive compared to the values for Nb-based alloys previously reported.

Table 4.3: Parabolic oxidation rate constants for Nb alloys developed for high temperature applications.

Alloy (at%)	T (°C)	K_p ($\text{mg}^2 \text{cm}^{-4} \text{hr}^{-1}$)	Reference
65Nb-39Cr-4W	1300	108.1	This work
60Nb-45Cr-4W	1300	65.3	This work
83Nb-15Si-2B	1000	115	[13]
Nb-24Ti-18Si-5Cr-5Al-2Mo-5Hf	1200	396	[14]
Nb-25Ti	1200 (cyclic)	526.7	[6]
Nb-38Ti-12Hf-12Al	1200 (cyclic)	248.7	[6]
NbCr ₂	1200	10.7	[6]

The characterization of the oxidation behavior of the alloys was based on gravimetric methods, however the metal recession of 25Cr and 30Cr alloys after 16 hours of static oxidation in air at 1300°C was measured in order to compare the

recession values to the short term goal for high temperature alloys which requires a loss of <200 μm in 10 hours at 1370°C [2, 97]. The material loss for 25Cr and 30Cr alloys is of the order of 180 and 160 microns respectively at 1300°C, therefore both alloys are expected to meet the short term goal at 1370°C.

Microhardness measurements were performed on the alloys after oxidation experiments at different temperatures. Figure 4.15 presents the microhardness values of the alloys in the as-cast condition and after 24 hours of exposure at different temperatures. The hardness of the alloys increases as temperature increases, the samples oxidized at 1300°C exhibit the highest hardness values. The change in hardness is more evident for samples with lower Cr content, for instance the hardness of 15Cr increased 90% when oxidized at 1300°C while the hardness of 25Cr and 30Cr alloys only increased between 30 and 35%. The increase in hardness is assumed to be related to the amount of dissolved oxygen in the samples. Hardness values in the range of 900 HV are expected for all the alloys after 24 hours of exposure at 1300°C.

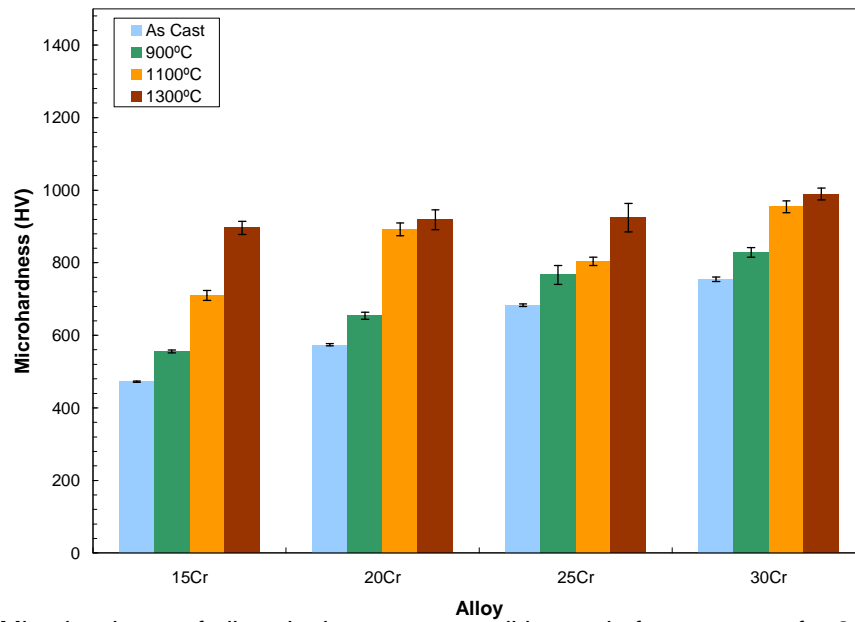


Figure 4.15: Microhardness of alloys in the as-cast condition and after exposure for 24 hours in air at 900, 1100 and 1300°C.

4.3.2 Oxide Scale Characterization

4.3.2.1 Surface Morphology

Figures 4.16 and 4.17 show the appearance of the alloys after isothermal oxidation for 24 hours at different temperatures. The alloys exhibited either a solid scale adhered to the metal surface or powder formation. Samples with solid oxidation products did not exhibit spallation during the oxidation or cooling process, separation of the oxide scale as observed on images was caused by sample handling after the oxidation process.

The alloys with lower Cr content show a compact oxide scale adhered to the metal surface, the thickness of the scale increases with temperature which increases the weight gain as presented in Figures 4.11 to 4.13. The alloys containing 25 and 30% Cr suffered from scale spallation and powder formation at 900°C which is consistent with the high weight gains and oxidation rate constants of the samples. The scale formed at 1100°C consisted of oxide layers that spall off and turn to powder easily. High Cr content alloys exhibited the best oxidation resistance at 1300°C, with small weight gains, a thin oxide layer and no spallation.

Figures 4.18 to 4.21 show BSE images of the surface morphologies of the alloys after oxidation at 900, 1100, and 1300°C for 24 hours. The characteristics of the scale formed on the surface change with Cr content and temperature. The samples with the best oxidation resistance at 900°C (15Cr and 20Cr) exhibit smoother surfaces. The surface on 25Cr and 30Cr alloys is rough and prone to spallation, which is in agreement with the poor oxidation resistance observed.

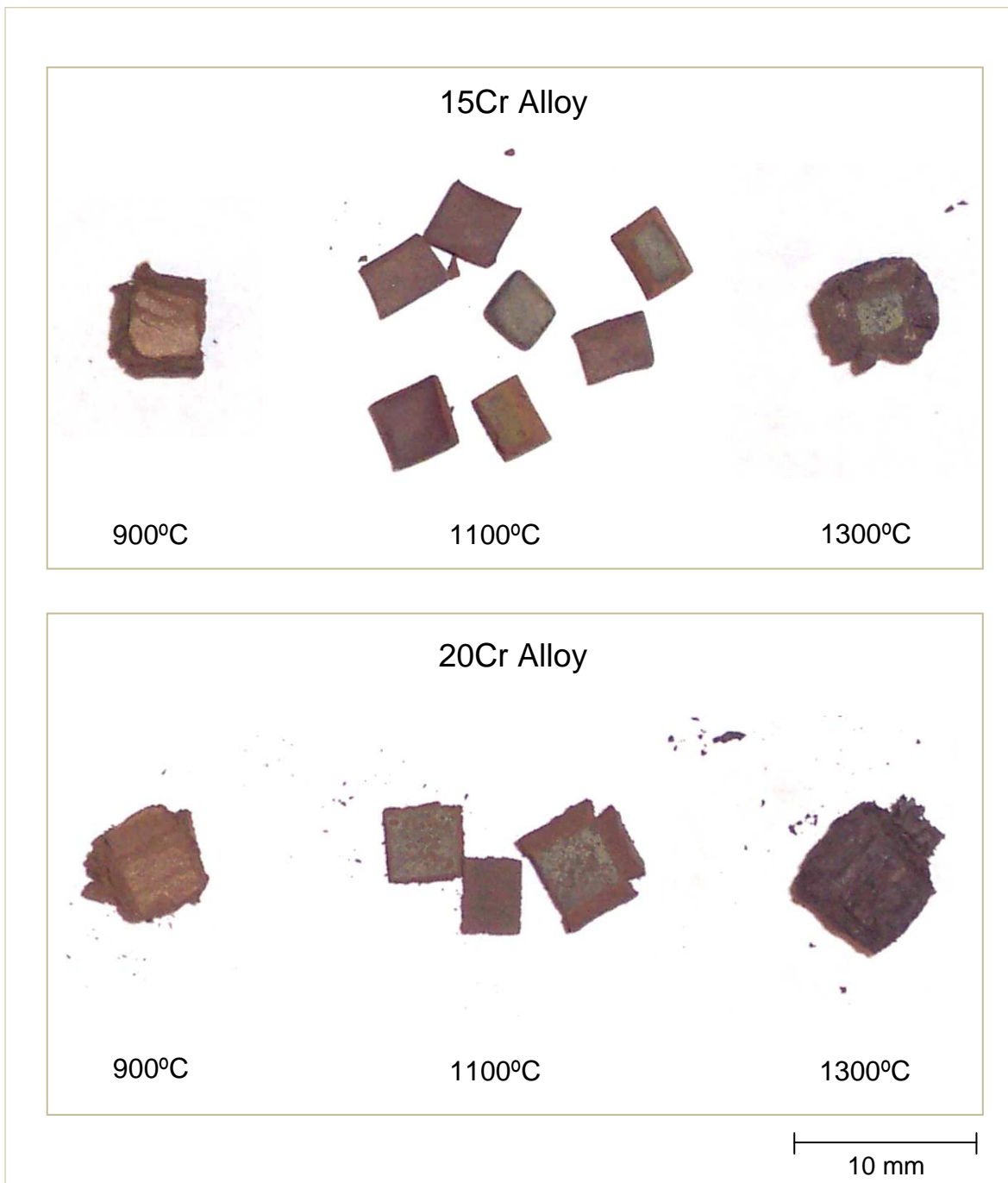


Figure 4.16: Oxidation products obtained from 15Cr and 20Cr alloys after isothermal oxidation for 24 hours.

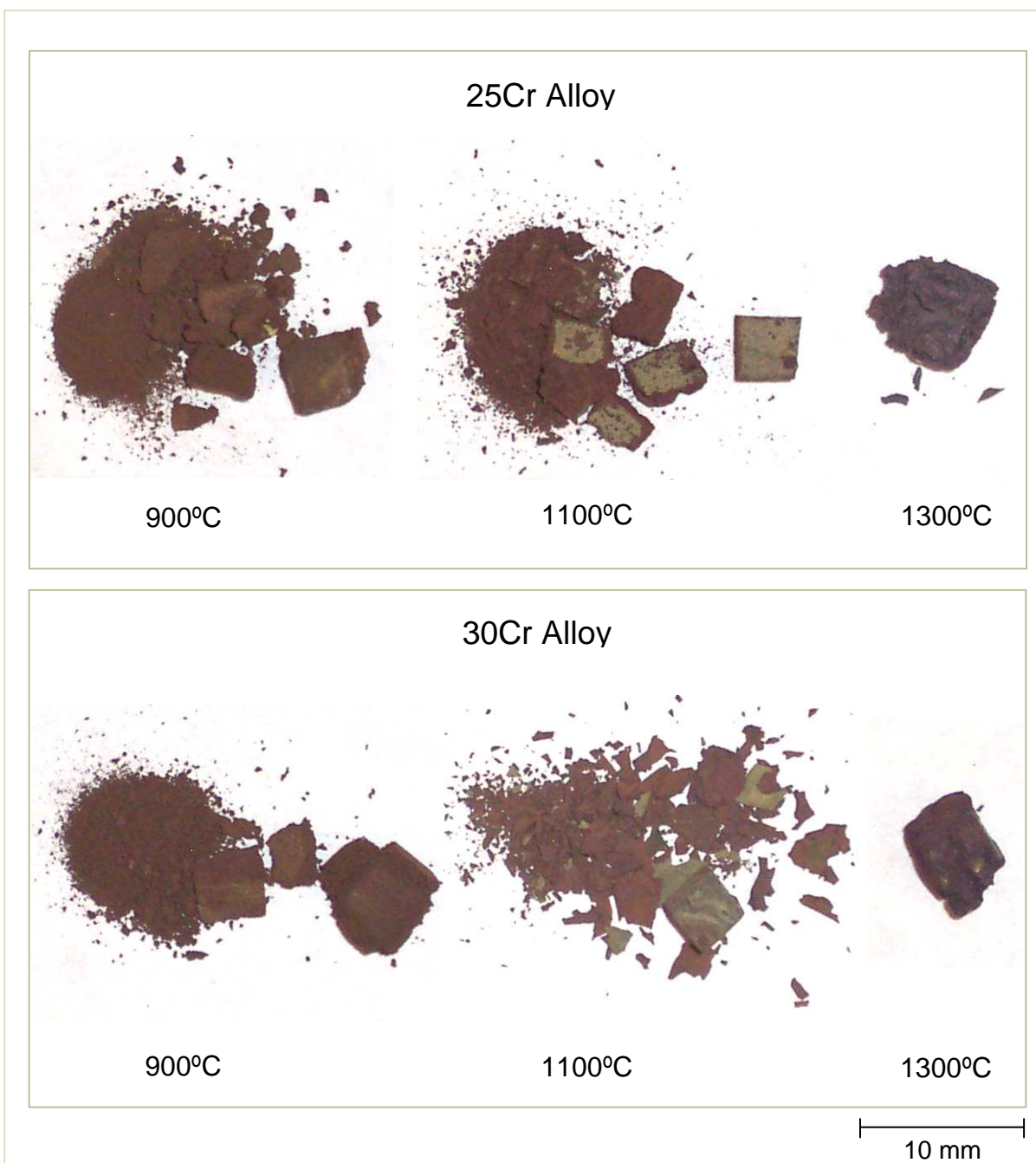


Figure 4.17: Oxidation products obtained from 25Cr and 30Cr alloys after isothermal oxidation for 24 hours.

Surfaces become smoother as temperature increases. Fine granular oxide structures are observed at 1100 and 1300°C. Particle coarsening occurs as the oxidation temperature increases; the particles formed at 1300°C are significantly larger than the particles formed at 1100°C. Particle distribution is more uniform in 15Cr and 20Cr oxide scales than in the alloys with higher Cr percentages.

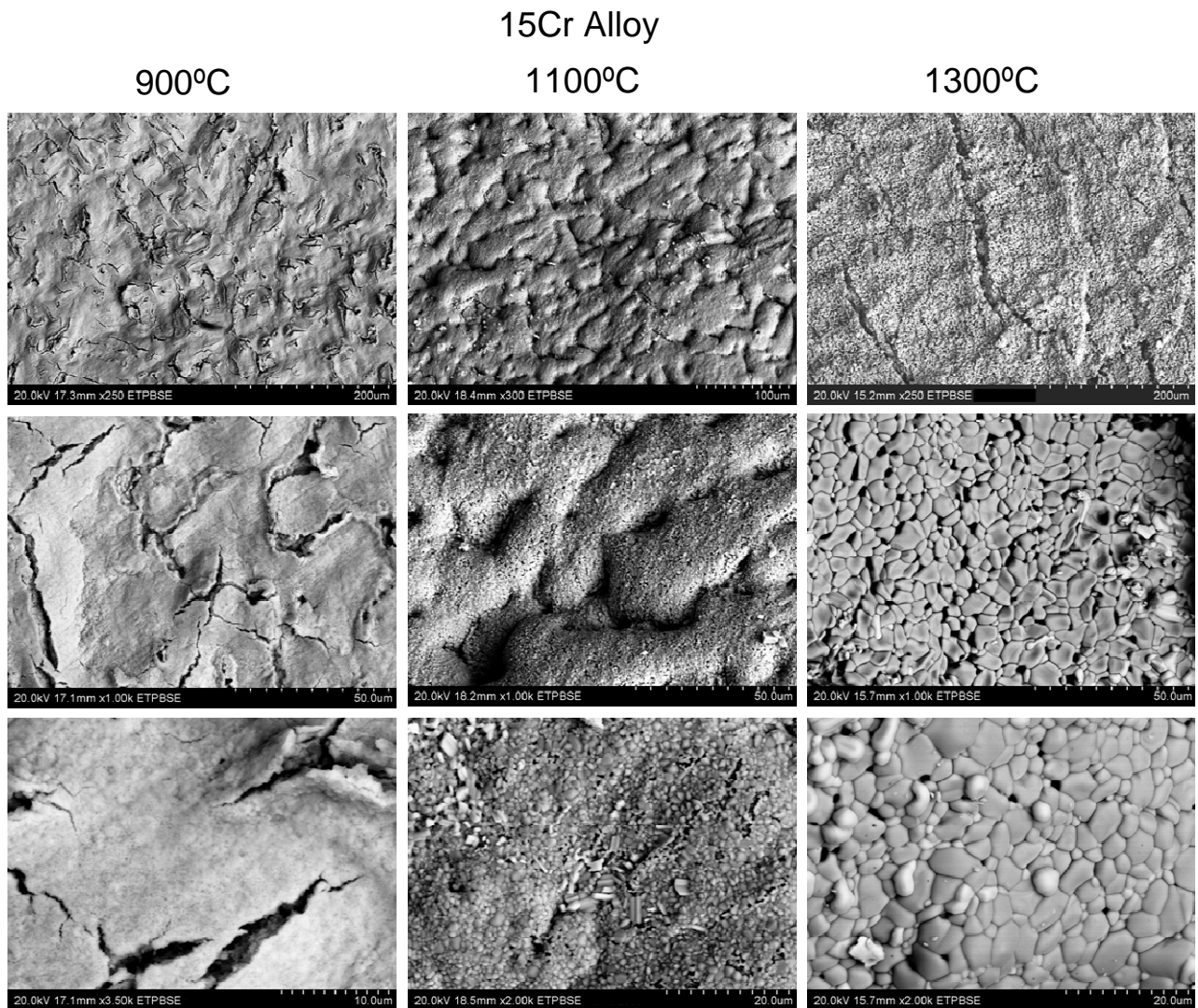


Figure 4.18: BSE images of the oxide surface of 15Cr alloy oxidized for 24 hours at 900, 1100, and 1300°C.

The EDS elemental analysis and BSE contrast were used to estimate the composition of the oxidation products. The oxide surface of 15Cr alloy exhibits low Cr concentration at 900°C; the atomic percentages of Nb and O suggest that Nb₂O₅ is the main constituent at this temperature. According to EDS analysis, the darker areas observed on the surface of 20Cr alloy especially at 1100°C (Figure 4.19) are Cr rich.

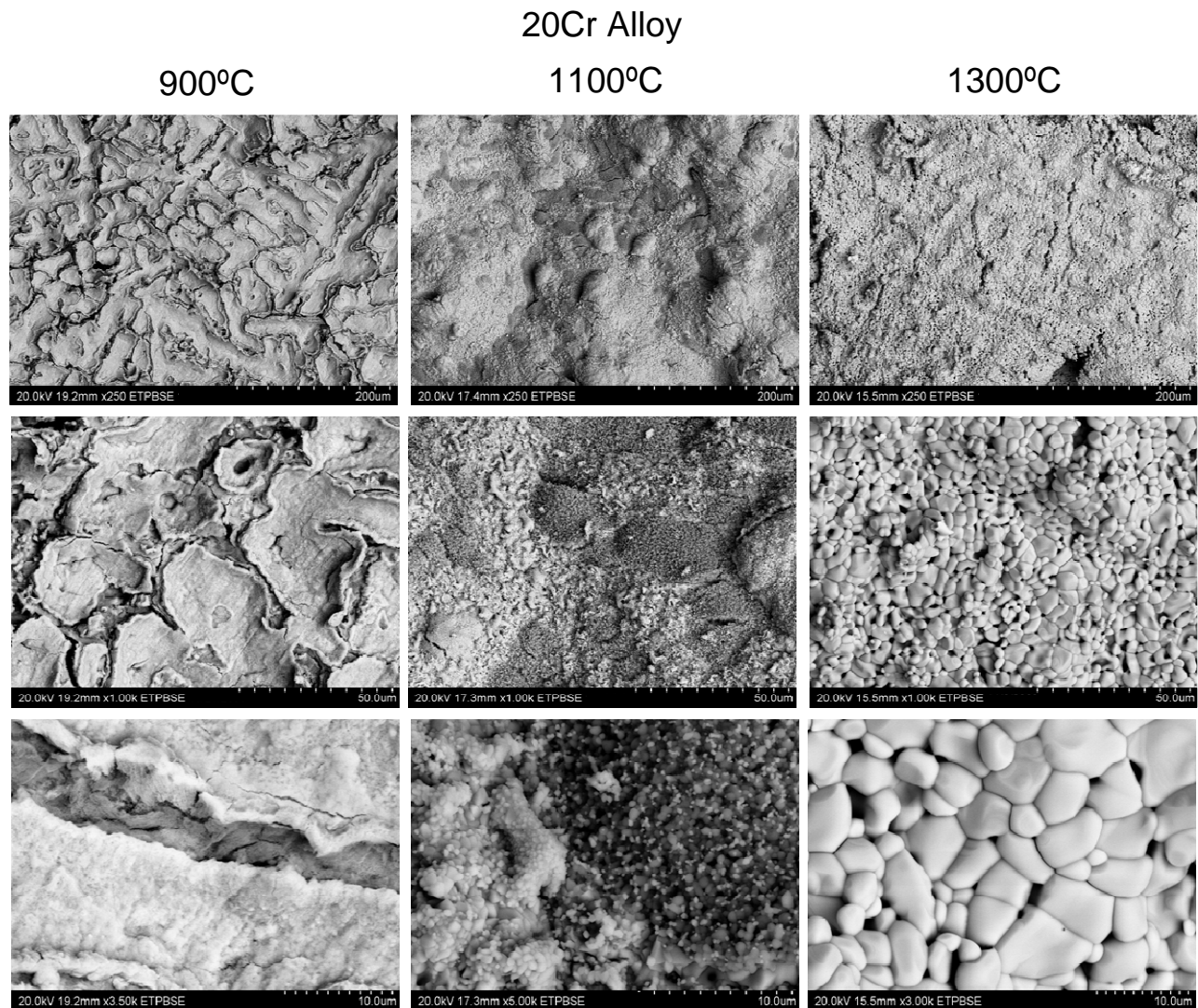


Figure 4.19: BSE images of the oxide surface of 20Cr alloy oxidized for 24 hours at 900, 1100, and 1300°C.

The Cr concentration on the oxide surface is higher for the alloys with higher Cr concentration in the base material. Nb rich areas tend to contain slightly higher tungsten concentrations.

The morphology and composition of oxide surfaces from 25Cr and 30Cr are similar. The BSE contrast reveals a combination of light and darker areas (Figures 4.20 and 4.21). According to Nb:Cr ratio, the darker areas are presumed to be CrNbO_4 and the lighter particles Nb_2O_5 .

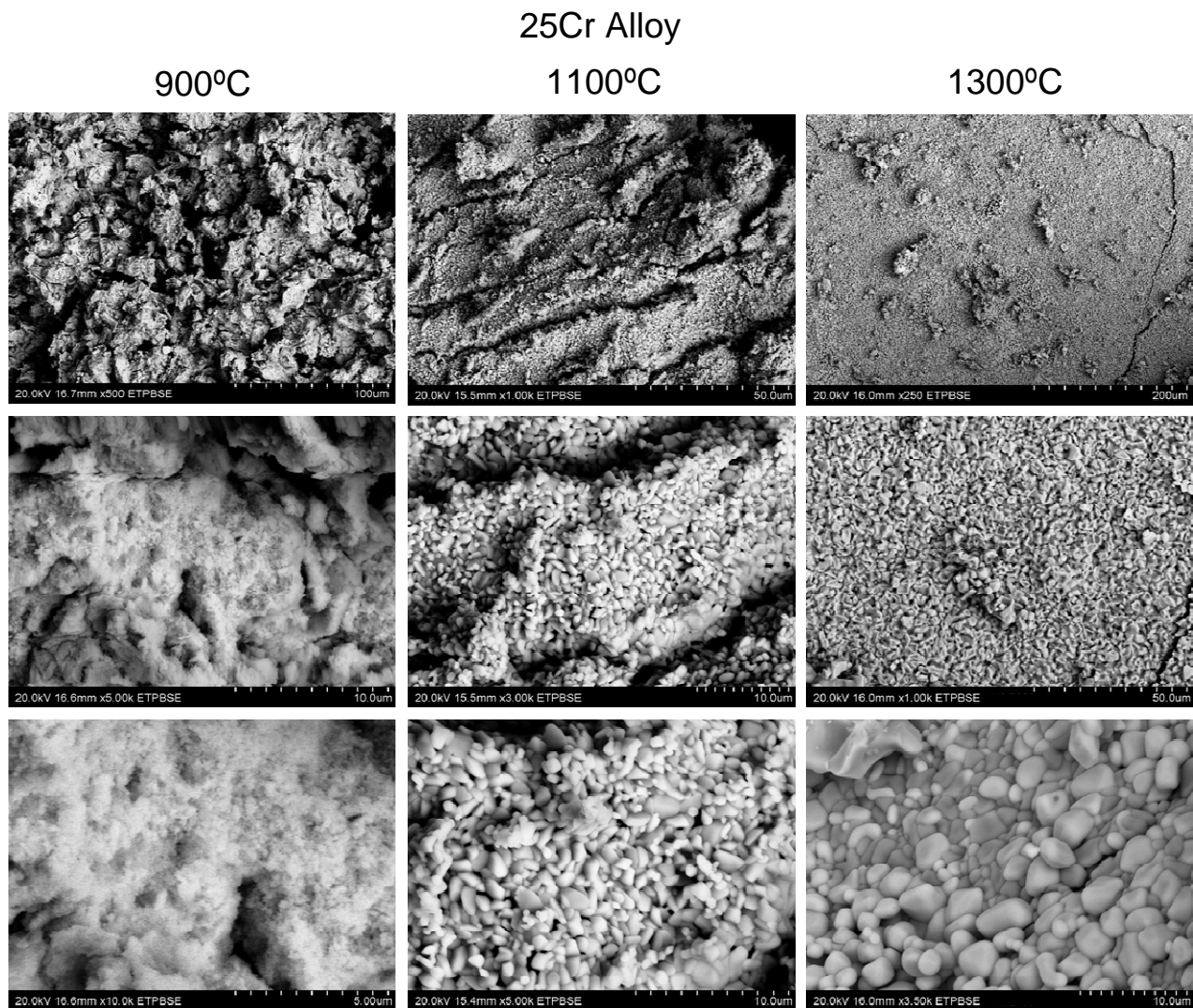


Figure 4.20: BSE images of the oxide surface of 25Cr alloy oxidized for 24 hours at 900, 1100, and 1300°C.

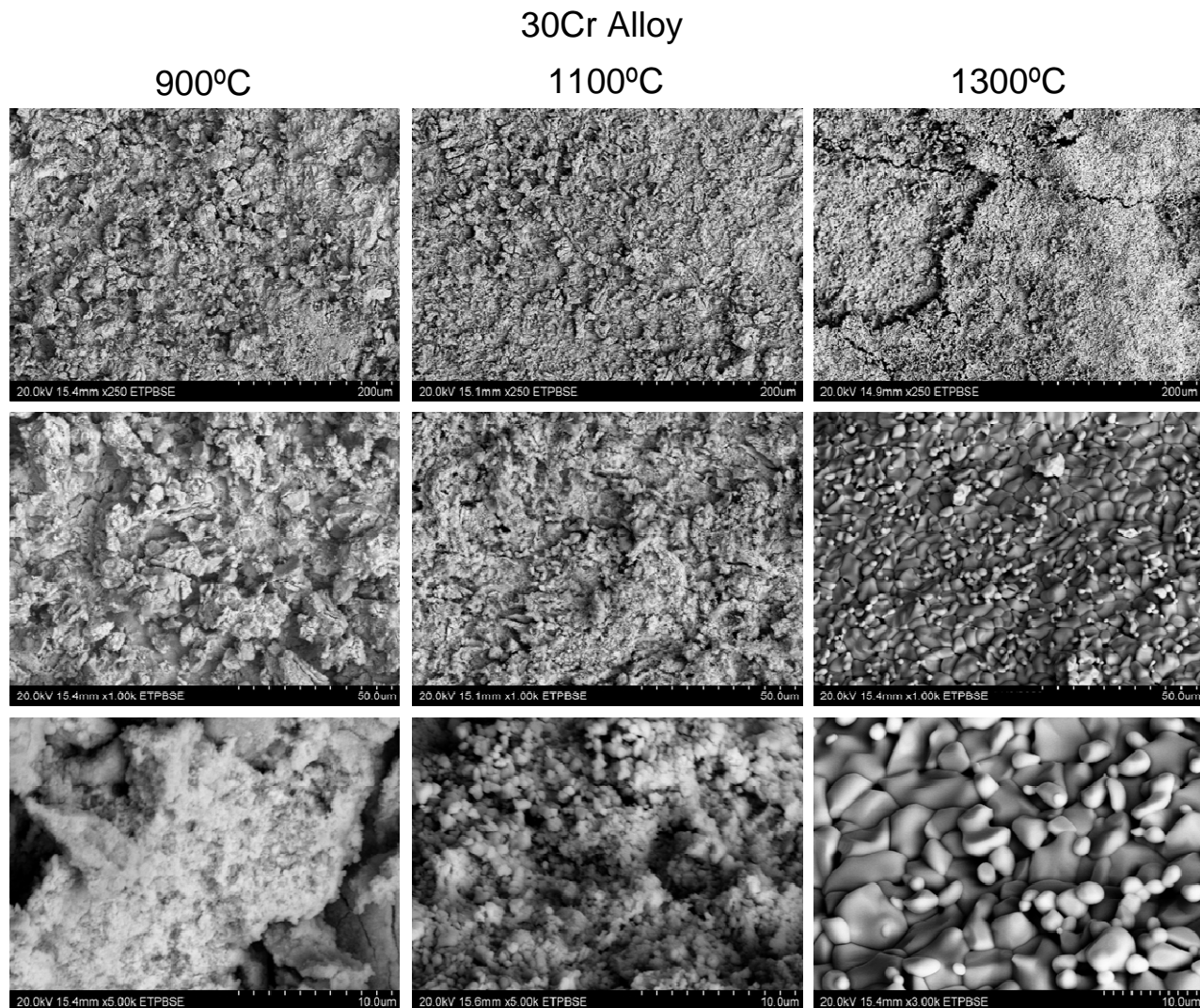


Figure 4.21: BSE images of the oxide surface of 30Cr alloy oxidized for 24 hours at 900, 1100, and 1300°C.

4.3.2.2 Oxidation Products Analysis by X-ray Diffraction

The oxidation products of the different alloys were identified by XRD. Figures 4.22 to 4.24 present the XRD patterns obtained from the oxidation products of the alloys after 24 hours of exposure at 900, 1100, and 1300°C respectively. The products are mainly a mixture of CrNbO_4 , and Nb_2O_5 . Two modifications of Nb_2O_5 were identified, one corresponding to the M-form (monoclinic with lattice parameters $a=$

22.10Å, $b=7.64\text{\AA}$, $c=19.52\text{\AA}$, $\beta=118.30^\circ$) present at 900°C, and the high temperature H-form (monoclinic with lattice parameters $a=20.38\text{\AA}$, $b=3.82\text{\AA}$, $c=19.36\text{\AA}$, $\beta=115.69^\circ$) observed at 1100°C and 1300°C. The M-form is often regarded as a less ordered precursor of the high temperature H-form [84].

While the types of oxides formed are similar, the relative amounts differ according to Cr content and temperature. As the Cr concentration increases the intensity of the Nb_2O_5 peaks decreases, thus CrNbO_4 is the predominant oxide formed on 30Cr sample by virtue of the relative peak heights of this oxide compared to Nb_2O_5 . Oxidation products observed are consistent with those reported for Nb and NbCr_2 alloys in the literature [6, 12, 23-26].

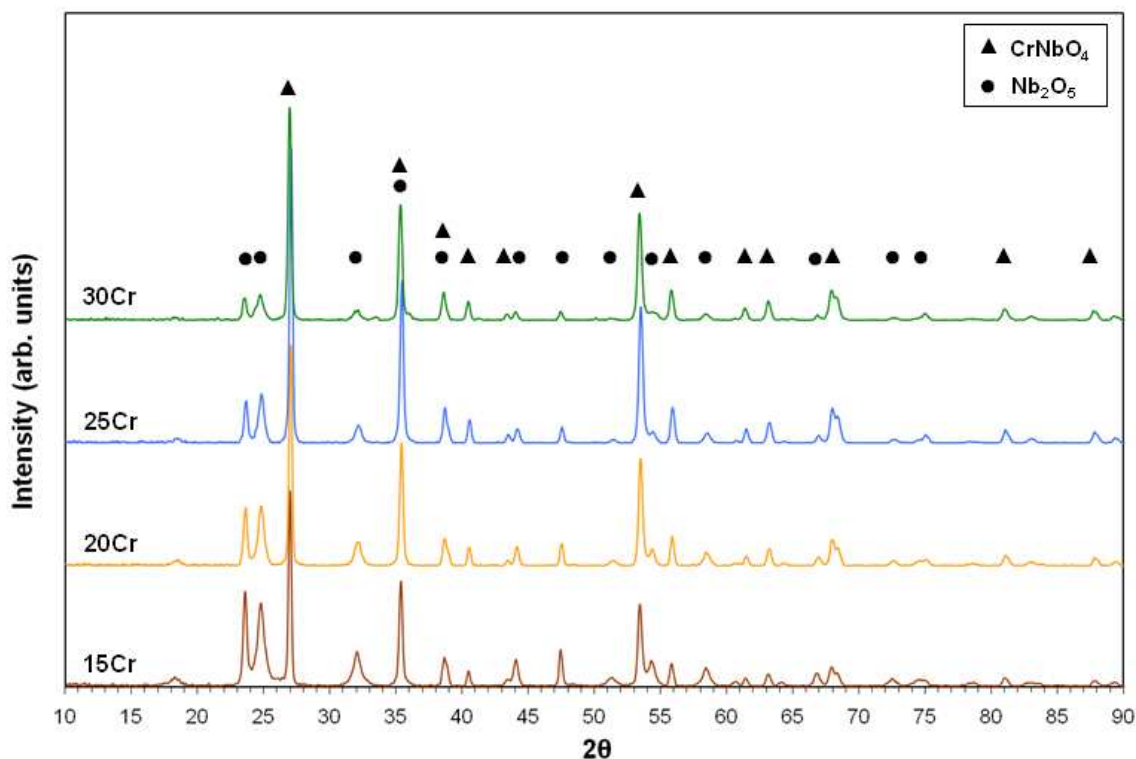


Figure 4.22: XRD pattern of the oxidation products obtained from the 4 alloys after 24 hours of exposure at 900°C.

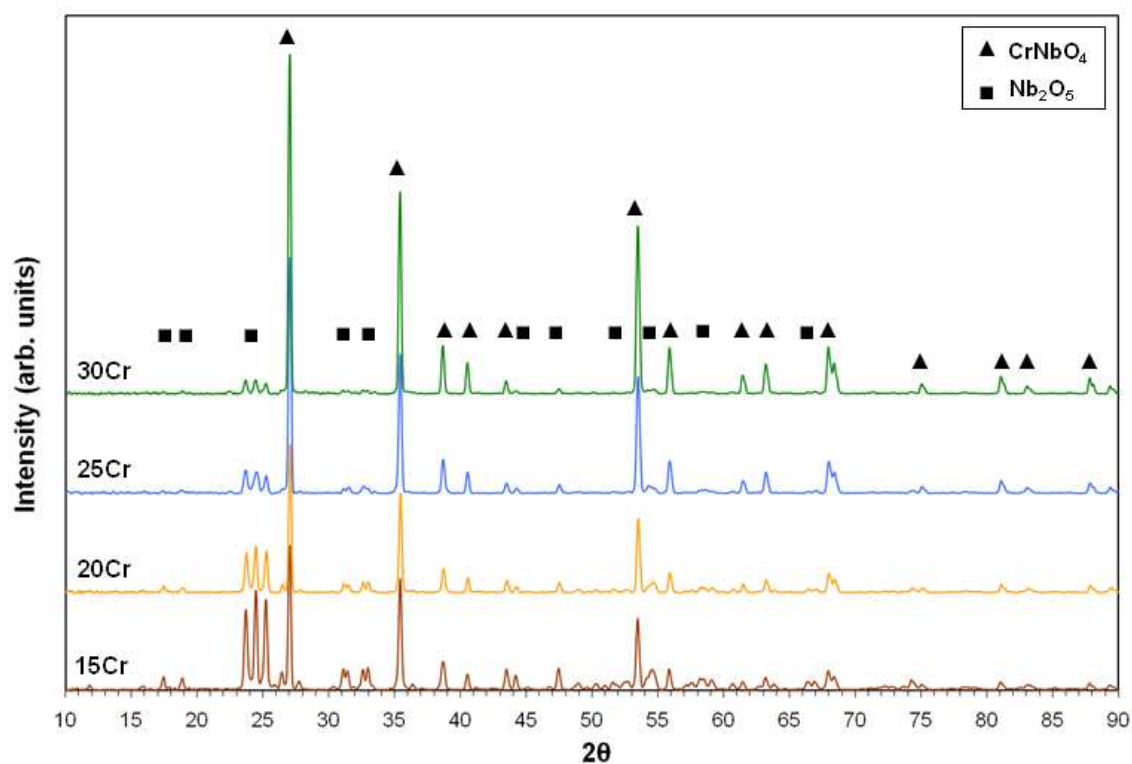


Figure 4.23: XRD pattern of the oxidation products obtained from the 4 alloys after 24 hours of exposure at 1100°C.

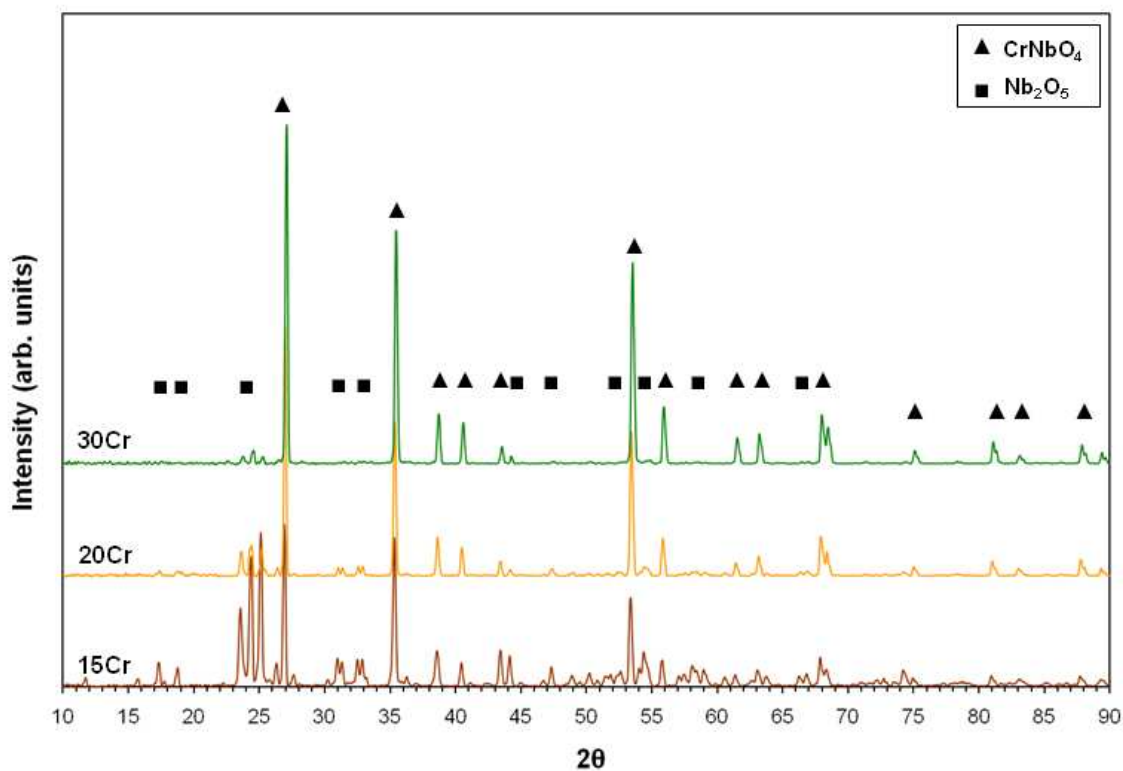


Figure 4.24: XRD pattern of the oxidation products obtained from 15Cr, 20Cr, and 30Cr alloys after 24 hours of exposure at 1300°C.

The reflection with the highest intensity occurs at $2\theta=27.1$ deg in the case of CrNbO_4 while for $\text{M-Nb}_2\text{O}_5$ and $\text{H-Nb}_2\text{O}_5$ the most intense reflections occur at $2\theta=23.7$ and $2\theta=24.4$ deg respectively. The intensity ratio of the CrNbO_4 reflection to the Nb_2O_5 reflection ($I_{\text{CrNbO}_4}/I_{\text{Nb}_2\text{O}_5}$) was used to perform a comparison of the relative amounts of CrNbO_4 and Nb_2O_5 in the oxidation product. The results are plotted as a function of the intermetallic phase volume percentage in Figure 4.25. The relative intensity ratio increases with the volume percent of intermetallic phase, therefore it is reasonable to believe that the formation of CrNbO_4 is favored in alloys with higher volume percent of Laves phase. The graph also shows the effect of temperature, the relative intensity ratio increases significantly in the case of alloys with higher intermetallic phase content, while the range of variation is small in the case of alloys with lower values of intermetallic phase volume percentage (15Cr and 20Cr).

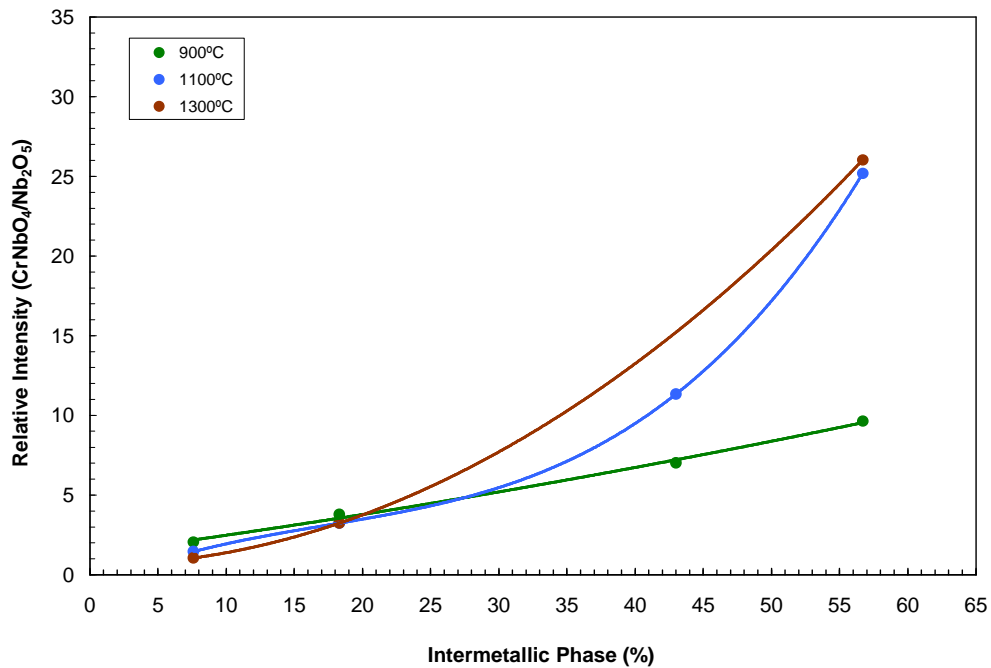


Figure 4.25: Relative intensity ratio as a function of the volume percentage of intermetallic phase.

4.3.2.3 SEM and EDS Analysis of Oxide-Metal Interfaces

The oxide-metal interface images of sample 15Cr oxidized at 900°C for 24 hours are presented in Figure 4.26. Results from the XRD analysis, the EDS analysis and the BSE contrast were used to identify the oxidation products. The oxide scale is a combination of Nb_2O_5 (light gray areas) and CrNbO_4 (dark gray areas) alternated oxide layers. The oxide layers contain fissures parallel to the metal surface which are more evident at the CrNbO_4 rich areas. These types of irregularities are usually caused by the stress generated by the difference in the oxide volumes and the thermal expansion coefficients. The first oxide layer has a lighter appearance than the successive layers (Figure 4.26a), EDS elemental analysis revealed a Nb/O ratio close to 1, which leads to believe that this first layer is the intermediate reaction product NbO. The presence of the NbO at the metal-oxide interface depends on time, temperature and pressure of oxidation, and also on the local radius of curvature of the metal oxide interface [102, 57]. The oxidation of Nb-Cr alloys resulting in alternate layers of Nb_2O_5 and CrNbO_4 has been previously reported [103]; these studies indicate that oxide growing occurs by inward oxygen diffusion. The BSE image and X-ray maps in Figure 4.27 show the Nb, Cr, W, and O distribution for 15Cr alloy at 900°C. The Cr rich alternate layers corresponding to the CrNbO_4 oxide are clearly distinguished.

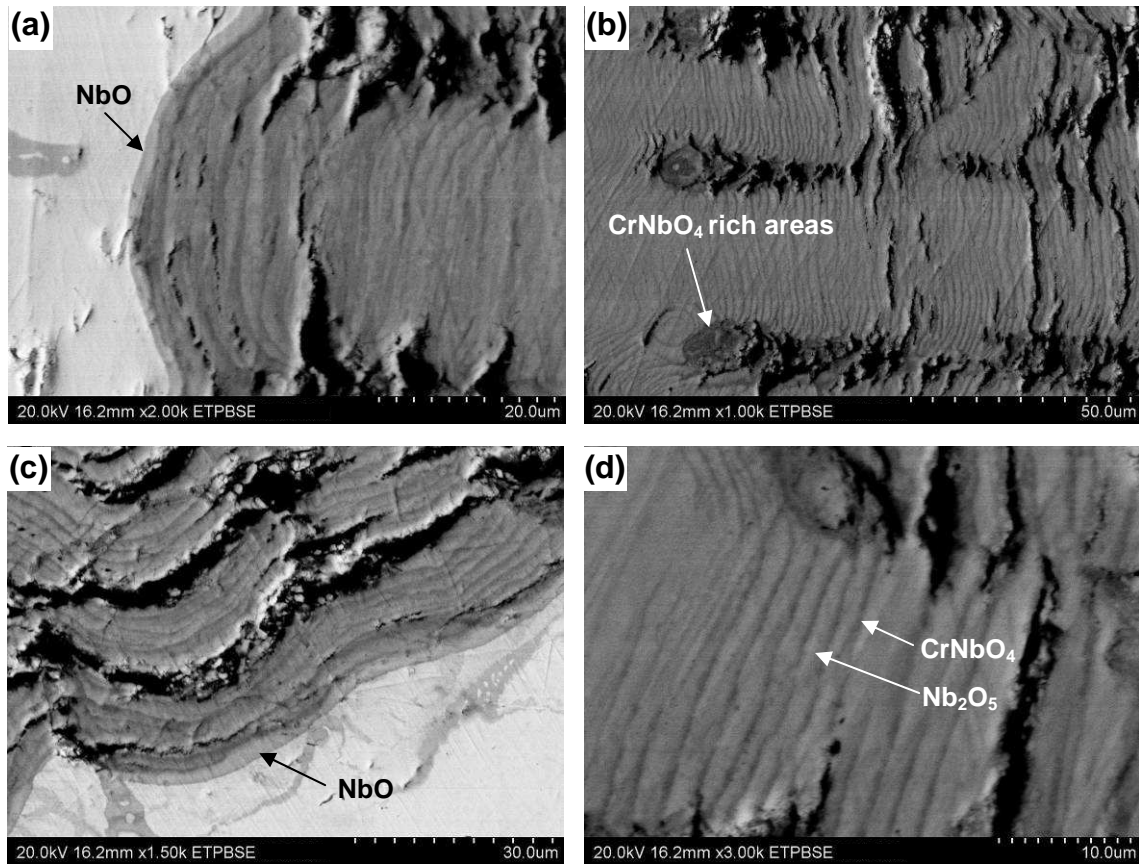


Figure 4.26: BSE images of the metal-oxide interface of 15Cr alloy after 24 hours of exposure at 900°C. (a) and (c) interface, (b) and (d) oxide scale.

Figure 4.28 presents the metal oxide interface of 20Cr alloy oxidized at 900°C for 24 hours. The oxide scale consists of alternate layers of CrNbO₄ and Nb₂O₅ and dark gray areas of CrNbO₄. A layer of NbO was not observed in this case. The oxide scale exhibits more fissures and layer separation than the oxide scale of 15Cr alloy especially at the metal oxide interface. The formation of these discontinuities is again related to the stress generated by the two types of oxides formed and it is more severe in this case since more CrNbO₄ areas are present. The distribution of the Cr rich areas (dark gray areas) in Figure 4.29 suggests that they are a product of the oxidation of the intermetallic phase into CrNbO₄. The oxidation of the Nb_{ss} and the

NbCr₂ phases is presented in Figure 4.30 which is an image of the metal interface of 30Cr alloy oxidized at 900°C showing that the Nb_{ss} and the NbCr₂ phases can oxidize independently to form Nb₂O₅ and CrNbO₄ respectively.

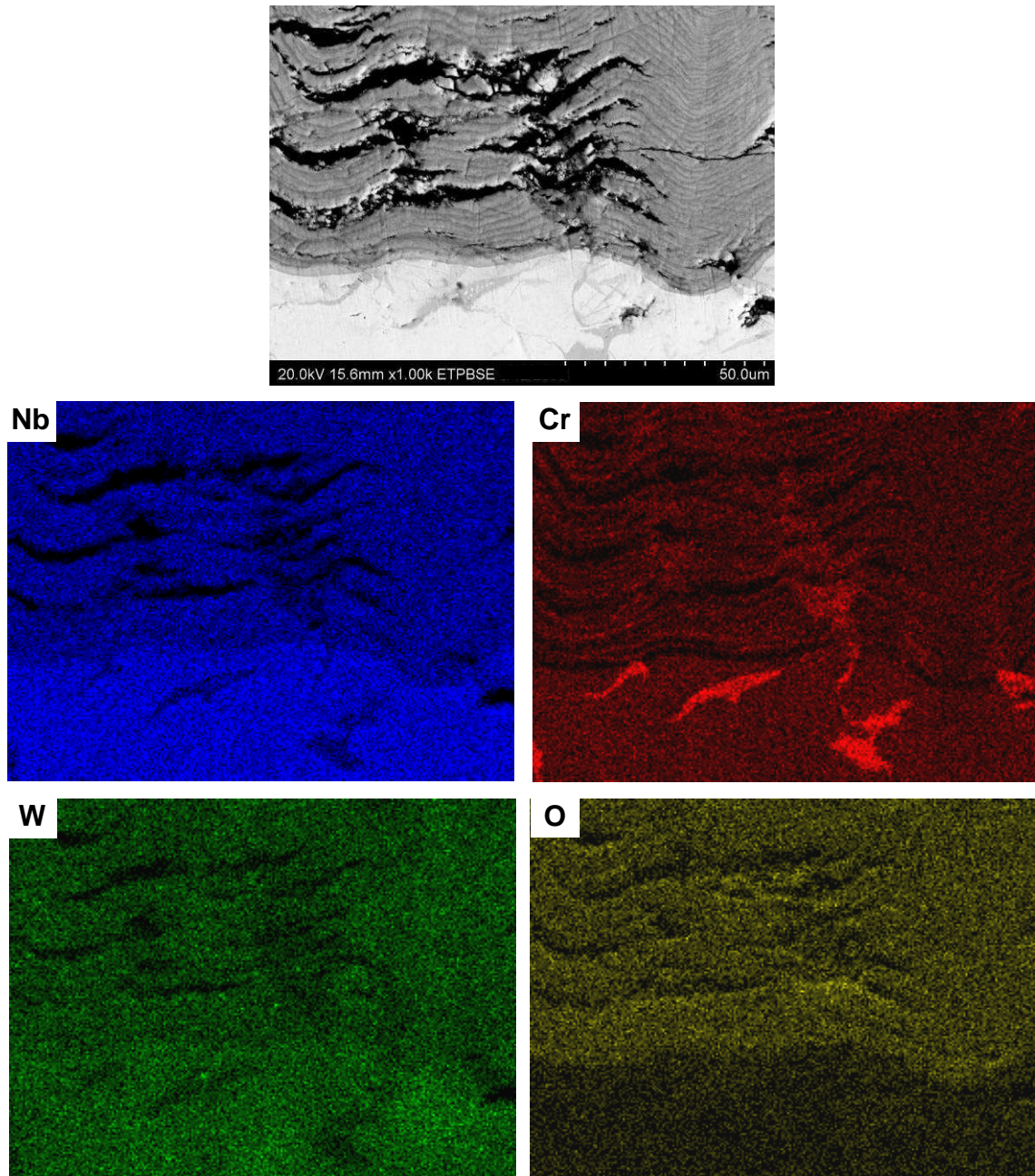


Figure 4.27: BSE image and X-ray maps showing Nb, Cr, W, and O distribution for 15Cr alloy oxidized 24 hours at 900°C.

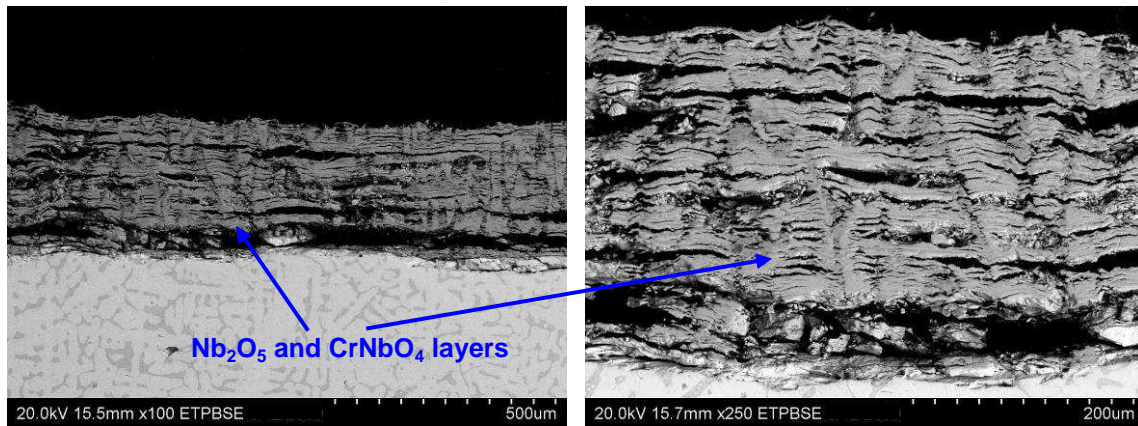


Figure 4.28: BSE images of the metal-oxide interface of 20Cr alloy after 24 hours of exposure at 900°C.

The oxide-metal interfaces of 25Cr and 30Cr alloys (Figures 4.31 and 4.32) present numerous microcracks around the perimeter of the sample which causes alloy fragmentation before the complete oxidation of the phases. These microcracks cause the accelerated oxidation and powder formation observed for these alloys. The poor oxidation resistance of Nb-based alloys at intermediate temperatures caused by internal oxidation and microcrack formation has been previously reported by Bewlay *et al.* [2], Chan [12], Geng *et al.* [14, 92], and Moricca *et al.* [45]. Figure 4.31 shows that complete oxidation of the alloy occurs after fragmentation. Oxide scales in Figures 4.31c and 4.32b show the final products of oxidation, Nb_2O_5 and CrNbO_4 layers and CrNbO_4 areas.

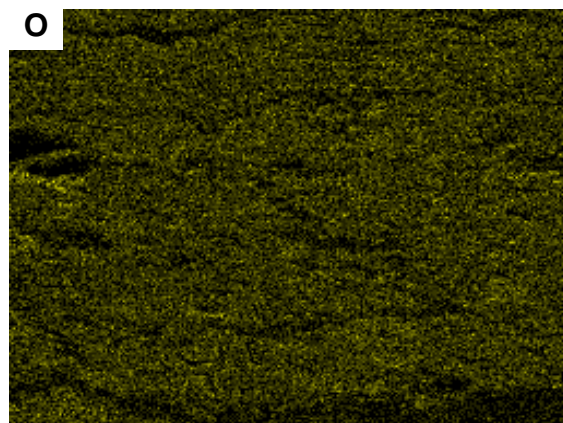
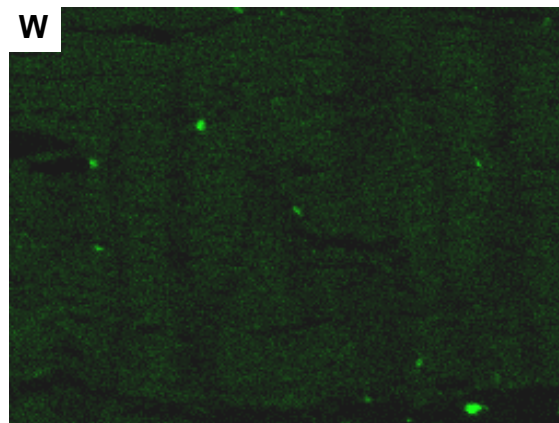
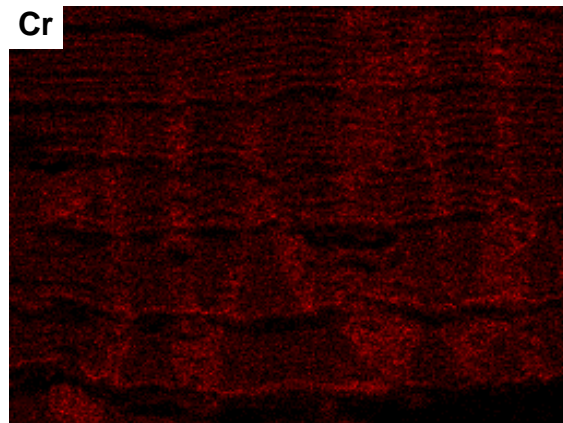
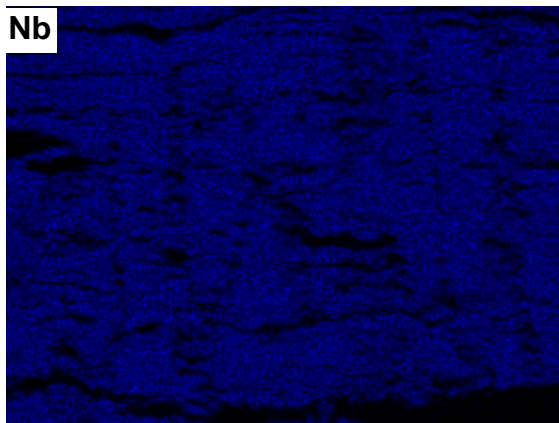
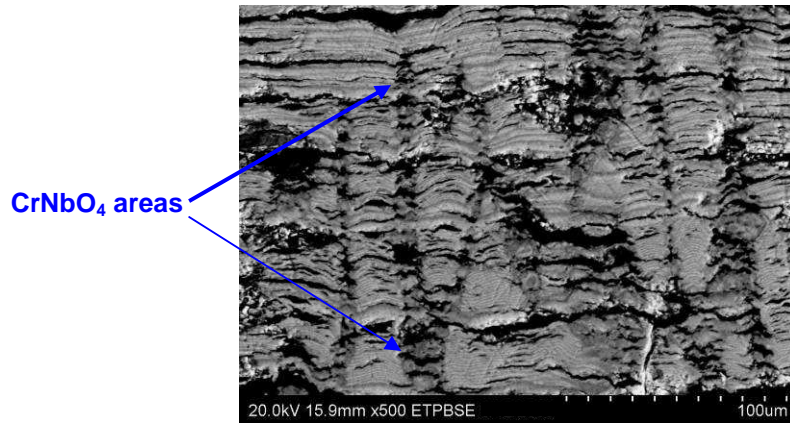


Figure 4.29: BSE image and X-ray maps showing Nb, Cr, W, and O distribution for 20Cr alloy oxidized 24 hours at 900°C.

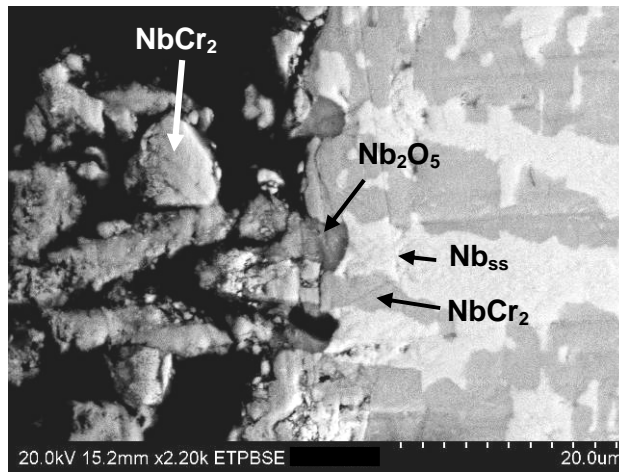


Figure 4.30: BSE images of the metal-oxide interface of 30Cr alloy after 24 hours of exposure at 900°C showing oxidation of Nb_{ss} and NbCr₂ to form Nb₂O₅ and CrNbO₄ respectively.

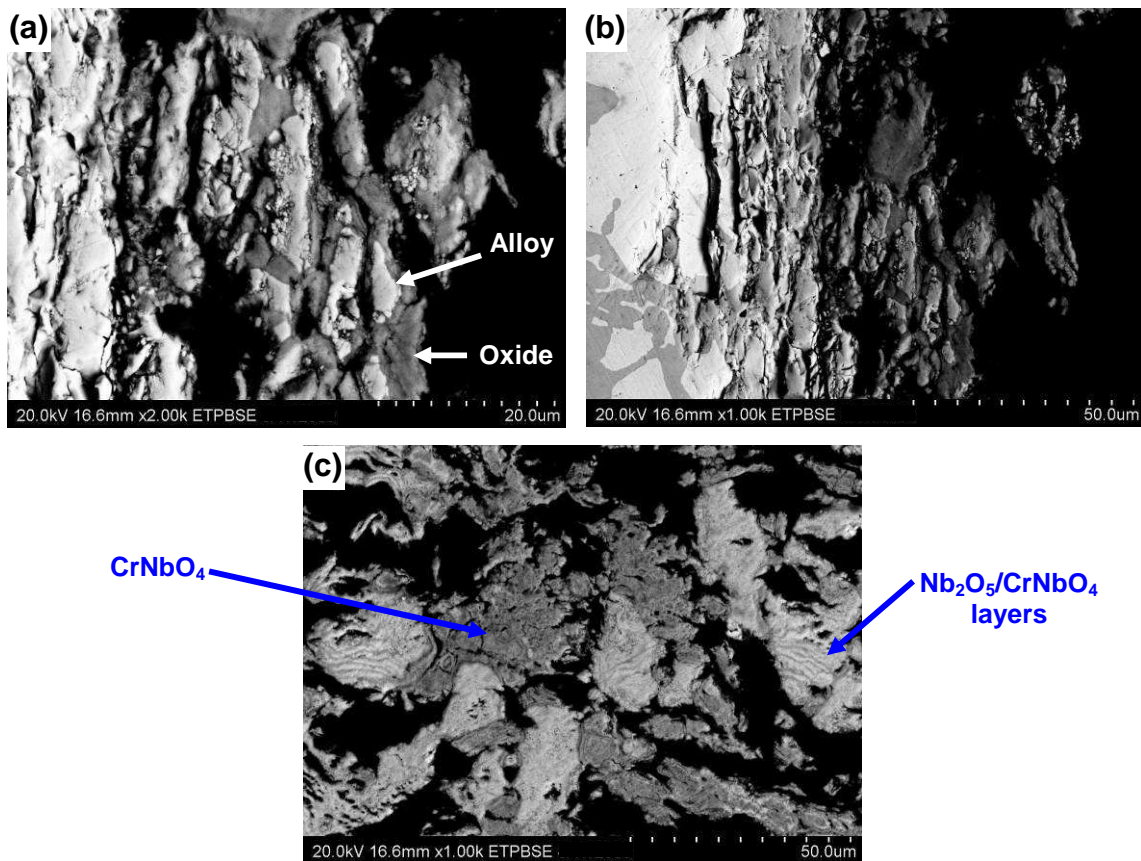


Figure 4.31: BSE images of the metal-oxide interface of 25Cr alloy after 24 hours of exposure at 900°C. (a) and (b) interface, (c) oxide scale.

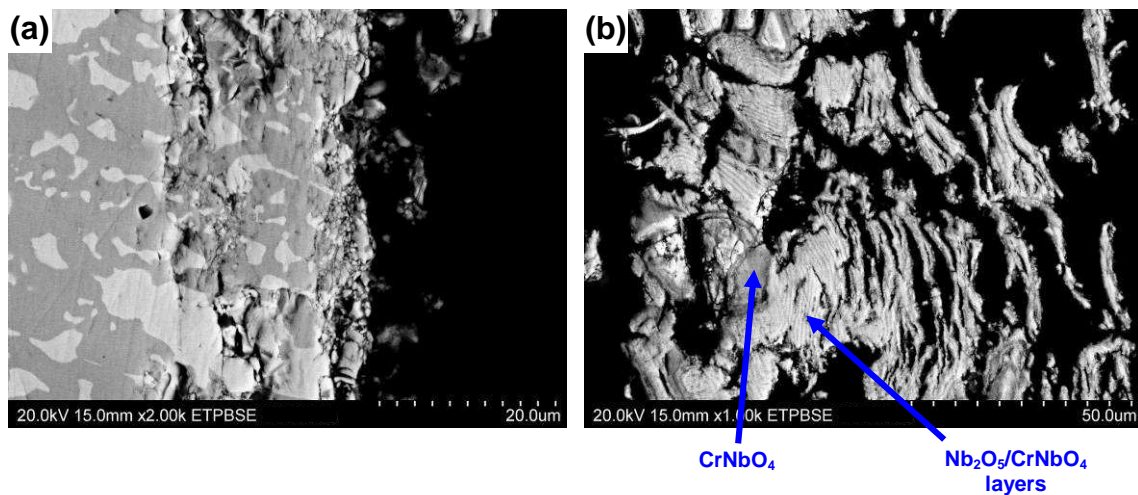


Figure 4.32: BSE images of the metal-oxide interface (a) and oxide scale (b) of 30Cr alloy after 24 hours of exposure at 900°C.

The oxide-metal interface images of sample 15Cr oxidized at 1100°C for 24 hours are presented in Figure 4.33. The oxide scale contains some porosity; neither oxide layers nor fissures are observed. The oxidation products are a mixture of Nb₂O₅ (light gray areas), CrNbO₄ (dark gray areas) and irregular porosity. Some spallation of the oxide scale is observed, mainly at areas that are rich in CrNbO₄ which are considered high stress areas. The scale is prone to spallation as shown in Figure 4.33a. The BSE image and X-ray maps in Figure 4.34 show the Nb, Cr, W, and O distribution for 15Cr alloy at 1100°C. The element distribution is mainly uniform through the oxide layer, slight Cr depletion is observed close to the metal interface which is apparently caused by differences in the Nb₂O₅/ CrNbO₄ oxide distribution.

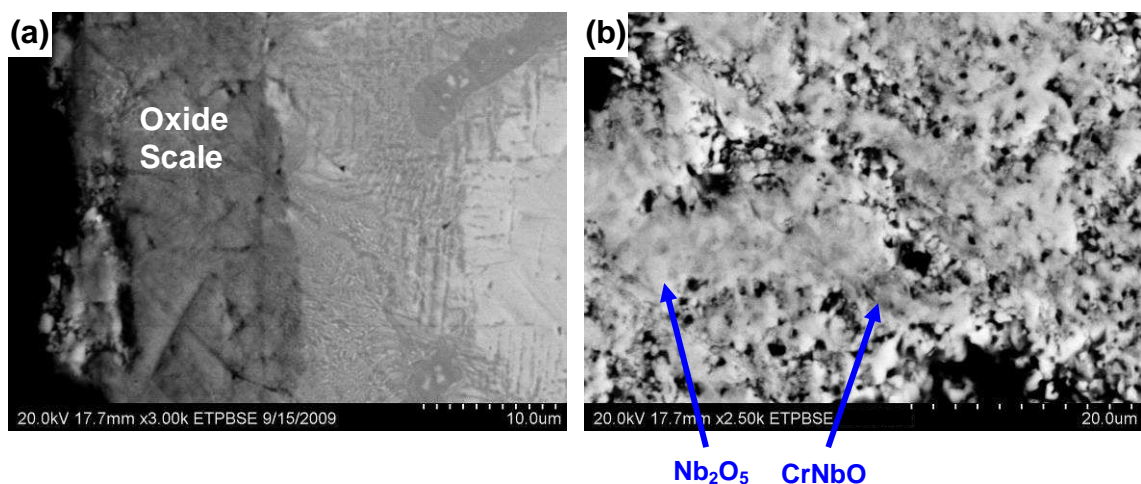


Figure 4.33: BSE images of the (a) metal-oxide interface, and (b) oxide scale of 15Cr alloy after 24 hours of exposure at 1100°C.

Figure 4.35 shows the metal oxide interface of 20Cr alloy oxidized at 1100°C for 24 hours. The oxide scale consists of a mixture of Nb_2O_5 (light gray areas), CrNbO_4 (dark gray areas), and irregular porosity. The distribution of the larger dark gray areas suggests that they are a product of the oxidation of the intermetallic phase into CrNbO_4 . Larger pores are observed adjacent CrNbO_4 areas which may be considered higher stress zones. This characteristic was less evident in oxide scale of 15Cr alloy possibly because CrNbO_4 large areas are less frequent since the volume fraction of intermetallic is smaller.

The oxide-metal interface images of sample 25Cr oxidized at 1100°C for 24 hours are presented in Figure 4.36. The oxide scale is a combination of Nb_2O_5 (light gray areas) and CrNbO_4 (dark gray areas). The oxide layers contain fissures parallel to the metal surface which are more evident at the areas where CrNbO_4 formed from the intermetallic phase, these areas are prone to spallation as shown in (Figure 4.36a).

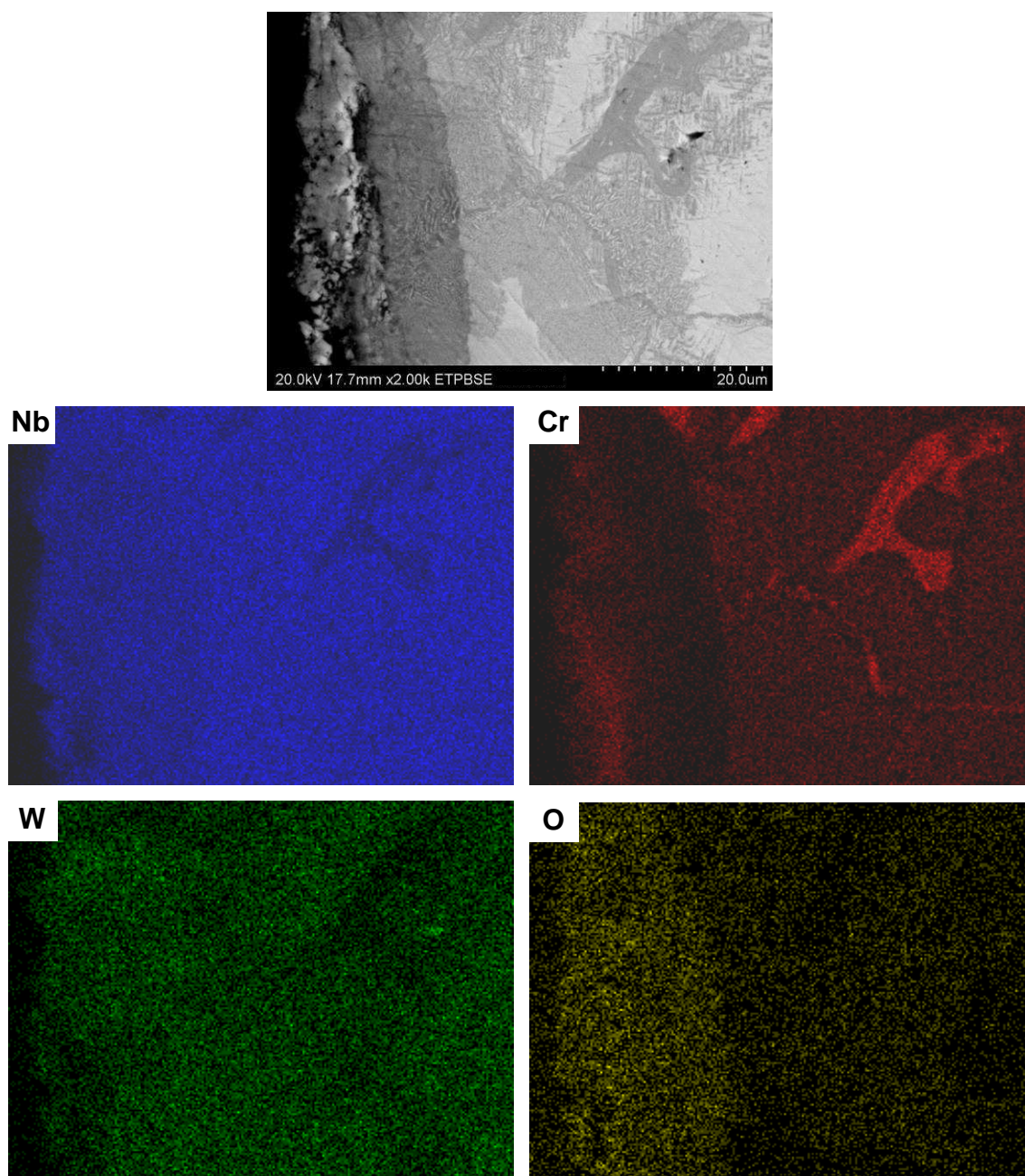


Figure 4.34: BSE image and X-ray maps showing Nb, Cr, W, and O distribution for 15Cr alloy oxidized 24 hours at 1100°C.

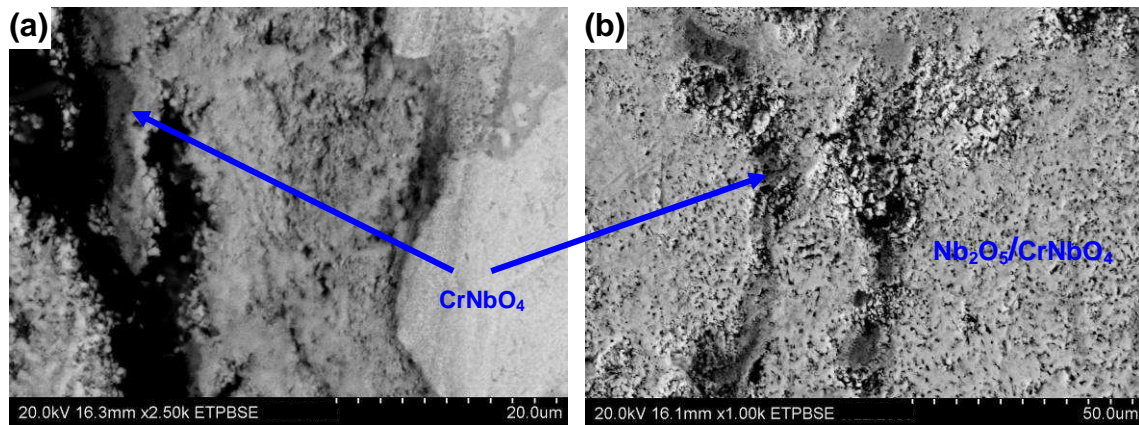


Figure 4.35: BSE images of the (a) metal-oxide interface, and (b) oxide scale of 20Cr alloy after 24 hours of exposure at 1100°C.

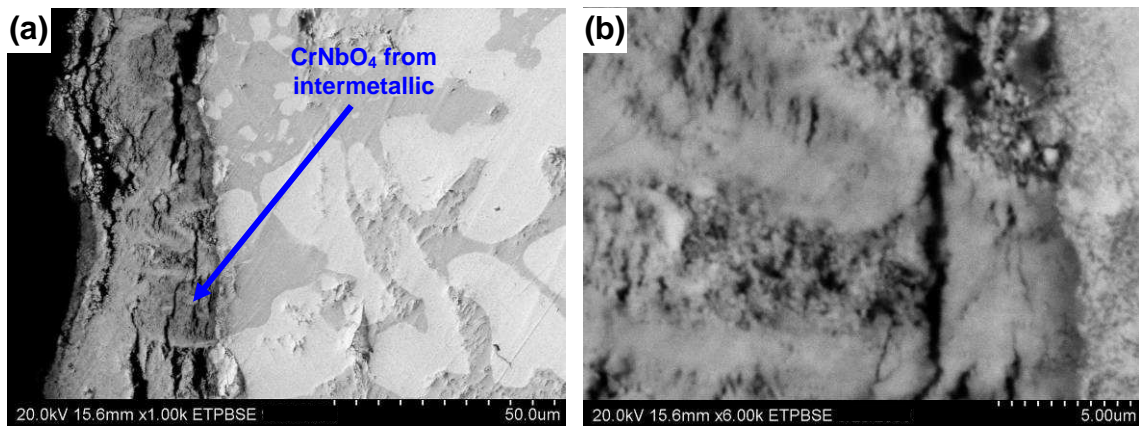


Figure 4.36: BSE images of the (a) metal-oxide interface, and (b) oxide scale of 25Cr alloy after 24 hours of exposure at 1100°C.

Figure 4.37 presents the metal oxide interface and oxide scale of 30Cr alloy oxidized at 1100°C. The oxide scale spalls easily and it separated from the metal interface when it was transferred from the crucible to the resin mold. The oxide scale consists of alternated layers of CrNbO_4 and Nb_2O_5 with CrNbO_4 areas, the layers tend to separate mainly at the CrNbO_4 layers and have a thickness of approximately 30 microns. The formation of this buckled layered structure is consequence of the stress

developed at the interface, a scale will spall if the stress is high, or the scale reaches a critical thickness causing the formation of layers with similar thicknesses.

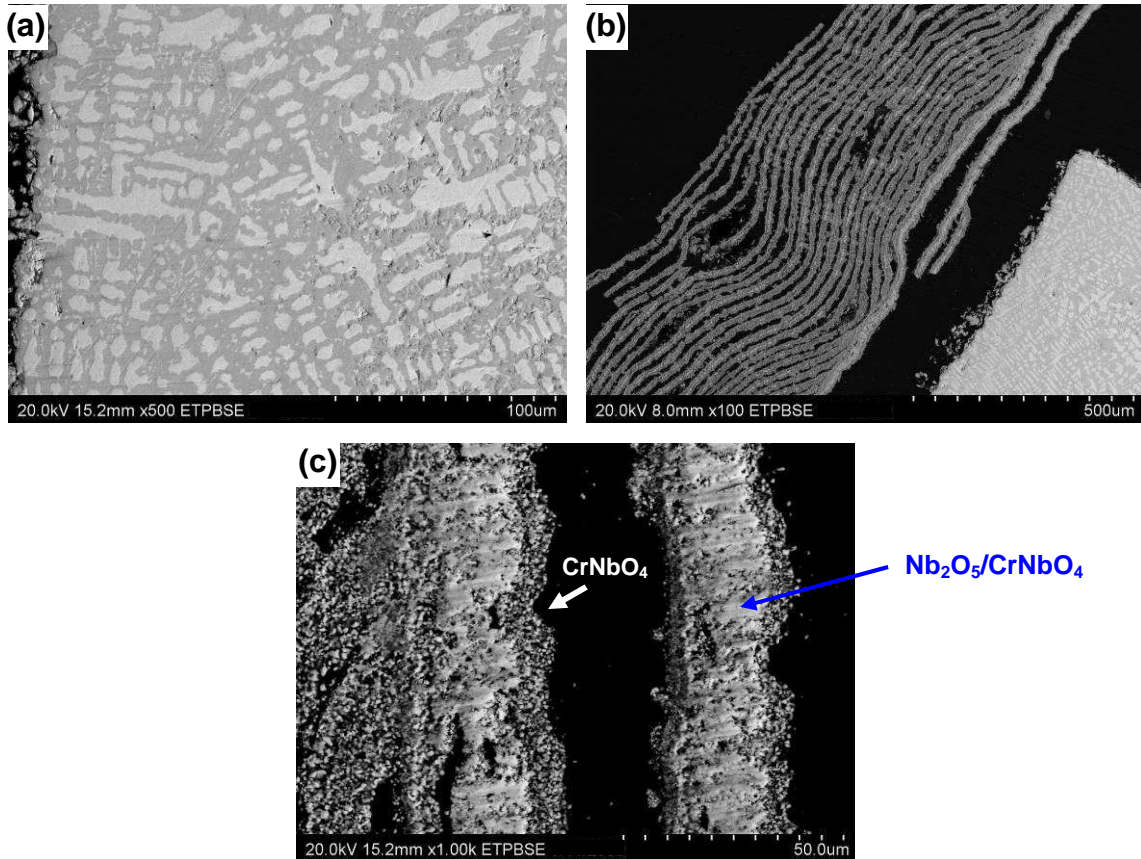


Figure 4.37: BSE images of the (a) metal-oxide interface, (b) and (c) oxide scale of 30Cr alloy after 24 hours of exposure at 1100°C.

The oxide-metal interface images of 15Cr, 20Cr, 25Cr and 30Cr oxidized at 1300°C for 24 hours are presented in Figures 4.38 to 4.45. The oxide scale on 15Cr alloy is a mixture of Nb_2O_5 (light gray areas) and CrNbO_4 (dark gray areas), however there are no alternating layers or fissures as the ones observed at 900°C and 1100°C; instead a more compact scale with small pores is formed. The distribution of CrNbO_4

appears to follow the distribution of the intermetallic phase indicating that the formation of this oxide it is more frequent at the NbCr_2 regions.

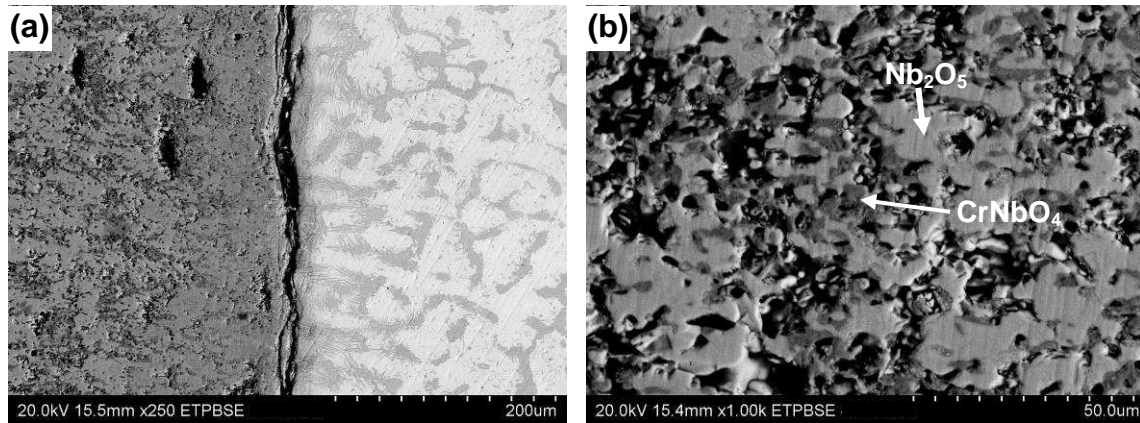


Figure 4.38: Cross-section BSE images of the metal-oxide interface (a) and oxide layer (b) of 15Cr alloy after 24 hours of exposure at 1300°C.

Figure 4.39 presents X-ray maps showing the Nb, Cr, W, and O distribution for 15Cr alloy at 1300°C. A Cr depletion layer of approximately 20 microns can be observed at the metal-oxide interface, which may be indicating that at this temperature the oxidation process occurs not only by inward diffusion of oxygen but also by means of outward diffusion of Cr. However the Cr content of the alloy might not be enough to form a layer of Cr_2O_3 at the metal-oxide interface as observed frequently in Cr alloys.

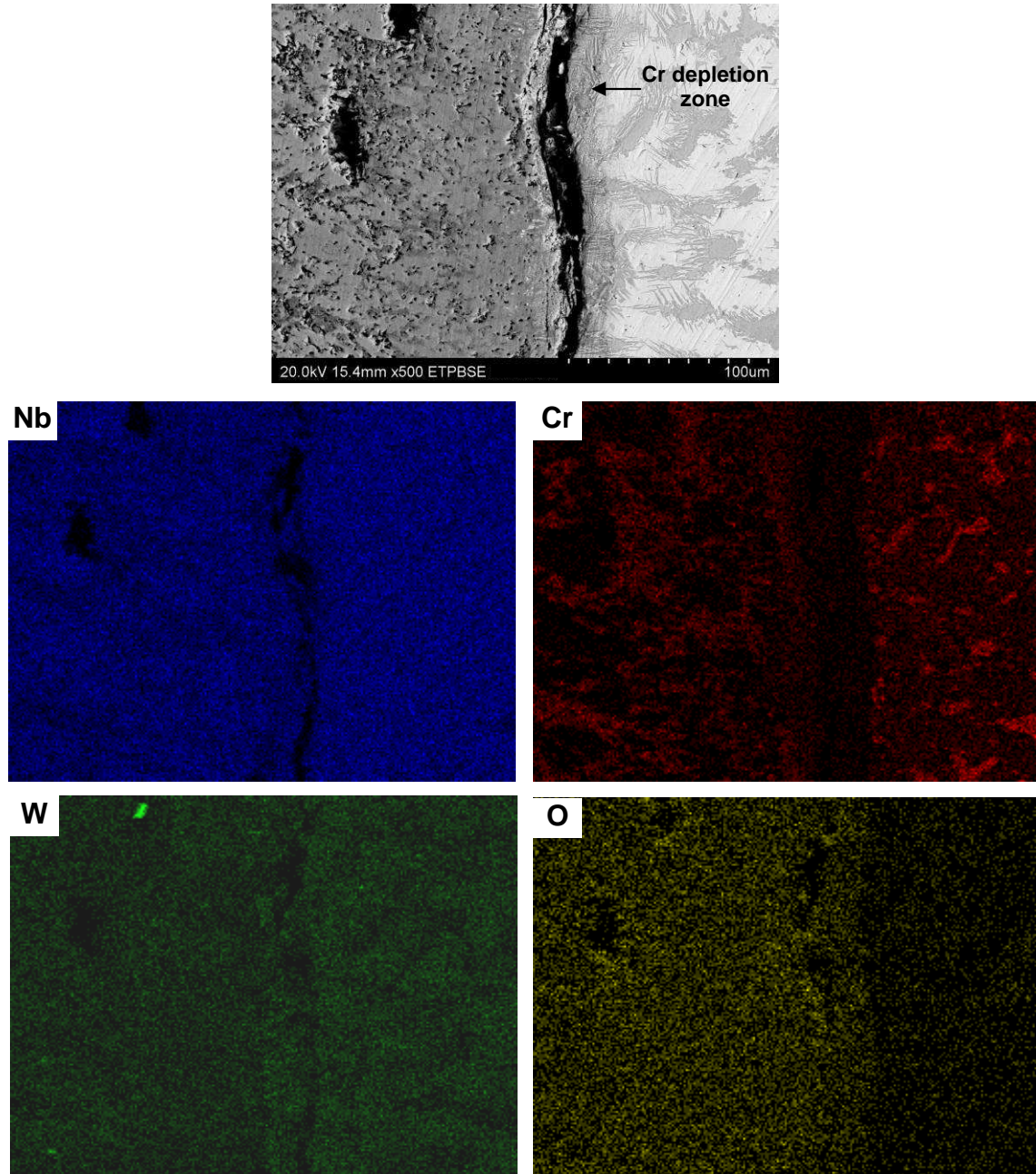


Figure 4.39: BSE image and X-ray maps showing Nb, Cr, W, and O distribution for 15Cr alloy oxidized 24 hours at 1300°C.

A Cr depletion zone of approximately 50 microns is also observed for 20Cr alloy (Figures 4.40 and 4.41). The oxide scale is a mixture of Nb_2O_5 (light gray areas) and CrNbO_4 (dark gray areas) and uniformly distributed pores (Figure 4.40b). Dark areas were observed at the edge of the oxide layer next to the metal as shown in Figure 4.41

which is a BSE image and elemental X-ray maps of the metal edge. The EDS elemental analysis indicates that the Cr/O ratio is approximately 0.7, which leads to believe that this layer might be Cr_2O_3 . However this assumption is only based on the EDS analysis, the XRD analysis did not reveal the presence of this oxide, but according to the thickness of this layer, the amount of this oxide might be too small to be detected in the oxide scales or stayed at the metal surface when the oxides were spalled off for analysis. Chromia (Cr_2O_3) evaporates in the form of CrO_3 at high temperatures, the evaporation becomes important at temperatures higher than 1000°C and near atmospheric oxygen partial pressures. The vaporization losses are reduced in static air since a large fraction of the evaporating molecules are reflected back on the surface, also the presence of other oxides on top of the Cr_2O_3 layers may inhibit the evaporative loss [57, 58]. Evidence of the presence of Cr_2O_3 at the external oxide layers is not observed which leads to believe that the chromia initially formed reacted with Nb_2O_5 to form CrNbO_4 .

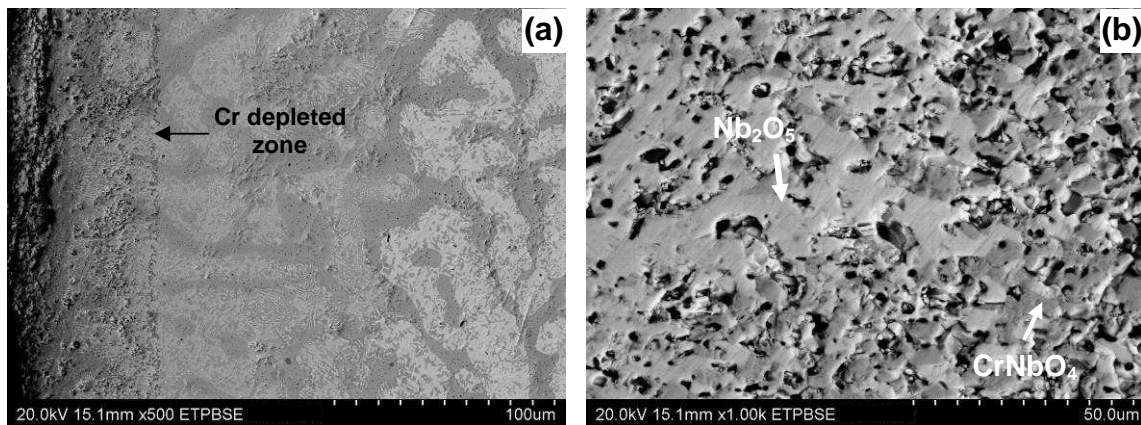


Figure 4.40: Cross-section BSE images of the metal-oxide interface (a) and oxide scale (b) of 20Cr alloy after 24 hours of exposure at 1300°C .

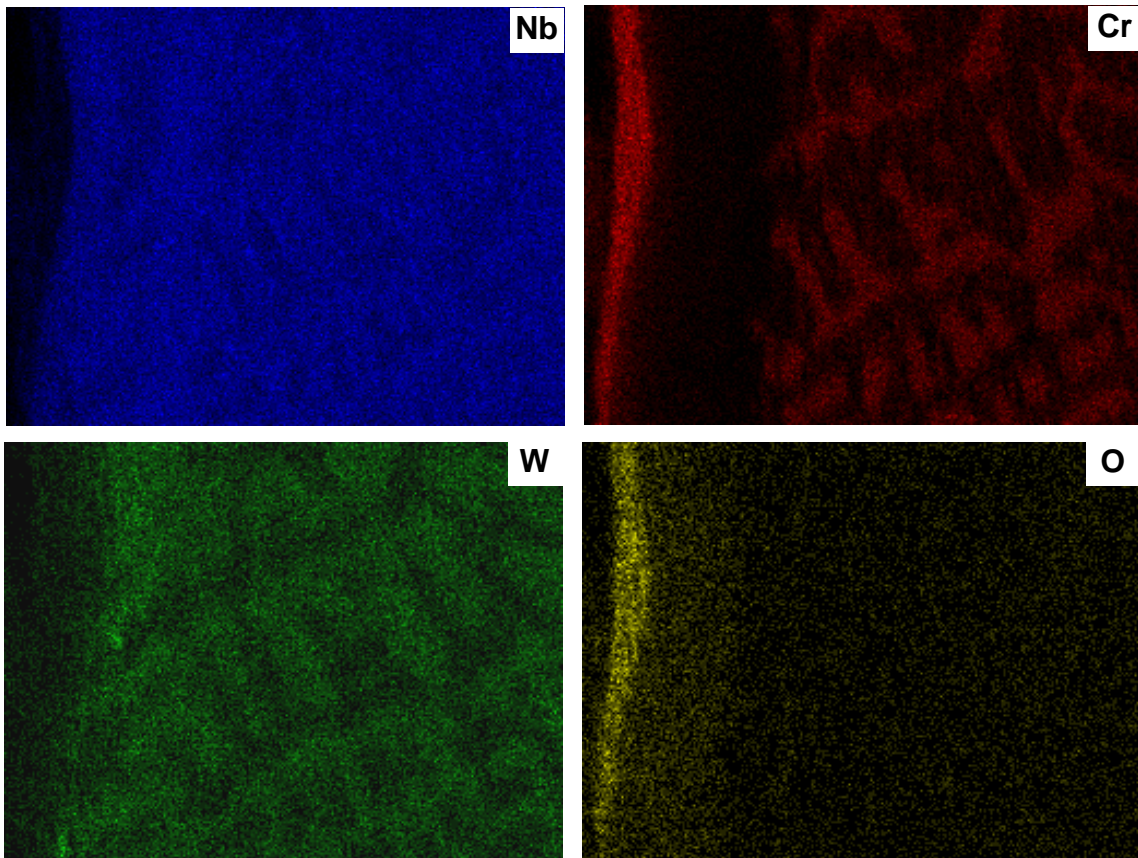
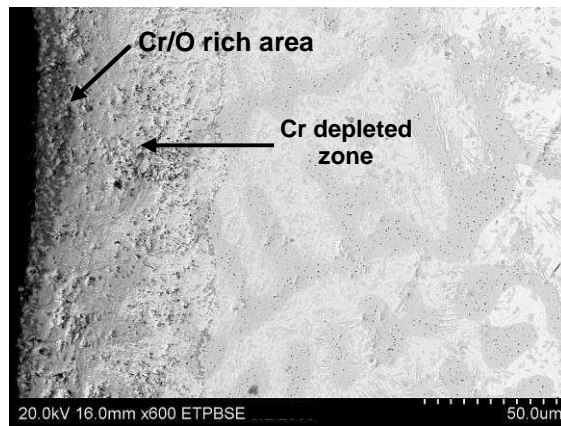


Figure 4.41: BSE image and X-ray maps showing Nb, Cr, W, and O distribution for 20Cr alloy oxidized 24 hours at 1300°C.

Figures 4.42 to 4.45 present images of the metal-oxide interface and oxide scale of 25Cr and 30Cr alloys. The oxide scale consists of multiple layers with a

mixture of Nb_2O_5 and CrNbO_4 (Figure 4.42) instead of a compact scale as observed for 15Cr and 20Cr alloys.

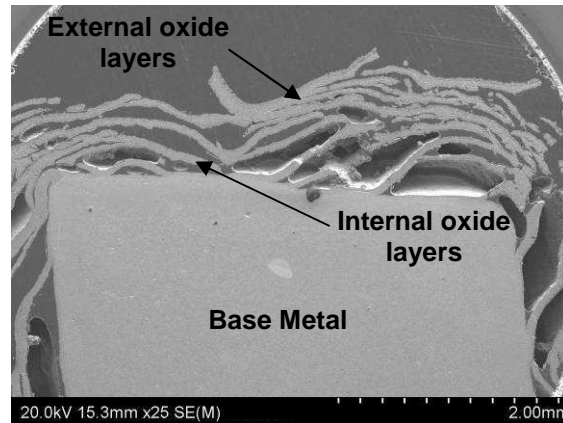


Figure 4.42: SEM images of the oxide layers formed on 25Cr and 30Cr alloys after 24 hours of exposure at 1300°C.

The metal-oxide interface of 25Cr and 30Cr alloys also exhibits a Cr depleted zone of approximately 50 microns and a Cr/O rich layer of around 10 microns as shown in Figures 4.43 and 4.44. A BSE image and the X-ray maps showing Nb, Cr, W, and O distribution for 30Cr alloy is presented in Figure 4.45. The oxidation mechanism might be explained as follows:

- a. Outward diffusion of Cr and oxygen inward diffusion to form a thin Cr_2O_3 layer at the metal-oxide interface.
- b. Formation of a inner oxide layer with mixed CrNbO_4 and Nb_2O_5 (Figures 4.43a and 4.44a)
- c. Spallation of the oxide scale once it reaches a critical thickness (Figures 4.43a and 4.44a).
- d. Separation of the oxide layer leaves a new metal surface for the formation of a new layer.

- e. The internal oxide layers (Figure 4.42) contain a mixture of Nb and Cr oxides as shown in Figures 4.43b and 4.44b.
- f. Evidence of the presence of Cr_2O_3 at the external oxide layers (Figures 4.42 and 4.43b) is not observed which leads to believe that the chromia initially formed reacted with Nb_2O_5 to form CrNbO_4 .

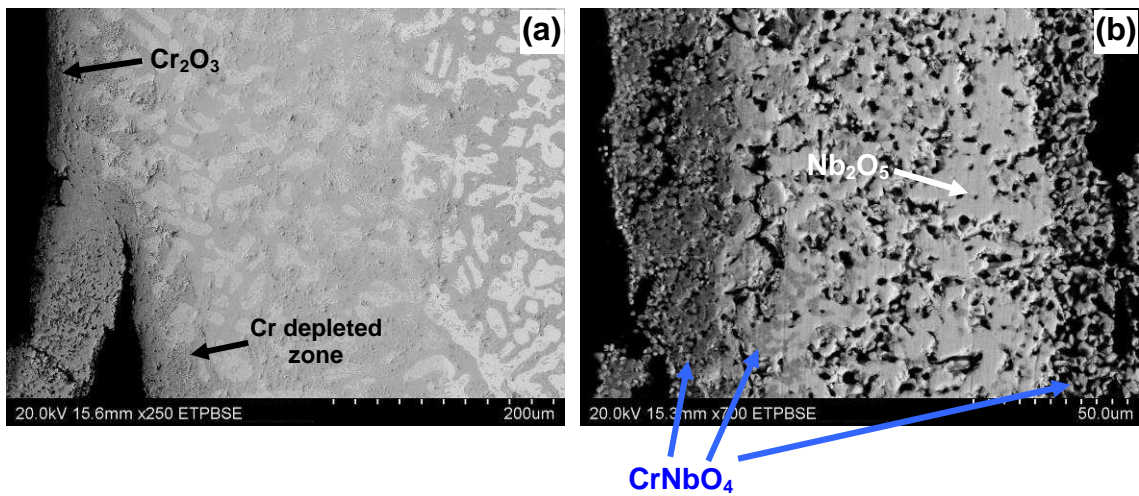


Figure 4.43: Cross-section BSE images of the metal-oxide interface (a) and an external oxide layer (b) for 25Cr alloy after 24 hours of exposure at 1300°C.

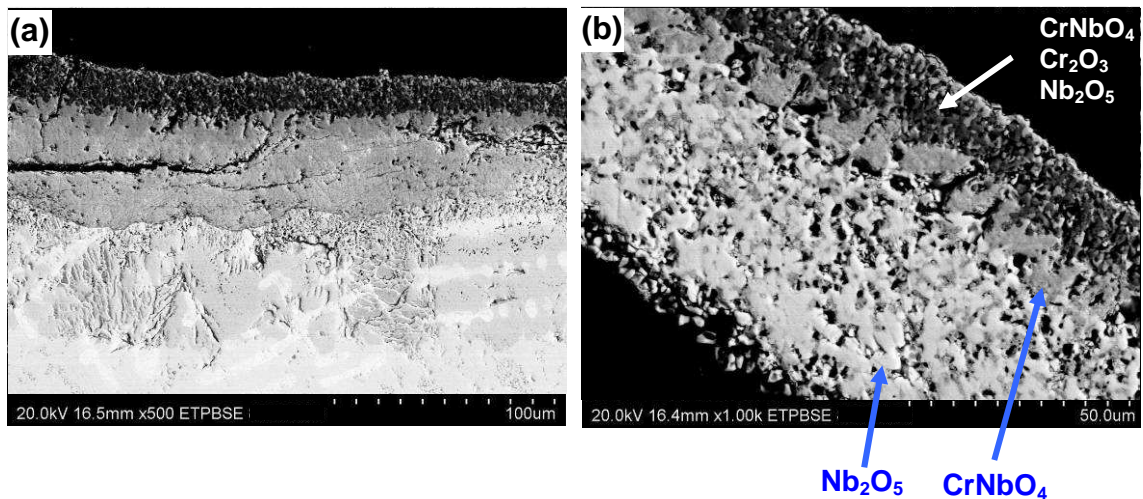


Figure 4.44: Cross-section BSE images of the metal-oxide interface (a) and internal oxide layer (b) of 30Cr alloy after 24 hours of exposure at 1300°C.

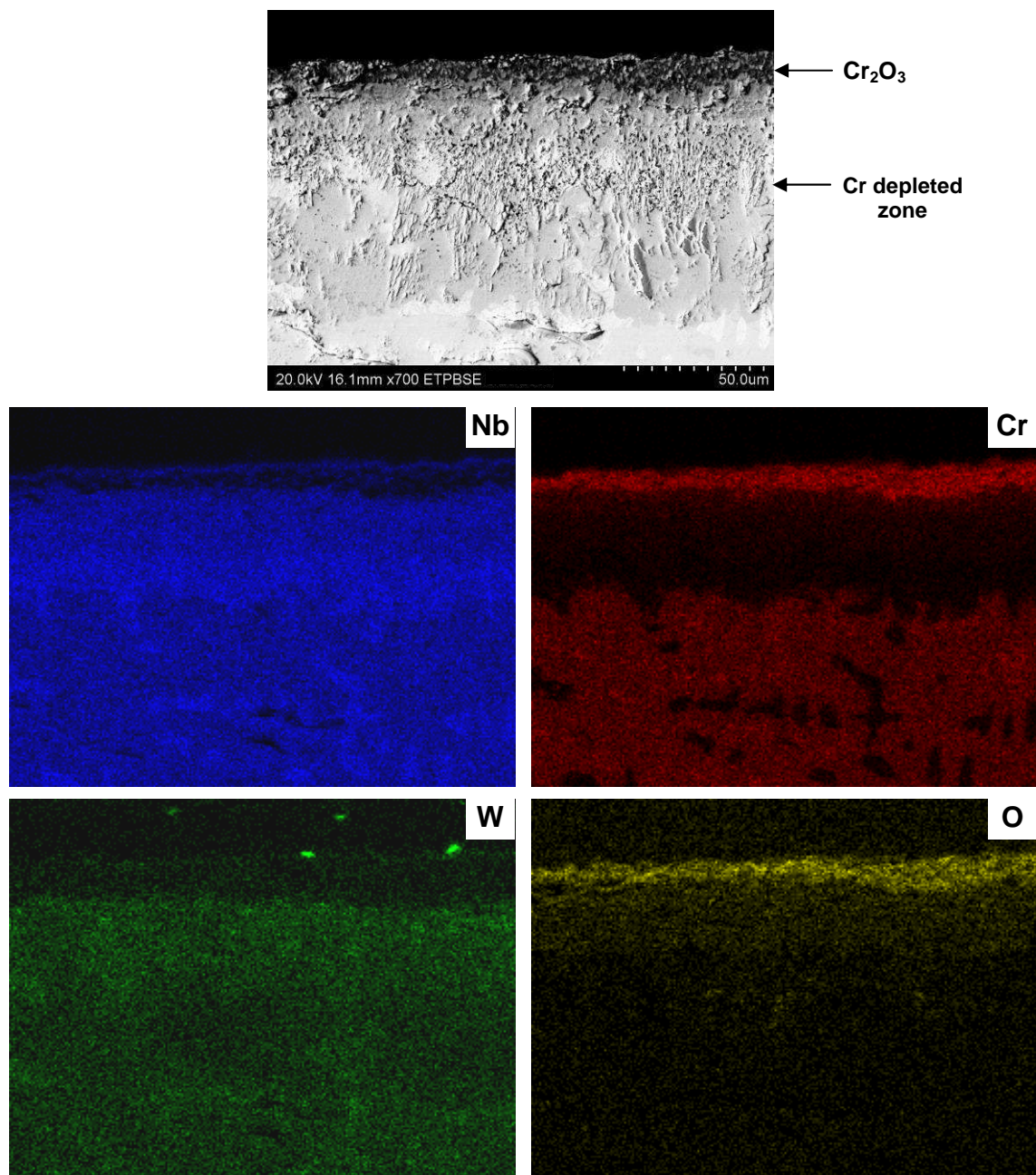


Figure 4.45: BSE image and X-ray maps showing Nb, Cr, W, and O distribution for 30Cr alloy oxidized 24 hours at 1300°C.

Table 4.4 presents the elemental composition as determined by EDS analysis of the different oxides at 900, 1100, and 1300°C. The identification of the oxides was based on the results obtained from XRD analysis.

Table 4.4: Elemental compositions (at%) of the oxides formed after 24 hours of exposure.

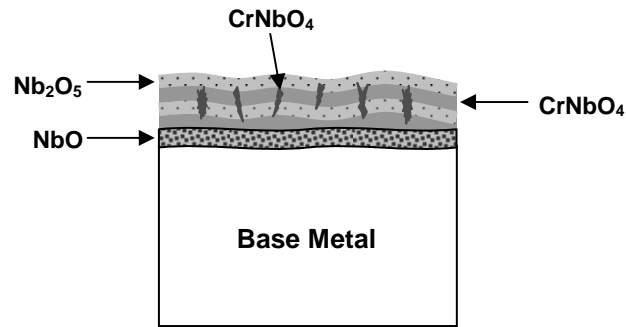
Alloy	Temperature	Oxide	Composition (at%)			
			Nb	Cr	W	O
15Cr	900°C	Nb ₂ O ₅	32.8-38.4	3.2-8.6	2.4-3.5	53.1-57.2
		CrNbO ₄	21.9-27.0	17.7-23.8	0.7-1.5	53.5-53.7
		NbO	43.7-46.3	1.9-5.5	4.0-4.9	45.5-49.6
	1100°C	Nb ₂ O ₅	35.9-37.2	1.5-2.7	2.6-4.5	55.8-59.9
		CrNbO ₄	22.3-25.7	18.3-22.0	0.8-1.6	50.7-58.5
	1300°C	Nb ₂ O ₅	37.5-39.2	3.9-6.3	2.8-3.6	53.2-53.4
CrNbO ₄		24.6-25.0	23.5-24.0	1.3-2.1	49.4-50.0	
20Cr	900°C	Nb ₂ O ₅	34.2-35.5	2.8-4.1	2.9-4.1	57.6-58.8
		CrNbO ₄	18.9-19.7	17.9-24.5	1.0-1.2	55.7-61.3
	1100°C	Nb ₂ O ₅	27.1-37.9	1.9-6.7	2.4-4.6	56.1-62.9
		CrNbO ₄	22.7-24.4	19.7-20.2	0.8-1.2	53.2-54.9
	1300°C	Nb ₂ O ₅	40.2-41.8	0.4-0.6	3.4-5.1	54.1-54.4
		CrNbO ₄	23.2-28.9	20.8-23.7	0.5-2.0	47.9-52.9
25Cr	900°C	Nb ₂ O ₅	29.0-30.9	7.2-9.9	0.9-2.6	59.6-61.0
		CrNbO ₄	19.2-27.1	18.8-24.6	1.2-1.7	46.6-58.2
	1100°C	Nb ₂ O ₅	36.0-38.3	4.3-6.7	3.8-5.2	51.7-54.4
		CrNbO ₄	22.1-23.8	18.9-20.1	0.9-2.0	55.3-56.9
	1300°C	Nb ₂ O ₅	36.9-39.8	0.8-1.7	3.6-4.3	55.3-57.8
		CrNbO ₄	21.8-27.7	21.5-27.1	1.1-1.6	45.5-52.2
Cr ₂ O ₃		2.4-8.9	32.8-46.9	0.3-0.9	50.1-57.5	
30Cr	900°C	Nb ₂ O ₅	32.5-34.0	6.5-7.1	3.1-3.6	55.2-57.9
		CrNbO ₄	21.3-22.9	26.1-28.9	0.9-1.2	48.8-49.7
	1100°C	Nb ₂ O ₅	36.6-37.5	3.6-8.7	2.9-5.0	50.6-54.7
		CrNbO ₄	18.8-23.7	17.3-22.9	0.7-1.14	52.3-63.2
	1300°C	Nb ₂ O ₅	37.5-40.3	0.7-1.2	3.2-3.3	55.2-58.7
		CrNbO ₄	17.1-22.4	14.6-22.8	0.4-1.1	55.3-68.0
Cr ₂ O ₃		0.7-2.0	38.9-44.8	0.1-0.2	54.2-58.8	

4.3.3 Oxidation Models

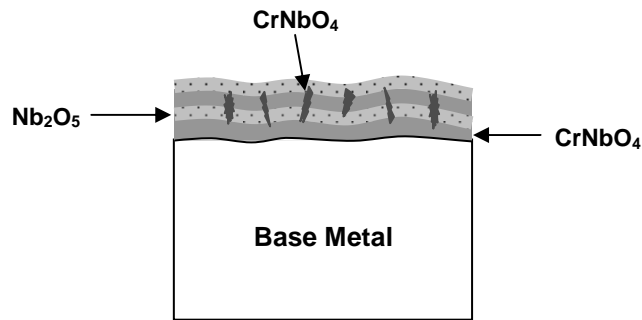
Gesmundo and Gleeson discussed the oxidation behavior of multicomponent two-phase alloys [63], and presented various oxidation behaviors for this type of alloys. These include (1) two phases oxidizing independently to form a non uniform scale, (2) two phases oxidizing cooperatively to form a uniform scale and (3) a continuous oxide scale that grows because a solute rich second phase acts as a reservoir (Figure 2.9). Similar models were constructed by applying these concepts in the context of the studied system.

Figures 4.46 and 4.47 show the proposed schematic diagrams for the oxidation of the alloys at 900 and 1300°C. In the case of 15Cr alloy at 900°C, the two phases oxidize cooperatively to form alternated layers of CrNbO_4 and Nb_2O_5 . 20Cr alloy presents a combination of two mechanisms, cooperative oxidation to form alternated layers and independent oxidation of the Laves phase to form CrNbO_4 zones.

The two phases oxidize cooperatively to form a scale with a mixture of CrNbO_4 and Nb_2O_5 oxides at 1300°C. Outward diffusion results in the formation of a Cr depleted zone. The Cr concentration in the 15Cr and 20Cr alloys is not enough to form a Cr_2O_3 layer at the interface; however a continuous layer of Cr_2O_3 is formed at metal interface of 25Cr and 30Cr alloys. According to the features observed in the oxide scale formed at 1100°C, this temperature might be considered as an intermediate temperature where a combination of the lower and higher temperature models apply.

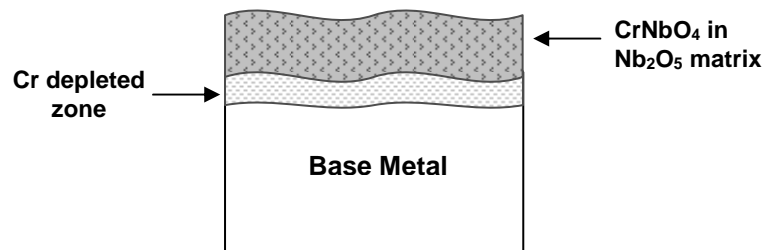


(a)

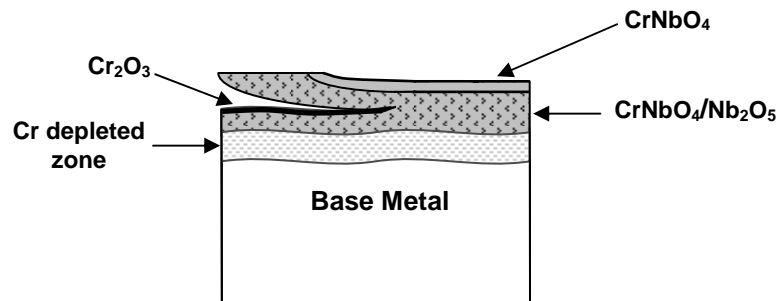


(b)

Figure 4.46: Schematic representation of the oxide scale formed on samples oxidized at 900°C. (a) 15Cr alloy. (b) 20Cr alloy.



(a)



(b)

Figure 4.47: Schematic representation of the oxide scale formed on samples oxidized at 1300°C. (a) 15Cr and 20Cr alloys. (b) 25 Cr and 30Cr alloys.

4.4 Cyclic Oxidation

4.4.1 Oxidation Kinetics

The oxidation rates of all the alloys were measured at 900°C and 1300°C in static air. The cyclic oxidation experiments were performed by periodic removal of the specimen every 4 hours after it cooled in the furnace to room temperature, the sample was then weighted and placed in the furnace for further oxidation at constant temperature for a total exposure time of 24 hours.

Figure 4.48 shows the weight gain per unit area as a function of the exposure time at 1300°C for the alloys 15Cr, 20Cr, 25Cr, and 30Cr. The oxidation behavior of all the alloys follows a parabolic law at this temperature. Alloys with higher chromium concentration show a significant improvement on oxidation resistance when compared to alloys containing 20% Cr or lower. The alloy containing 15% Cr exhibits the lowest oxidation resistance with a weight gain that is approximately 2.5 times the weight gained by 30Cr alloy. The alloys gained twice as much weight under cyclic conditions than under isothermal conditions, which is expected due to scale spallation that occurs during each cooling cycle, this will limit the ability of the alloy to form an effective protective layer. The alloy will experience accelerated oxidation because of the inverse relationship between the oxidation rate and the scale thickness [104].

The cyclic oxidation curves at 900°C are presented in Figure 4.49. The alloys with higher Cr content exhibit poor oxidation resistance at this temperature as observed for isothermal experiments. Weight gains under these conditions are approximately 30% higher than the gains under isothermal conditions at the same temperature.

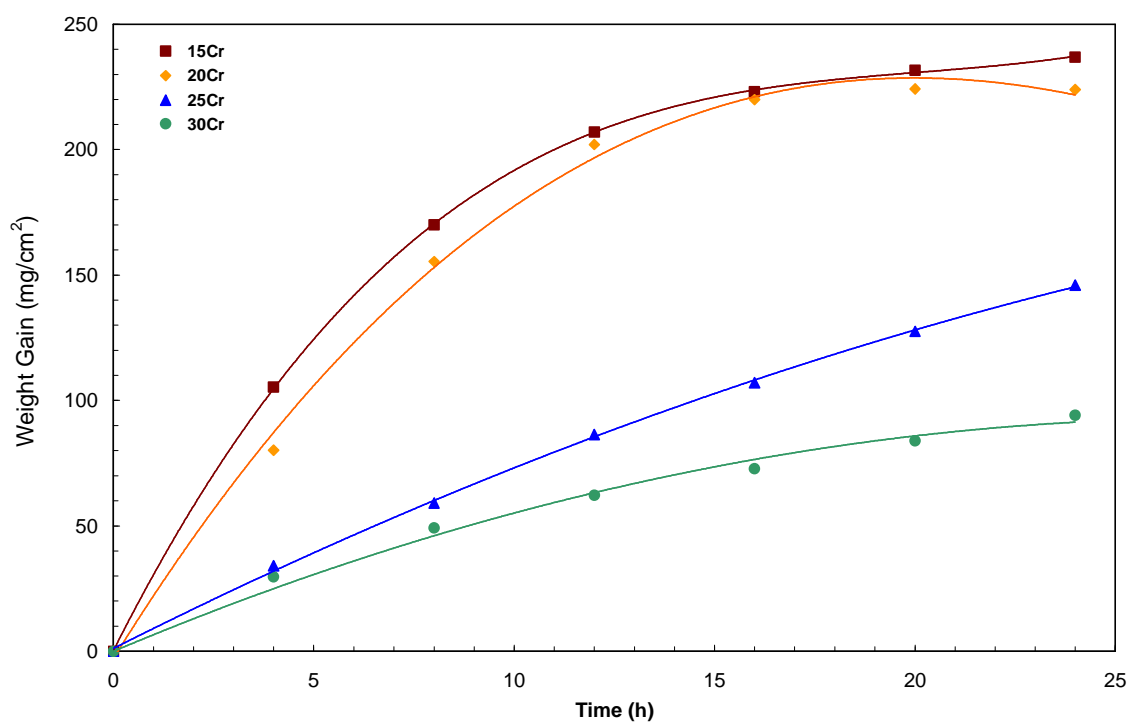


Figure 4.48: Cyclic oxidation curves for 15Cr, 20Cr, 25Cr, and 30Cr alloys at 1300°C.

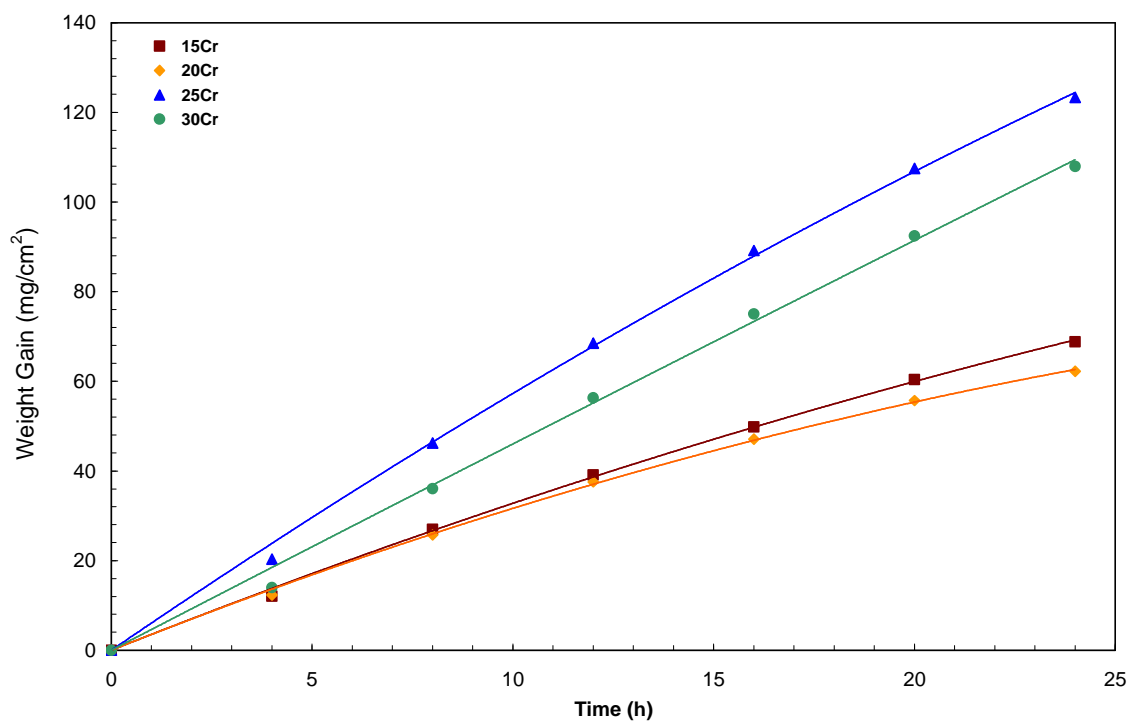


Figure 4.49: Cyclic oxidation curves for 15Cr, 20Cr, 25Cr, and 30Cr alloys at 900°C.

The parabolic rate constants for oxidation tests are listed in Table 4.5. At 900°C the alloys 25Cr and 30Cr follow a linear behavior rather than a parabolic since the oxidation rate does not decrease with time as it does in the case of parabolic oxidation (Figure 4.49). The oxidation kinetics follow a parabolic behavior at 1300°C for the four analyzed alloys; the addition of 30% of Cr resulted in the significant reduction of the parabolic oxidation rate.

Table 4.5: Values of parabolic rate constants (k_p) and correlation coefficients corresponding to cyclic exposure at 900°C and 1300°C [45].

Temperature	Alloy	Time Span (h)	k_p ($\text{mg}^2 \text{cm}^{-4} \text{h}^{-1}$)
900°C	15Cr	0-24	172.4
	20Cr	0-24	146.5
	25Cr	0-24	-
	30Cr	0-24	-
1300°C	15Cr	0-20	3021.4
	20Cr	0-20	2826.8
	25Cr	0-24	784.7
	30Cr	0-24	348.5

4.4.2 Oxide Scale Characterization

Figures 4.50 and 4.51 show the appearance of the alloys after cyclic oxidation for 24 hours at different temperatures. The oxide scale from alloys with lower Cr content (15Cr and 20Cr) consists of multiple well defined layers. This characteristic was also observed at 1300°C; however the layers from 20Cr alloy are prone to fragmentation. Evidence indicating that some metallic phase remains after 24 hours of exposure at 1300°C was not found, according to the oxidation curves and parabolic rate constant calculation complete oxidation of the alloy occurred after 20 hours of exposure.

The alloys containing 25 and 30% Cr suffered from powder formation at 900°C which is consistent with the high weight gains observed (Figure 4.51). The scale is not much different from the scale formed during static oxidation at this temperature. High Cr content alloys exhibited the best oxidation resistance at 1300°C, with smaller weight gains. The oxidation products obtained from alloys 25Cr and 30Cr alloys during isothermal oxidation at 1300°C consisted of multiple thin layers lightly attached to the metal surface (Figure 4.42), in the case of cyclic oxidation the layers separated from the metal oxide interface as shown in Figure 4.51 which limited the scale ability to act as a protective barrier.

4.4.2.1 SEM and EDS Analysis of Oxide-Metal Interfaces

The oxide-metal interface images of samples 15Cr oxidized at 900°C for 24 hours are presented in Figure 4.52. The oxide scale of 15Cr alloy consists of Nb_2O_5 and CrNbO_4 alternate layers. The oxide scale tends to spall more easily than the oxide layer formed during isothermal conditions (Figure 4.26). The first oxide layer has a lighter appearance than the successive layers (Figure 4.52b), EDS elemental analysis revealed a Nb/O ratio close to 1, which leads to believe that this first layer is the intermediate reaction product NbO; this layer was also observed in the case of isothermal oxidation. Figure 4.53 presents the metal interface of 30Cr alloy after cyclic oxidation at 900°C, the alloy presents numerous microcracks around the perimeter of the sample which causes alloy fragmentation before the complete oxidation of the phases. The lower oxidation resistance observed in 25Cr and 30Cr alloys at 900°C is again attributed to the cracking occurring at the metal surface. Figure 4.53b shows that the oxidation of the phases occurs after fragmentation.

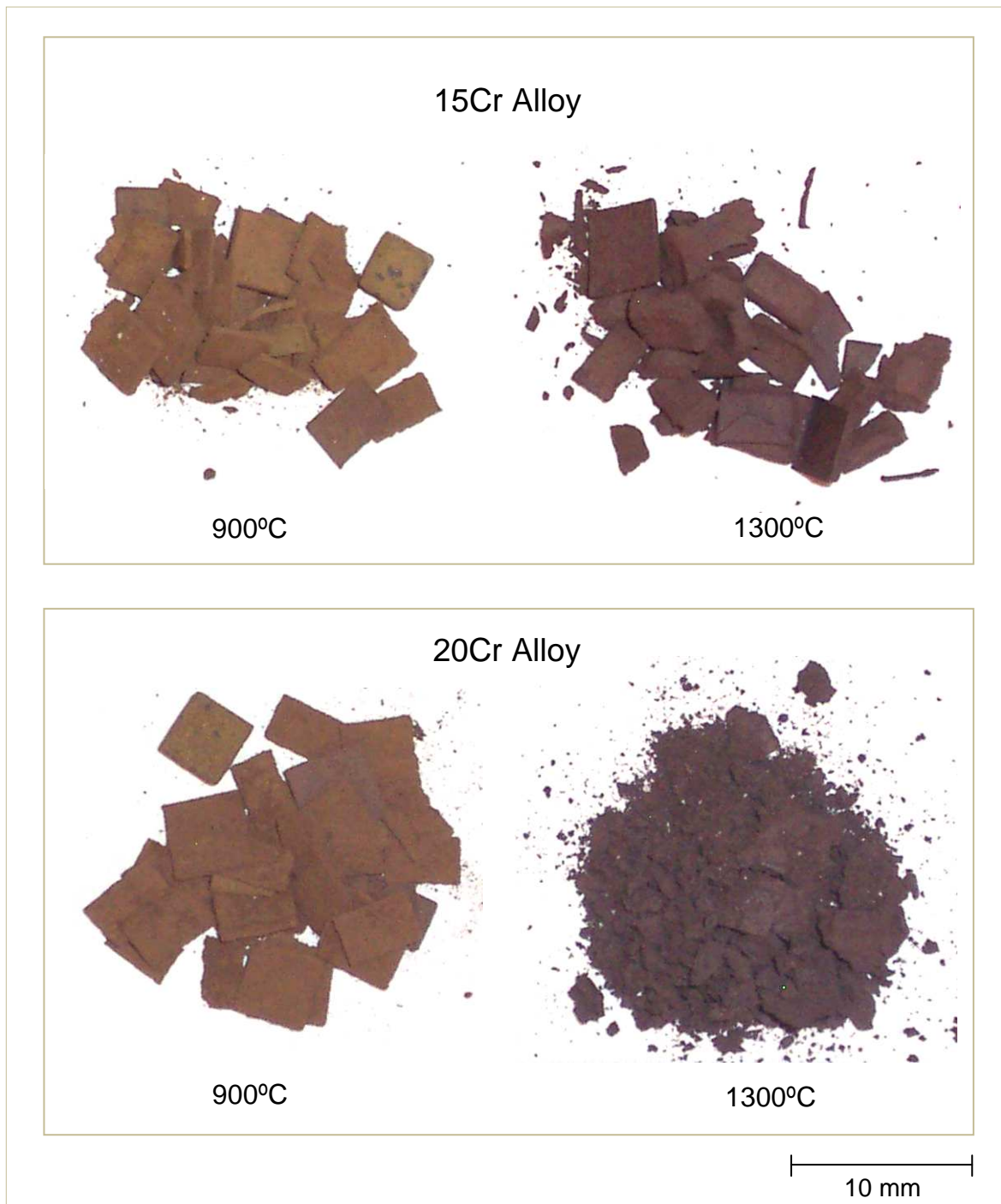


Figure 4.50: Oxidation products obtained from 15Cr and 20Cr alloys after cyclic oxidation for 24 hours in air.

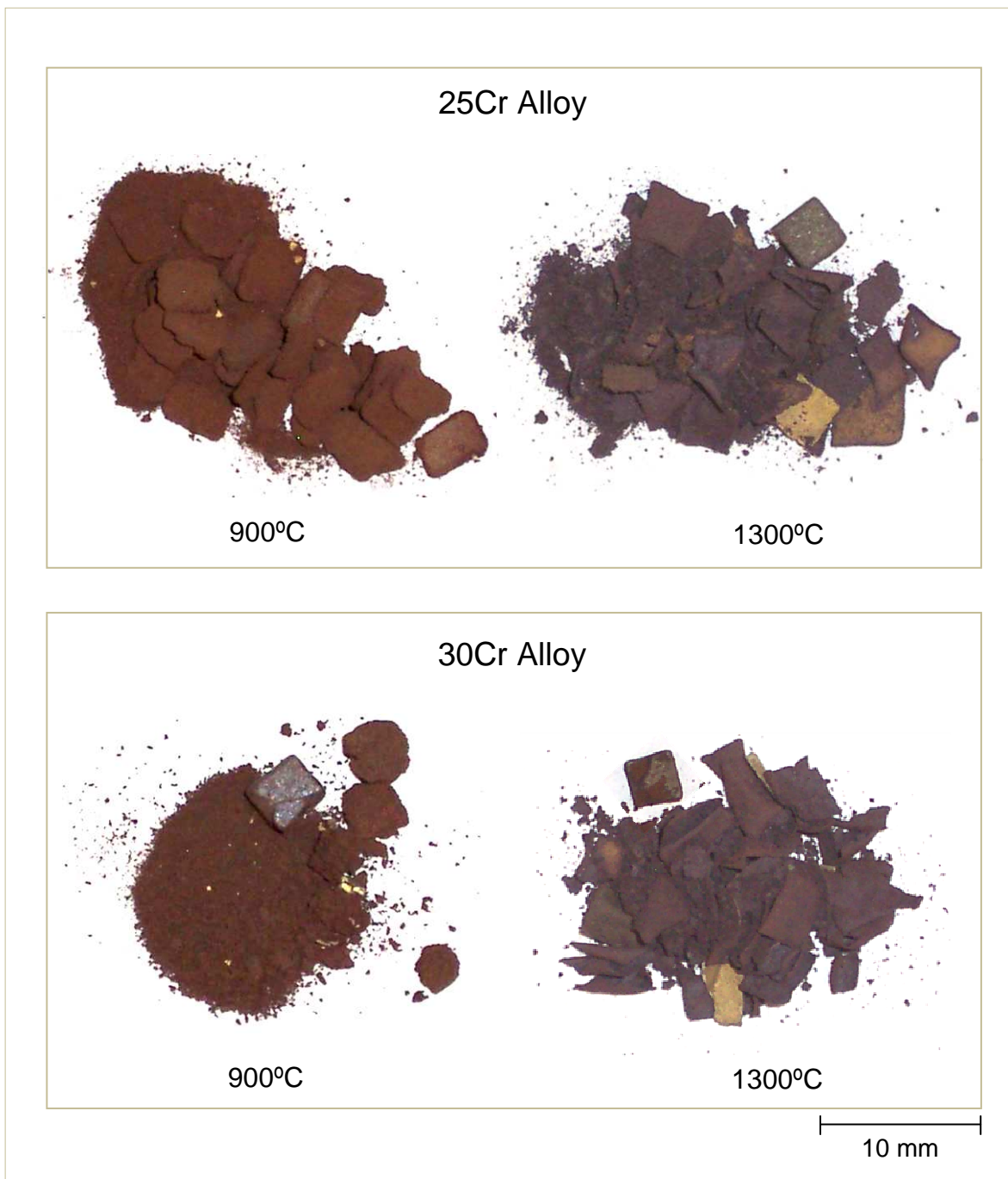


Figure 4.51: Oxidation products obtained from 25Cr and 30Cr alloys after cyclic oxidation for 24 hours in air.

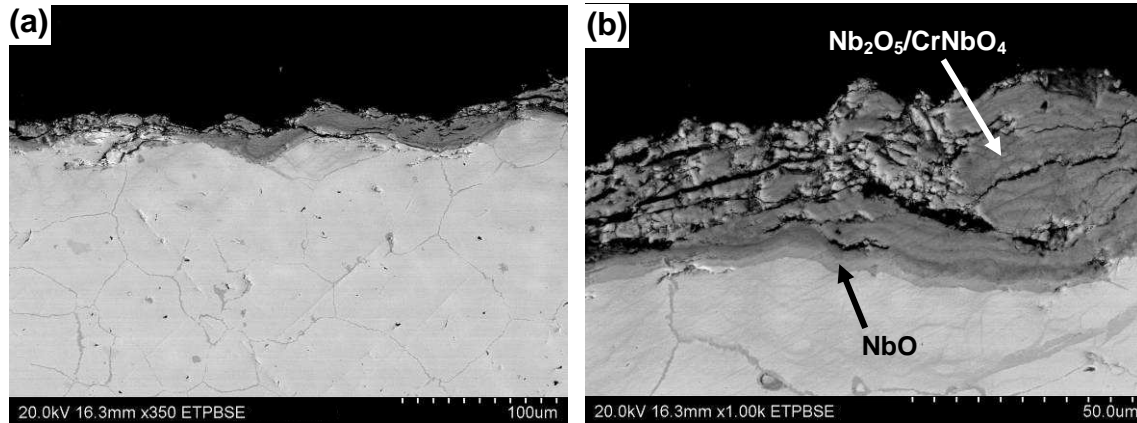


Figure 4.52: BSE images of the metal-oxide interface from 15Cr alloy after 24 hours of cyclic exposure at 900°C.

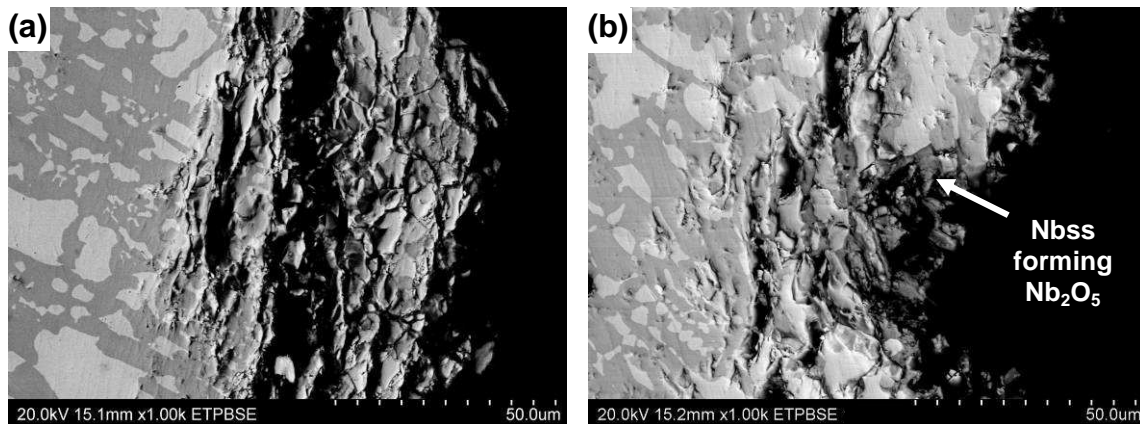


Figure 4.53: BSE images of the metal-oxide interface of 30Cr alloy after 24 hours of cyclic exposure at 900°C.

The oxide-metal interface images of sample 30Cr oxidized at 1300°C for 8 and 24 hours are presented in Figure 4.54. The oxide formed is not continuous around the edge the first 8 hours, showing the preferential oxidation of the solid solution phase to form Nb_2O_5 which causes the formation of cracks parallel to the surface in the intermetallic regions. A Cr depleted zone, a Cr_2O_3 layer and multiple oxide layers at the interface as observed in the case of isothermal conditions were not evident after 24 hours of exposure (Figure 4.54b). However the interface presented in Figure 4.54b

is the result of the last cycle of the test and the oxide scale formed during the previous cycles spalled off. The only oxide scale left on the surface is a mixture of CrNbO_4 and Nb_2O_5 .

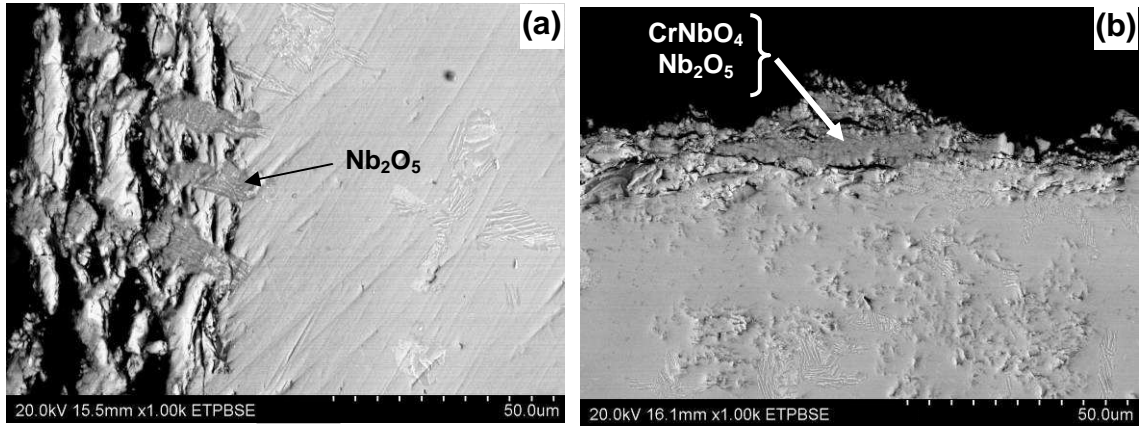


Figure 4.54: BSE images of the metal-oxide interface of alloy 30Cr after cyclic exposure at 1300°C for (a) 8 hours, and (b) 24 hours.

Figure 4.55 presents a SEM micrograph showing the metal oxide interface of 15Cr sample after oxidation at 1300°C for 8 hours. The EDS elemental analysis and BSE contrast were used to identify the composition of the oxidation products which are a mixture of Nb_2O_5 , CrNbO_4 , and irregular large pores. The oxide layer is most likely to be the oxidation product of only the last cycle of the test, therefore high oxidation rates are expected since the scale is thinner than the scale formed under isothermal conditions. The absence of an effective protective layer caused the complete oxidation of the 15Cr alloy before the 24 hours.

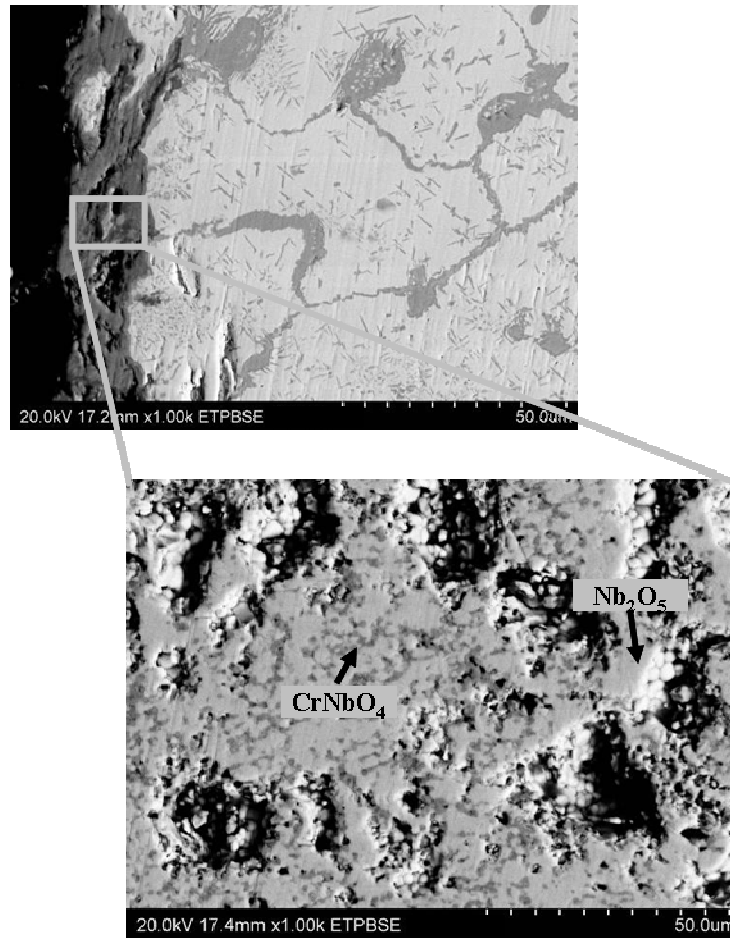


Figure 4.55: BSE images of the metal-oxide interface of alloy 15Cr oxidized for 8 hours at 1300°C.

4.4.2.2 Oxidation Products Analysis by X-ray Diffraction

Figure 4.56 and 4.57 present the XRD patterns obtained from the oxidation products of 15Cr, 20Cr, 25Cr, and 30Cr alloys after 24 hours of cyclic exposure at 900 and 1300°C respectively. The products are a mixture of CrNbO_4 and Nb_2O_5 as observed for isothermal oxidation. The Nb_2O_5 oxide formed at 1300°C is the high temperature modification, H-form; while the oxide from oxidation products obtained at

900°C is the M-form. As the Cr concentration increases the intensity of the M-Nb₂O₅ and H-Nb₂O₅ peaks decreases, thus CrNbO₄ is the predominant oxide in 30Cr alloy.

Figure 4.58 presents the intensity ratio of the CrNbO₄ reflection to the Nb₂O₅ reflection ($I_{\text{CrNbO}_4} / I_{\text{Nb}_2\text{O}_5}$) plotted as a function of the intermetallic phase volume percentage. The relative intensity ratio increases with the volume percent of intermetallic phase and the temperature, therefore the formation of CrNbO₄ is favored in alloys with higher volume percent of Laves phase at high temperatures (1300°C).

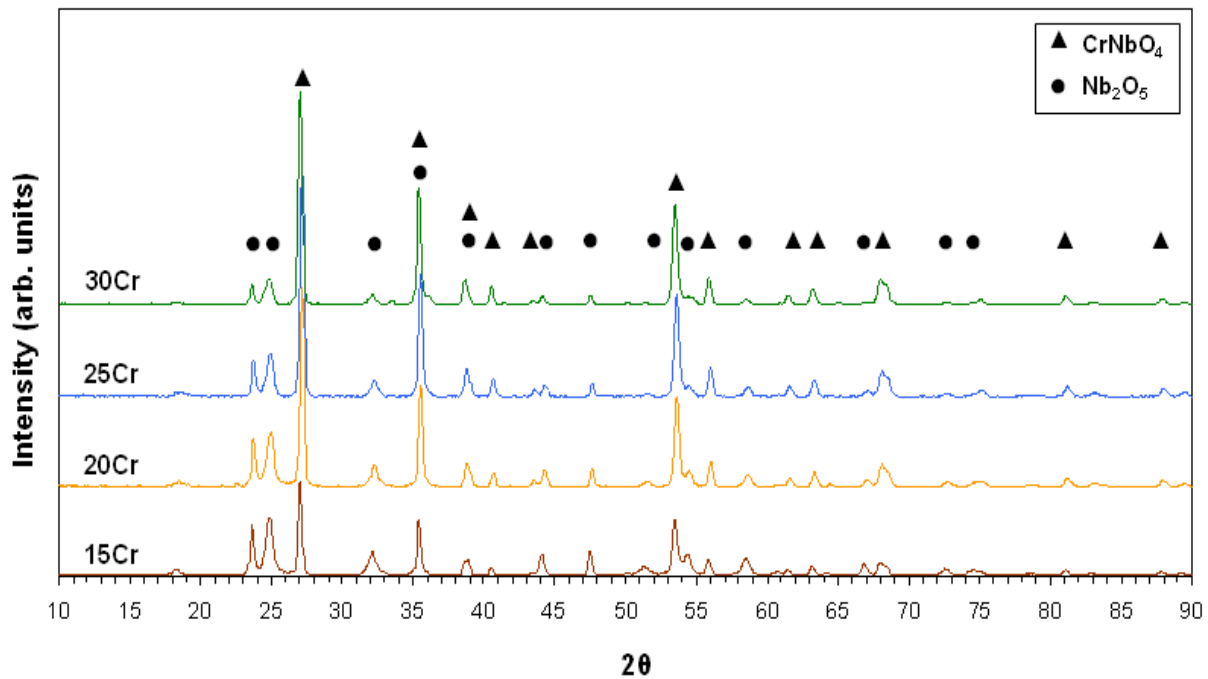


Figure 4.56: XRD pattern of the oxidation products obtained from the 4 alloys after 24 hours of cyclic exposure at 900°C.

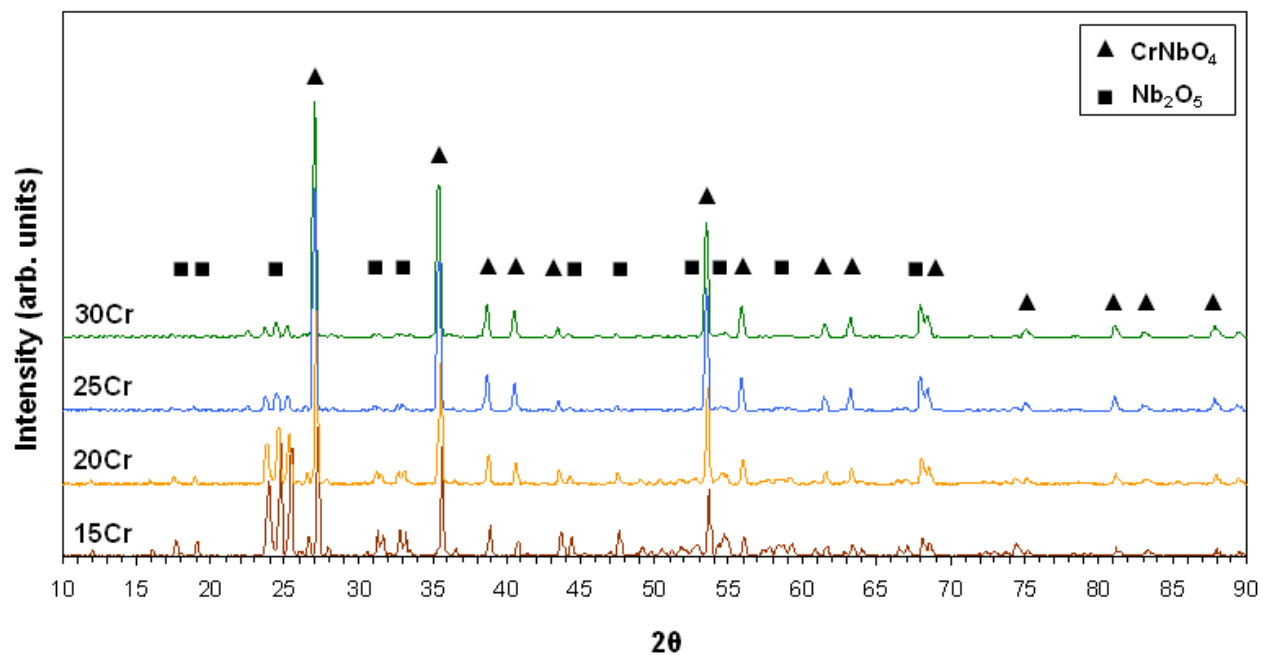


Figure 4.57: XRD pattern of the oxidation products obtained from the 4 alloys after 24 hours of cyclic exposure at 1300°C.

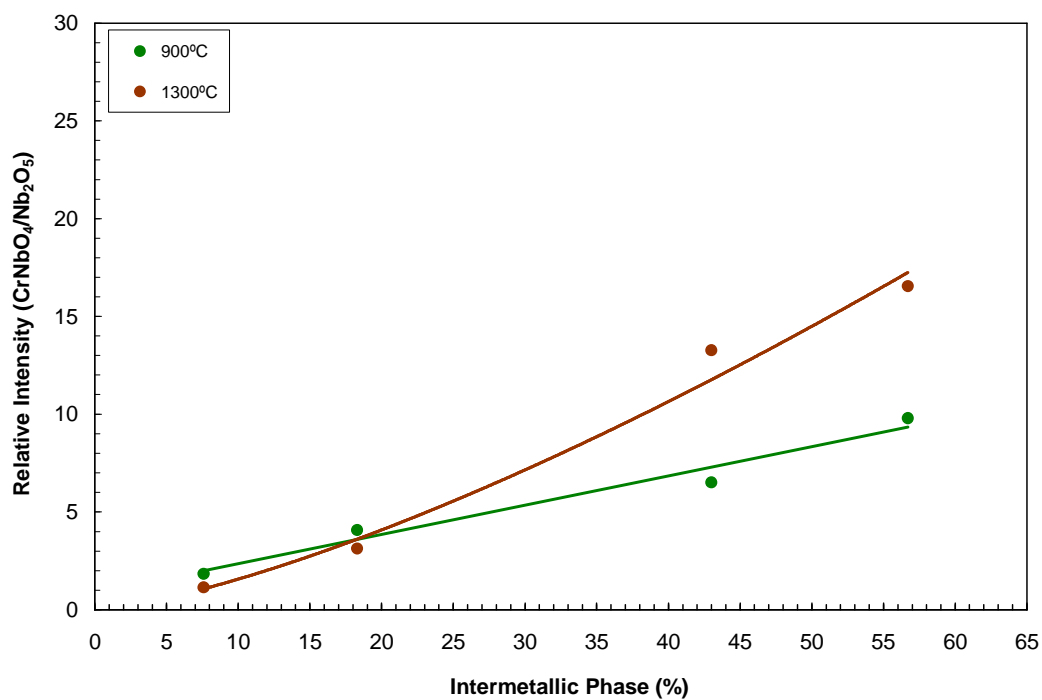


Figure 4.58: Relative intensity ratio as a function of the volume percentage of intermetallic phase for oxidation products of alloys oxidized under cyclic conditions.

CHAPTER 5

SUMMARY AND CONCLUSIONS

This work presents the results obtained from a study of the microstructural and oxidation characteristics of four alloys from the Nb-W-Cr system.

Alloy microstructure consists of Nb solid solution phase surrounded by a network of the NbCr₂ Laves phase. The amount of intermetallic phase is related to the amount of Cr content.

The oxidation kinetics for the four alloys follow a parabolic behavior at all the selected temperatures under isothermal conditions and the time at which the oxidation rate stabilizes is composition dependent. Alloys containing lower Cr concentrations exhibit better oxidation resistance than alloys with higher Cr content at 900°C; the unsatisfactory oxidation behavior of 25Cr and 30Cr alloys is related to microcrack formation at the alloy perimeter. Oxidation scale at 900°C consists of alternate layers of CrNbO₄, and Nb₂O₅ for 15Cr and 20Cr; and a mixture of CrNbO₄, and Nb₂O₅ in powder form for alloys with higher Cr concentration. At 1300°C, the Nb solid solution and the Laves phase oxidize cooperatively to form a scale with a mixture of CrNbO₄ and Nb₂O₅ oxides. Outward diffusion results in the formation of a Cr depleted zone and the formation of a thin layer of Cr₂O₃ at the oxide-metal interface in the case of alloys with higher Cr content. The addition of 30% Cr resulted in the significant reduction of the parabolic oxidation rate at 1100 and 1300°C.

Cyclic oxidation experiments revealed that 25Cr and 30Cr alloys follow a linear behavior at 900°C and exhibit poor oxidation resistance. As temperature increases there is a change in the oxidation kinetics of these alloys from linear to parabolic at

1100 and 1300°C. 15Cr and 20Cr alloys follow parabolic behavior at all temperatures. The alloys gained twice as much weight under cyclic conditions than under isothermal conditions, which is expected due to scale spallation that occurs during each cooling cycle, this will limit the ability of the alloy to form an effective protective layer.

The oxidation products of the alloys are a mixture of CrNbO_4 , and Nb_2O_5 . Two modifications of Nb_2O_5 were identified, M-form at 900°C and H-form at 1100 and 1300°C. Formation of CrNbO_4 is favored in alloys with higher volume percent of Laves phase at high temperatures (1300°C).

The oxidation behavior of the alloys is controlled by the volume fraction of intermetallic phase. Preferential attack of the Nb solid solution phase was observed in all the oxidized alloys.

Mass gain values and parabolic oxidation rate constants obtained at 1300°C for 25Cr and 30Cr alloys are competitive with the values for Nb-based alloys reported by different authors. The results obtained delineate the complexity of the oxidation mechanism and the influence of microstructure and composition of the alloys.

RECOMMENDATIONS

This work is an effort to explore the capabilities of Nb-W-Cr alloys as high temperature materials for power generation systems. The oxidation characteristics of four alloys from the Nb-W-Cr system with different Cr contents were discussed and the information obtained established a baseline that leads to a better understanding of the oxidation kinetics and the improvement of the oxidation resistance of Nb-based alloys.

The process of designing an alloy that performs effectively thought all the temperature range is an iterative one; and each study will provide new information from which new alloys can be developed.

It is expected that the following recommendations will reveal more interesting results and improve the oxidation behavior of alloys from this system:

- Future research should be oriented to improve the oxidation resistance of the alloys at intermediate temperatures (900°C). It is well established that the addition of small quantities of certain elements greatly improves oxide scale adherence and may eliminate spallation. Yttrium additions have been reported to increase adherence of the oxide scale to the metal substrate in Nb alloys. Studies performed with Cr-10W alloys indicate that Al significantly improves the oxidation resistance of these alloys; aluminized specimens show no sign of spallation during the cyclical oxidation tests [105]. Previous studies reported the benefit of minor additions of Sn on eliminating pesting behavior on Nb-Si-Cr alloys at intermediate temperatures [14].
- The complexity of the oxidation mechanisms limits the development of a generalized oxidation model and a case by case study may be necessary to

determine the right Cr-W composition for a specific environment. In order to reduce the amount of experiments necessary to attain this optimal composition, simulation software based on thermodynamic and crystallographic data can be employed to calculate parameters that are difficult to measure and determine the thermodynamical stability of the alloys. Simulations may also provide information regarding the influence of the crystallographic structures and temperature changes in the oxidation process and scale adherence. It is evident that more robust databases will be needed in order to predict the relationship between the microstructural changes, the temperature variations and the diffusion processes.

- The amount of Cr determines the volume fractions of intermetallic phase in the alloys and the oxide scale composition. The oxidation resistance of the alloy can be improved by modifying the relative compositions of the oxides in the scale; a more uniform scale may be obtained by using heat treated samples.
- Due to the significant amount of intermetallic compound in the alloy, brittleness is a concern especially in alloys with 30% Cr; therefore it is recommended that further studies should be based in Cr compositions around 23-25% Cr since this composition is expected to have a better balance of mechanical properties while maintaining good oxidation resistance.

REFERENCES

- [1] B.P. Bewlay, M.R. Jackson, J.C. Zhao, P.R. Subramanian, M.G. Mendiratta, J.J. Lewandowski, "Ultrahigh-Temperature Nb-Silicide-Based Composites", *MRS Bulletin*, September 2003, 646-653.
- [2] B.P. Bewlay, M.R. Jackson, J.C. Zhao, P.R. Subramanian, "A Review of Very High Temperature Nb-Silicide-Based Composites", *Metall. Trans. A*, 34A (2003), 2043-2052.
- [3] P.R. Subramanian, M.G. Mendiratta, D.M. Dimiduk, M.A. Stucke, "Advanced Intermetallic Alloys-Beyond Gamma Titanium Aluminides", *Mat. Sci. Eng.*, A239 (1997), 1-13.
- [4] H.J. Song, "Processing, Phase Transformation, and Microstructural Evolution of Advanced Nb-Ti-Si-Al-Cr-X Alloys for High Temperature Aeroengine Applications", (Master's Thesis, University of Cincinnati, 2005).
- [5] M. Nedyakha, V.G. Chernyi, "Increasing the Oxidation Resistance of Niobium at Elevated Temperatures", *Fiziko Khimicheskaya Mekhanika Materialov*, 2 (6) (1966), 646-648.
- [6] K.S Chan, "Cyclic-Oxidation Resistance of Niobium-Base in situ Composites: Modeling and Experimentation", *Oxidation of Metals*, 61 (2004), 165-194.
- [7] R.A. Perkins, K.T. Chang, G.H. Meier, R. Miller, "Oxidation of High Temperature Intermetallics", T. Grobstein and J. Doychak, eds., (TMS, Warrendale, 1988), 157-169.
- [8] J. Doychak and M.G Hebsur, "Protective Al₂O₃ Scale Formation on NbAl₃-Base Alloys", *Oxidation of Metals*, 36(1) (1991), 113-141.
- [9] B. Bewlay, M.Jackson, H. Lipsitt, "The Balance of Mechanical and Environmental Properties of a Multielement Niobium-Niobium Silicide-Based In Situ Composite", *Metall. Trans. A*, 27A (1996), 3801-3808
- [10] J. Geng, P. Tsakiroopoulos, G.Shao, "Oxidation of Nb-Si-Cr-Al in situ Composites with Mo, Ti and Hf Additions", ", *Mat. Sci. Eng.*, A441 (2006), 26-38.
- [11] P.R. Subramanian, M.G. Mendiratta, D.M. Dimiduk, "The Development of Nb Based Advanced Intermetallic Alloys for Structural Applications", *JOM*, 48 (1) (1996), 33-38.
- [12] K.S Chan, "Cyclic Oxidation Response of the Multiphase Niobium-Based Alloys", *Metall. Mater. Trans. A*, 35A (2004), 589.
- [13] V. Behrani, A.J. Thom, M. J. Kramer, M. Akinc, "Microstructure and Oxidation Behavior of Nb-Mo-Si-B Alloys", *Intermetallics*, 14 (2006), 24-32.

- [14] J. Geng, P. Tsakiroopoulos, "A Study of the Microstructures and Oxidation Resistance of Nb-Si-Cr-Al-Mo in situ Composites Alloyed with Ti, Hf and Sn", *Intermetallics*, 15 (2007), 382-395.
- [15] C.L. Ma, J.G. Li, Y. Tan, R. Tnaka, S. Hanada, "Effect of B Addition on the Microstructures and Mechanical Properties of Nb-16Si-10Mo-15W Alloy", *Mat. Sci. Eng. A*, 384, (2004), 377-384.
- [16] T. Murakami, S. Sasaki, K. Ichikawa, A. Kitahara, "Oxidation Resistance of Powder Compacts of the Nb-Si-Cr System and Nb₃Si₅Al₂ Matrix Compacts Prepared by Spark Plasma Sintering", *Intermetallics*, 9 (2001), 629-635.
- [17] E.S. Menon, M.G. Mendiratta, D.M. Dimiduk, "Oxidation Behavior of Complex Niobium Based Alloys", *Proceedings of the International Symposium Niobium 2001*, Orlando, Florida, USA, 121-145.
- [18] C. Liu, P. Tortorelli, J. Horton, C. Carmichael, "Effects of Alloy Additions on the Microstructure and Properties of Cr-Cr₂Nb Alloys", *Mat. Sci. Eng.*, A214 (1996), 23-32.
- [19] D.J. Thoma, K.C. Chen, F. Chu, P.G. Kotula, T.E. Mitchell, J.M. Wills, A.O. Ormeci, S.P. Chen, R.C. Alberts, "Theoretical and Experimental Investigation on the Low Temperature Properties of the NbCr₂ Laves Phase", Los Alamos National Laboratory, DOE Office of Scientific and Technical Information (OSTI), (1999), <http://www.osti.gov/bridge/servlets/purl/763895-6QaaQU/webviewable/763895.PDF>.
- [20] M.Yoshida, T. Takasugi, "Phase Relation and Microstructure of the Nb-Cr-W Alloy System", *Mat. Sci. Eng.*, A262 (1999), 107-114.
- [21] H. Okaniwa, D. Shindo, M.Yoshida, T. Takasugi, "Determination of the site Occupancy of Additives X (X=V, Mo, W and Ti) in the Nb-Cr-X Laves Phase by ALCHEMI", *Acta mater*, 47 (6) (1999), 1897-1992.
- [22] M.Yoshida, T. Takasugi, "Phase Relation and Microstructure of Nb-Cr-V and Nb-Cr-Mo Alloy Systems", *Mat. Sci. Eng.*, A224 (1997), 69-76.
- [23] P. Kakarlapudi, S. Varma, "High Temperature Oxidation of Nb-20W-10Cr Alloy in Air up to 1400°C", *PFAM XV Proceedings*, (2006), 131-139.
- [24] B. Portillo, P. Kakarlapudi, S.K. Varma, "The Possible Applications of Nb-W-Cr Alloys in High-Temperature Air", *JOM*, 59 (6) (2007), 46-49.
- [25] M.D. Gonzalez, S.K. Varma, "Oxidation Behavior of Alloys from the Nb-W-Cr System Containing C Modifiers", *Proceedings TMS 2008 Conference*, Vol I, 455-460.
- [26] M.D. Moricca, S.K. Varma, "High Temperature Oxidation Characteristics of Alloys from the Nb-W-Cr System with C Additions", *JOM*, 60 (7) (2008), 66-69.

- [27] Y.W. Kim and T. Carneiro, eds., "Niobium High Temperature Applications", *Proceedings of the International Symposium on Niobium for High Temperature Applications* (Warrendale, PA:TMS, 2003).
- [28] C.T. Sims, N.S. Stoloff, W.C. Hagel, eds., *Superalloys II*, (Wiley-Interscience Publication, 1987).
- [29] R.C. Reed, *The Superalloys Fundamental and Applications*, (New York:Cambridge University Press, 2006).
- [30] A.L. Bement, "Trends and Needs for High Temperature Materials", S.M. Allen, R.M. Pelloux, and R. Widmer, eds, *Advanced High Temperature Alloys Processing and Properties*, ASM, American Society of Metals, (1986), 141.
- [31] P. Lipetzky, "Refractory Metals: A Primer", *JOM*, 54 (3) 2002, 47-49.
- [32] J. Wittenauer, "Refractory Metals 1990: Old Challenges, New Opportunities", *JOM*, 42 (8), 1990, 7.
- [33] C.L. Briant, "The Use of Refractory Metals as High Temperature Materials", *J. of Eng, and Mat. Tech.*, 22 (2000), 338-341.
- [34] Los Alamos National Laboratory's Chemistry Division, *Periodic Table of the Elements*, <http://periodic.lanl.gov/default.htm>.
- [35] W.O. Soboyejo, T.S. Srivatsan, *Advanced Structural Materials. Properties, Design Optimization and Applications*, (CRC Press, 2007).
- [36] http://wings.avkids.com/Book/Propulsion/Images/components_01.jpg.
- [37] C.G. Wodjcik, "Thermomechanical Processing and Properties of Niobium Alloys", http://www.cbmm.com.br/portug/sources/techlib/science_techno/table_content/sub_2/images/pdfs/011.pdf
- [38] J.R. Davis, *Alloying:Understanding the Basics*, (ASM International, 2001).
- [39] M. Schwartz, *Encyclopedia of Materials, Parts, and Finishes*, 2nd ed., (CRC Press 2002).
- [40] J. R. Davis, *Heat Resistant Materials*, (ASM International, 1997).
- [41] T.E. Tietz, J.W. Wilson, *Behavior and Properties of Refractory Metals*, (Stanford University Press, 1965).
- [42] Y. Murayama, S. Hanada, "High Temperature Strength, Fracture Toughness and Oxidation Resistance of Nb-Si-Al-Ti Multiphase Alloys", *Science and Technology of Advanced Materials*, 3 (2002), 145-156.

- [43] K. Zelenitsas, P. Tsakiroopoulos, "Effect of Al, Cr and Ta Additions on the Oxidation Behaviour of Nb-Ti-Si in situ Composites at 800°C", *Mat. Sci. Eng.*, A416 (2006), 269-280.
- [44] K. Zelenitsas, P. Tsakiroopoulos, "Study of the Role of Al and Cr Additions in the Microstructure of Nb-Ti-Si in situ Composites", *Intermetallics*, 13 (2005), 1079-1095.
- [45] M.P. Moricca, S.K. Varma, "High Temperature Oxidation Characteristics of Nb-10W-XCr Alloys", *Journal of Alloys and Compounds*, 489 (2010), 195-201.
- [46] J. Ventura, "High Temperature Oxidation Behavior of Nb-20Mo-15Si-5B-20Cr Alloy", (Thesis, University of Texas at El Paso, 2009).
- [47] D. Thoma, J. Perepezko, "An Experimental Evaluation of the Phase Relationships and Solubilities in the Nb-Cr System", *Mater. Sci. Eng. A.*, 156 (1) (1992), 97-108.
- [48] J. Friauf, "The Crystal Structures of Two Intermetallic Compounds", *Intermetallic Compound Crystal Structures*, 49 (1927), 3107-3114.
- [49] J. Friauf, "The Crystal Structure of Magnesium Di-Zincide", *Physical Review*, 29 (1927), 34-40.
- [50] F. Laves, "Laves:Kristallographi der Legierungen", *Naturwissenschaften*, 27 (1939), 65-73.
- [51] F. Stein, M. Palm, G. Sauthoff, "Structure and Stability of Laves Phases. Part I. Critical Assessment of Factors Controlling Laves Phase Stability", *Intermetallics*, 12 (2004), 713-720.
- [52] T. Ohta, Y. Nakagawa, Y. Kaneno, H. Inoue, T. Takasugi, "Microstructure and Mechanical Properties of NbCr₂ and ZrCr₂ Laves Phase Alloys Prepared by Powder Metallurgy", *J. of Mat. Sci.*, 38 (2003), 657-665.
- [53] R. Johnston, R. Hoffmann, "Structure-Bonding Relationships in the Laves Phases", *Z. Anorg. All. Chem.*, 616 (1992), 105-120.
- [54] F. Chu, D. Thoma, P. Kotula, S. Gerstl, T. Mitchell, I. Anderson, J. Bentley, "Phase Stability and Defect Structure of the C15 Laves Phase Nb(Cr,V)₂", *Acta Mater.*, 46 (5) (1998), 1759-1769.
- [55] J. English, "Alloy Phase Diagrams: Cr-Nb-W Isothermal Sections", *ASM Handbook Vol 3*, H. Baker ed., (Materials Park, Ohio, 1999), 3-47.
- [56] S.D. Cramer, B.S. Covino, eds., *Corrosion: Fundamentals of Corrosion in Gases*, *ASM Handbook Vol 13*, (Materials Park, Ohio, 1987), 61.
- [57] P. Kofstad, *High Temperature Corrosion*, (Elsevier Applied Science, 1988).

- [58] N. Birks, G.H. Meier, F.S. Pettit, "Introduction to the High-Temperature Oxidation of Metals, 2nd ed., (Cambridge University Press, 2006).
- [59] http://www.doitpoms.ac.uk/tlplib/ellingham_diagrams/ellingham.php.
- [60] C. Xu, W. Gao, "Pilling-Bedworth Ratio for Oxidation of Alloys", *Mat. Res. Innovat.*, 3 (2003), 231-235.
- [61] N.B. Pilling and R.E. Bedworth, "The Oxidation of Metals at High Temperatures", *J. Inst. Met.*, 29 (1923), 529.
- [62] A.S. Khanna, Introduction to High Temperature Oxidation and Corrosion, (Materials Park, Ohio, ASM International, 2002).
- [63] F. Gesmundo, B. Gleeson, "Oxidation of Multicomponent Two-Phase Alloys", *Oxidation of Metals*, 44 (1/2) (1995), 211-237.
- [64] R.A. Rapp, "The High Temperature Oxidation of Metals Forming Cation-Diffusing Scales", *Metall. Trans. B*, 15B, (1984), 195-212.
- [65] C. Wagner, "Theoretical Analysis of the Diffusion Processes Determining the Oxidation Rate of Alloys", *Journal of the Electrochemical Society*, 99 (10) (1952), 369-380.
- [66] G. Wahl, "Coating Composition and the Formation of Protective Oxide Layers at High Temperatures", *Thin Solid Films*, 107 (1983), 417-426.
- [67] G. Wang, "Theoretical Aspects of Oxidation of Composite Materials", *Journal de Physique IV*, 3 (1993), 873-880.
- [68] G. Wang, B. Gleeson, D. Douglass, "A Diffusional Analysis of the Oxidation of Binary Multiphase Alloys", *Oxidation of Metals*, 35 (5/6) (1991), 333-348.
- [69] G. Wang, B. Gleeson, and D. Douglass, "An Extension of Wagner's Analysis of Competing Scale Formation", *Oxidation of Metals*, 35 (3/4) (1991), 317-332.
- [70] F. Gesmundo, Y. Niu, F. Viani, "Possible Scaling Models in High-Temperature Oxidation of Two-Phase Binary Alloys II: Low Oxidant Pressures", *Oxidation of Metals*, 43 (3/4) (1995), 379-394.
- [71] F. Gesmundo, F. Viani, Y. Niu, D. Douglass, "Further Aspects of the Oxidation of Binary Two-Phase Alloys", *Oxidation of Metals*, 39 (3/4) (1993), 197-209.
- [72] F. Gesmundo, F. Viani, Y. Niu, D. Douglass, "The Transition from the Formation of Mixed Scales to the Selective Oxidation of the Most-Reactive Component in the Corrosion of Single and Two-Phase Binary Alloys", *Oxidation of Metals*, 40 (3/4) (1993), 373-393.
- [73] N. Birks, G.H. Meier, F.S. Pettit, "High-Temperature Oxidation of Metals", 2nd ed, Cambridge University Press, 2006, 98.

- [74] T. Hurlen, "Oxidation of Niobium", *Journal of the Institute of Metals*, 89 (1960-61), 273-280.
- [75] O. Kubaschewski and B.E. Hopkins, "Oxidation Mechanisms of Niobium, Tantalum, Molybdenum and Tungsten", *Journal of Less-Common Metals*, 2 (1960), 172-180.
- [76] G. Brauer, "Die Oxyde des Niobs", *Z. Anorg. Allg. Chem.*, 248 (1) (1941).
- [77] A.U. Seybolt, "Solid Solubility of Oxygen in Columbium", *Trans. AIME*, 200 (1954), 770.
- [78] R.T. Bryant, "The Solubility of Oxygen in Transition Metal Alloys", *Journal of Less-Common Metals*, 4 (1) (1962), 62-68.
- [79] R. P. Elliot, "Niobium-Oxygen System", *Trans. Am. Soc. Metals*, 52 (1960), 990.
- [80] T.P. Hennessey, J.E. Morral, "Oxidation and Nitridation of Niobium in Air Above 1150°C", *Oxidation of Metals*, 38 (1) (1992), 163-187.
- [81] C. K. Gupta, A. K. Suri, "Extractive Metallurgy of Niobium", CRC Press, 1994, 142.
- [82] P. Franke, "Binary Systems Part 4: Binary Systems from Mn-Mo to Y-Zr", Vol. 19B4. *Landolt-Börnstein-Group IV Physical Chemistry, Chapter Fe-O*, Springer Berlin Heidelberg, (2006), 1-2.
- [83] H. Goldschmidt, "A High-Temperature X-Ray Investigation of Niobium Pentoxide and Some Problems Concerning the Oxidation of Niobium", *J. Inst. Metals*, 87 (1959), 235-239.
- [84] H. Schäfer, R. Gruehn, F. Schulte, "The Modifications of Niobium Pentoxide", *Angew. Chem. Int. Edit. Eng.*, 5 (1) (1966), 40-52.
- [85] C.A. Barrett, J.L. Corey, "Oxidation Behavior of binary Niobium Alloys", *NASA Technical Note D-283*, Washington November 1960.
- [86] J.F. Stringer, "High Temperature Corrosion of Aerospace Alloys", (AGARD-AG200, Advisory Group of Aerospace Research and Development, NATO, August 1975).
- [87] M.G. Hebsur, J.R. Stephens, J.L. Smialek, C.A. Barrett, D.S. Fox, "Oxidation of High Temperature Intermetallics", T. Grobstein and J. Doychak, eds. (TMS, Warrendale, 1989), 171-184.
- [88] H. J. Grabke, M. Steinhorst, M. Brumm, D. Wiemer, "Oxidation and Intergranular Disintegration of the Aluminides NiAl and NbAl₃ and Phases in the System Nb-Ni-Al", *Oxidation of Metals*, 35 (3/4) (1991), 199-222.
- [89] A. Misra, "Niobium System Design of Niobium Superalloys", (Ph.D. thesis, Northwest University, Evanston Illinois, 2005).

- [90] Y. Niu, F. Gesmundo, F. Viani, "The Corrosion of Pure Niobium Oxidizing, Sulfidizing, and Oxidizing-Sulfidizing Gas Mixtures", *Oxidation of Metals*, 46 (3/4) (1996), 287-297.
- [91] M.G. Hebsur, J.R. Stephens, "Niobium-Aluminum Base Alloys Having Improved, High Temperature Oxidation Resistance", U.S. Patent 4, 983, 358, (Jan 8, 1991).
- [92] J. Geng, P. Tsakiroopoulos, G. Shao, "A Thermo-gravimetric and Microstructural Study of the Oxidation of Nb_{ss}/Nb₅Si₃-based Composites with Sn Addition", *Intermetallics*, 15 (2007), 270-281.
- [93] D.M. Dimiduk, M.G. Mendiratta, P.R. Subramanian, "Development Approaches for Advanced Intermetallic Materials-Historical Perspective and Selected Successes", *Structural Intermetallics*, 1993, 619-629.
- [94] E.S.K. Menon, M.G. Mendiratta and D.M. Dimiduk, "High Temperature Oxidation Mechanisms in Nb-silicide Bearing Multicomponent Alloys", K.J. Hemker, D.M. Dimiduk, H. Clemens, R. Darolia, H. Inui, J.M. Larsen, V.K. Sikka, M. Thomas, and J.D. Whittenberger, eds, *Structural Intermetallics*, TMS, The Minerals, Metals and Materials Society (2001), 591.
- [95] T. Murakami, C. Xu, A. Kithara, M. Kawahara, Y. Takahashi, H. Inui, M. Yamaguchi, "Microstructure, Mechanical Properties and Oxidation Behavior of Powder Compacts of the Nb-Si-B System Prepared by Spark Plasma Sintering", *Intermetallics*, 7 (1999), 1043-1048.
- [96] Y. Liu, A.J. Thom, M.J. Kramer, and M. Akinc, "Processing and Oxidation Behavior of Nb-Si-B Intermetallics", *Proceedings of the XIth International Symposium on Processing and Fabrication of Advanced Materials*, (2003), 258-271.
- [97] B.P. Bewlay, J.J. Lewandowski, M.R. Jackson, "Refractory Metal-Intermetallic In-Situ Composites for Aircraft Engines", *JOM*, (1997), 44-45.
- [98] Pandat™ 7.0, Multi-component Phase Equilibrium Calculation Software, CompuTherm LLC, Madison, WI, (2007).
- [99] J. Lambert, M. Schussler, "Refractory Metals and Alloys", *ASM Handbook Vol 9, Metallography and Microstructures*, (Materials Park, Ohio, 1998), 440.
- [100] B.D. Cullity, *Elements of X-Ray Diffraction*, 2nd. ed., (Addison-Wesley Publishing Company Inc., 1978).
- [101] W.F. Gaze, Totemeier T.C. editors, "Smithells metals reference book", 8th ed, Elsevier Butterworth-Heinemann, (2004).
- [102] J.S. Sheasby, "The Oxidation of Niobium in the Temperature Range 450°-720°C", *J. Electrochem. Soc.*, 115 (7) (1968), 695-700.

- [103] D.J. Derry, D.G. Lees, "The Oxidation Behaviour of a Niobium-Chromium-Nickel Alloy", *Corrosion Science*, 16 (1976), 219-232.
- [104] J. Smialek, "A Deterministic Interfacial Oxidation Spalling Model", *Acta Materialia*, 51 (2003), 469-483.
- [105] Ö.N. Doğan, "Effect of Al on High Temperature Oxidation of Cr-W Alloys", *Oxidation of Metals*, 69 (2008), 233-247.

CURRICULUM VITA

Pilar Moricca was born in Chihuahua, Chihuahua. She obtained a Bachelor degree in Chemical Engineering from the Instituto Tecnológico de Chihuahua in 1996 and received her Master of Science degree in Materials Science from the Advanced Materials Research Center (CIMAV) in Chihuahua, Chih. during the spring of 1999. Her research project covered the development and characterization of nanoparticles and magnetic fluids. In 1999 she was the recipient of the Academic Excellence Award. After obtaining her Master's degree in Materials Science, she worked as a Materials Engineer for Delphi Corporation in Cd. Juárez, Chih.

During the fall of 2004 Pilar joined the doctoral program at the University of Texas at El Paso. In 2006 she started working as a research assistant for the Metallurgical and Materials Engineering Department under the guidance of Dr. S.K. Varma. Her research focused in the study and the development of Nb-based materials for high temperature applications and it was sponsored by the National Energy Technology Laboratory of the U.S. Department of Energy.

Pilar has presented her work at international conferences and she has several publications in international journals such as the Journal of Alloys and Compounds and the Journal of Metals.

Permanent address: 505 Rosinante Rd
 El Paso, TX, 79922

This dissertation was typed by the author.